Coordination of protrusive forces in immune cell migration

by

Patricia Reis-Rodrigues

July, 2025

A thesis submitted to the
Graduate School
of the
Institute of Science and Technology Austria
in partial fulfillment of the requirements
for the degree of
Doctor of Philosophy

Committee in charge:
Prof. Dr. Florian Schur, Chair
Prof. Dr. Anna Akhmanova
Prof. Dr. Mario De Bono
Prof. Dr. Michael Sixt

The thesis of Patricia Reis-Rodrigues, titled *Coordination of protrusive forces in immune cell migration*, is approved by:

Supervisor: Michael Sixt, ISTA, Klosterneuburg, Austria

Signature: _____

Committee Member: Mario De Bono, ISTA, Klosterneuburg, Austria

Signature: _____

Committee Member: Anna Akhmanova, Faculty of Science, Utrecht University, Utrecht, Netherlands

Signature: _____

Defense Chair: Florian Schur, ISTA, Klosterneuburg, Austria

Signature: _____

Signed page is on file

I hereby declare that this thesis is my own work and that it does not contain other people's work without this being so stated; this thesis does not contain my previous work without this being stated, and the bibliography contains all the literature that I used in writing the dissertation.

I accept full responsibility for the content and factual accuracy of this work, including the data and their analysis and presentation, and the text and citation of other work.

I declare that this is a true copy of my thesis, including any final revisions, as approved by my thesis committee, and that this thesis has not been submitted for a higher degree to any other university or institution.

I certify that any republication of materials presented in this thesis has been approved by the relevant publishers and co-authors.

Signature: _____

Patricia Reis-Rodrigues

July, 2025

Signed page is on file

Abstract

Immune responses depend on the coordinated and efficient migration of leukocytes. These cells, which are embedded and tightly confined within tissues, must navigate and traverse diverse and complex three-dimensional environments. Leukocytes adapt their locomotory behavior to the mechanical, geometrical, and biochemical characteristics of their surroundings. In low-density environments, where the pore size of the interstitial matrix allows free passage, these cells position the nucleus directly behind the lamellipodium, the protrusive actin structure that forms the leading front of the cell. In this configuration, they use the nucleus as a gauge to identify the path of least resistance.

Here, we show that in high-density environments, where the pore size precludes free passage of the cell body, leukocytes reposition the microtubule-organizing center (MTOC) and associated organelles in front of the nucleus. In this configuration, they use actin structures protruding orthogonally to the direction of migration in order to open a path for the cell body. We identify two distinct actin populations that serve this purpose at different subcellular localizations. At the leading edge, local indentation of the plasma membrane leads to recruitment of the Wiskott-Aldrich syndrome protein (WASp), which, via Arp2/3, results in the formation of individual actin foci. At the cell body, actin polymerization is triggered by DOCK8, a Cdc42 exchange factor, resulting in the formation of a central actin pool.

We demonstrate that the central and peripheral actin pools are functionally communicating and that depletion of the central actin pool leads to increased actin accumulation at the cell front, resulting in excessive extension of the leading edge.

Acknowledgments

First of all, I would like to thank Michael Sixt for giving me the opportunity to work in his lab. I have learned so much from him over the years, and I am truly grateful for his guidance in helping me become the scientist I am proud to be today.
On that note, I also want to thank all past and present members of the Sixt Lab. It has been—and continues to be—a pleasure to work and exchange ideas with such brilliant and supportive colleagues. You all make work feel like home.
I would like to thank my thesis committee, Anna Akhmanova and Mario De Bono, for their valuable feedback and support throughout the years. I am also grateful to the Imaging and Optics, Pre-clinical, Lab Support, and Nanofabrication facilities at ISTA for their constant assistance. A special thank you goes to all the co-authors of my paper; I could not have achieved this without your collaboration and support. Also, I would like to acknowledge the financial support of the European Research Council through the ERC-SyG grant "Pushing from within: Control of cell shape, integrity and motility by cytoskeletal pushing forces" (01071793), which made this research possible.

Finally, to all my friends—whether you're just around the corner or a bit further away—thank you for being my personal cheerleaders, reality checks, and constant source of laughter. Your messages, calls, late-night rants and unofficial therapy sessions have kept me sane (or at least close enough). I'm so lucky to have you in my life.

I began my PhD journey in 2018. It was a challenging year—a year of many changes, deeply sad endings, and new beginnings. This PhD was something I truly wanted to pursue, and I am absolutely certain I wouldn't be writing these words of thanks if it weren't for the unconditional support of my family, who never let me give up on my dreams. This work is dedicated to them: to my sister, Bea, to my mom, Elisabete, and to the loving memory of my dad, Armando. Obrigada, sem o vosso apoio e amor, nada disto seria possível.

"Esse é o único destino dos homens, começar e acabar, acabar e começar."
"This is the only destiny of men, to begin and to end, to end and to begin."
- O Evangelho Segundo Jesus Cristo, José Saramago.

About the Author

Patricia Reis-Rodrigues completed a BSc in Biochemistry and an MSc in Medical Biochemistry at the Faculty of Sciences, University of Lisbon, in 2017. During her Master's studies, she investigated centrosome stability during oogenesis, which sparked her interest in the role and dynamics of cytoskeletal proteins. She joined ISTA in 2018 and became a member of Michael Sixt's laboratory in 2019 to study actin dynamics in migrating immune cells. Patricia has presented her research at several international conferences, including the European Cytoskeleton Forum Meeting (2022), the Directed Cell Migration Gordon Research Conference (2023), the EMBO Forces Across Scales Conference (2024), and the EMBO Cell Polarity and Membrane Dynamics Meeting (2025). The main body of her thesis work was recently published in *Nature Immunology*.

List of Collaborators and Publications

Florian Gaertner, **Patricia Reis-Rodrigues**, Ingrid de Vries, Miroslav Hons, Juan Aguilera, Michael Riedl, Alexander Leithner, et al. "WASp Triggers Mechanosensitive Actin Patches to Facilitate Immune Cell Migration in Dense Tissues." ***Developmental Cell*** 57, no. 1 (January 10, 2022): 47-62.e9. https://doi.org/10.1016/j.devcel.2021.11.024.

In this project, I provided conceptual and experimental assistance to the first author, Florian Gaertner. Specifically, I generated the dendritic cells expressing LifeaAct-eGFP and CIP4-mcherry, presented in Figure 3H. I performed and analyzed experiments of WT and WASp-depleted cells migrating in collagen gels of varying densities, shown in Figure 5 A-E. Experiments of cells migrating in labeled collagen gels were performed and analyzed in collaboration with Michael Riedl and are presented in Supplementary Figure 5 B, C. Additionally, I performed and analyzed experiments to show the absence of myosin II in the WASp-mediated actin foci, shown in Supplementary Figure 1D.

This publication was re-used in full in chapter 3 of this thesis.

Patricia Reis-Rodrigues, Mario J. Avellaneda, Nikola Canigova, Florian Gaertner, Kari Vaahtomeri, Michael Riedl, Ingrid de Vries, Jack Merrin, Robert Hauschild, Alba Juanes Garcia, Yoshinori Fukui, and Michael Sixt. "Migrating Immune Cells Globally Coordinate Protrusive Forces." (Accepted in ***Nature Immunology***)

In this project, I conceived, performed and analyzed most of the experiments. Experimental set-up and analysis of bead displacement in agarose was done in collaboration with Mario J. Avellaneda, as presented in Figure 2a-e. Nicola Canigova assisted with performance and analysis of the MTOC-nucleus position in microfabricated channels and under agarose, shown in Figure 1f,g and Extended Data Figure 1g,h. Florian Gaertner provided data on cells migrating under different agarose stiffness in Figure 1k. Michael Rield and Robert Hauschild wrote image-analysis scripts for the quantification of collagen I fiber deformation and actin bursts proximity (Extended Data Figure 2f,g) and the analysis of the central actin pool in cells moving in pillar mazes, and cross-correlation analysis of central actin pool, protrusions and cell area/cell speed (Figure 4h-j and Extended Data Figure 4f-i), respectively. Experiments with enucleated dendritic cells, presented in Figure 2f, were performed with the assistance of Ingrid de Vries. Jack Merrin generated microfabricated channels and pillar arrays. Yoshinori Fukui provided reagents, technical support and advice. Kari Vaahtomeri, Alba Juanes Garcia, and Michael Sixt provided conceptual and experimental feedback. I wrote the manuscript in collaboration with Mario J. Avellaneda and Michael Sixt, which was critically reviewed by all the co-authors.

This publication was re-used in full in chapter 4 of this thesis.

Table of Contents

List of Figures

List of Abbreviations

2D	two-dimensional
3D	three-dimensional
AC	adenylyl cyclases
ADP	adenosindiphosphate
ATP	adenosintriphosphate
cAMP	cyclic adenosine monophosphate
CLP	common lymphoid progenitor
CMP	common myeloid progenitor
DCs	dendritic cells
DH	Dbl-homology
DHR	Dock-homology region
ECM	extracellular matrix
F-actin	Filamentous actin
fMLP	formyl-methionyl-leucine-phenylalanine
G-actin	Globular actin
GAP	GTPase-activating protein
GDI	Guanine nucleotide dissociation inhibitor
GDP	guanosindiphosphat
GEF	Guanine exchange factor
GPCRs	G-protein coupled receptors
GTP	guanosintriphosphat
GTPase	Guanosine Triphosphatase
Gα	G alpha
Gβ	G beta
Gγ	G gamma
HVR	hypervariable region

LPA	lysophosphatidic acid
mDia1	mammalian Diaphanous-related formin 1
Mg^{2+}	magnesium
MHC	major histocompatibility complex
MLC	myosin light-chain
MMPs	matrix metalloproteinases
MTOC	microtubule-organizing center
NPF	nucleation promoting factor
PAMPs	pathogen-associated molecular patterns
PH	pleckstrin homology
Pi	Inorganic phosphate
PI3K	phosphatidylinositol 3-kinase
PIP2	phosphatidylinositol 4,5-bisphosphate
PIP3	phosphatidylinositol 3,4,5-trisphosphate
PKA	cAMP-dependent protein kinase A
PRRs	pattern recognition receptors
ROCK	Rho-associated coiled-coil containing protein kinase
S1P	sphingosine 1-phosphate
WAVE	WASP-family verprolin homologous

1 Introduction

1.1 A short overview of the immune system

The ability to protect oneself is a key element for any organism's survival. The first line of defense relies on the capacity to recognize and eliminate pathogens, a task taken by the immune system. The earliest forms of immune defense appeared in single-celled organisms, which used basic mechanisms like restriction enzymes and clustered regularly interspaced palindromic repeats (CRISPRs) to detect and neutralize foreign invaders[1]. As multicellularity evolved, so did the need for more complex defense systems.

The immune system of vertebrates combines physical and chemical barriers, like the skin or mucous membranes, that act as the individual's first line of defense, with a complex and highly coordinated network of molecules and cells[2]. All cells of the immune system arise from pluripotent hematopoietic stem cells in the bone marrow, which generate either common lymphoid progenitor (CLP) or common myeloid progenitor (CMP) cells (Figure 1). CMPs are the precursors of macrophages, granulocytes (the collective term used for white blood cells like neutrophils, eosinophils, and basophils), mast cells and dendritic cells (DCs), which are typically involved in innate immune responses[3]. These immune cells express invariant innate pattern recognition receptors (PRRs), which recognize conserved molecules and regular patterns of molecular structure known as pathogen-associated molecular patterns (PAMPs), which are part of many microorganisms, but are not found in the host body's cells[4]. When these receptors are activated, cells respond by either engulfing and killing the invading microorganism, clearing the threat. These cells are activated by a broad range of external stimuli, resulting in fast but nonspecific responses.
Cells derived from CLPs, like B and T lymphocytes, on the other hand, recognize specific antigens. This results in slower, but more targeted responses, called adaptive immune responses. B and T lymphocytes are named after the organs in which they mature: the bone marrow and the thymus, respectively. While the primary role of B lymphocytes is to produce antibodies that target the pathogen, T lymphocytes exhibit a broad range of functions. Upon encounter with an antigen, these cells proliferate and can differentiate into cytotoxic or helper T lymphocytes. While cytotoxic T lymphocytes are specialized in eliminating infected cells, helper T lymphocytes provide signals, often in the form of cytokines that stimulate cells, like macrophages, to kill and engulf pathogens. T lymphocytes can also differentiate into regulatory T lymphocytes which suppress the activity of other cells to avoid damage caused by immune responses. Upon infection clearance, activated B and T lymphocytes can differentiate into memory cells that enable a more rapid and effective response upon subsequent exposures to the same pathogen[5]. It is this immunological memory that forms the basis for the effectiveness of vaccines.

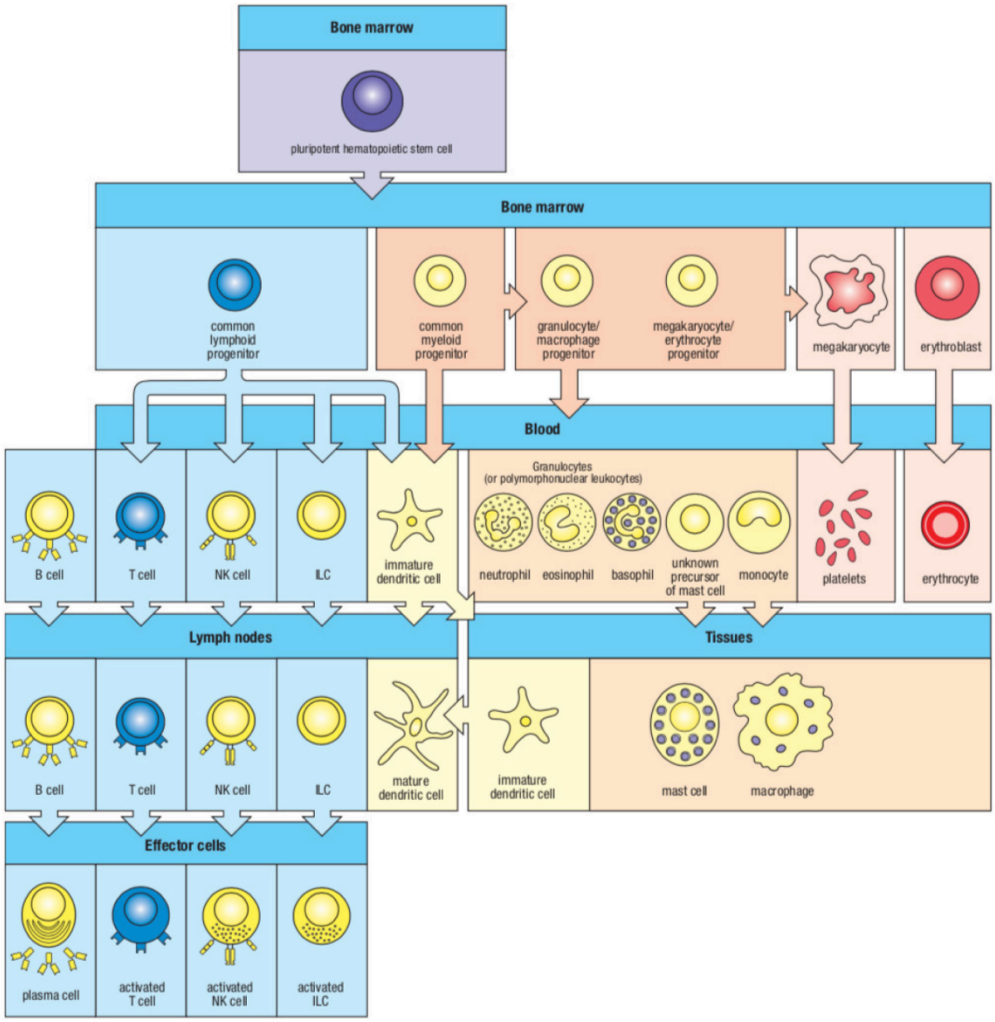

Figure 1. Different types of blood cells and their lineage. *Image adapted from Janeway's Immunobiology.*

1.2 Dendritic cells at the interface between innate and adaptive immune responses

Activation of T lymphocytes, and therefore initiation of an adaptive immune response, is triggered by cells of the innate system, most importantly dendritic cells (DCs). These cells were first described in the 1970s by Ralph Steinman and his research awarded him the Nobel Prize in Physiology or Medicine in 2011 "*for his discovery of the dendritic cell and its role in adaptive immunity*".

In their precursor state, DCs migrate from the bone marrow to the bloodstream to get to the peripheral tissues, where they patrol their surroundings as immature DCs[6]. Upon pathogen encounter, tissue resident immature DCs sense PAMPs via PRRs, which triggers phagocytosis of the pathogen. Alternatively, they can internalize soluble antigens via macropinocytosis[7,8]. In both cases, DCs engulf the foreign material and degrade it intracellularly into peptides that are then loaded on major histocompatibility complex (MHC) class I or II molecules. Pathogen sensing triggers a cellular differentiation process called maturation. Matured DCs lose their phagocytic ability and show significantly altered chemokine receptor expression pattern.

Particularly, expression of the CCR7 receptor makes DCs sensitive to the chemokine CCL21, which is produced by lymphoid tissues. CCL21 guides DCs to the nearest lymphatic vessels, from where they passively travel through lymph flow to the draining lymph node, where interaction with naïve T cells occurs[9]. Antigen-presenting DCs trigger the activation and proliferation of naïve T lymphocytes in an antigen-specific manner[10,11].

DCs play a crucial role as sensor cells that detect infection and initiate adaptive immune responses. This function is highly dependent on their capacity to efficiently and reliably migrate across different tissues with quite distinct characteristics. If their migratory capacity is impaired, it can result in delayed or weakened immune responses, which leave organisms vulnerable to infections, chronic inflammation, or autoimmune diseases. Therefore, understanding the fundamental processes ruling DC migration is essential for gaining a deeper insight into the functioning of the immune system.

1.3 The starting point of cell migration: establishing cell polarity

Migrating cells have a clear distinction between their front and back along the migration axis. This polarization can be triggered by several different cues: chemotactic gradients, growth factors, and even composition, geometry, and mechanics of their surrounding environment. All these inputs are integrated by cells through the activation of various cell surface receptors, including cytokine and adhesion receptors, receptor tyrosine kinases, as well as G-protein coupled receptors (GPCRs)[12,13].

GPCRs play a key role in leukocyte migration. These transmembrane proteins span the cell membrane seven times and work together with heterotrimeric G proteins, composed of three different subunits: G alpha (Gα), G beta (Gβ), and G gamma (Gγ). The Gβ and Gγ subunits always form a dimer and are, therefore, commonly referred to as Gβγ. There are four different families of Gα subunits: $G\alpha_s$, $G\alpha_q$, $G\alpha_i$, and $G\alpha_{12/13}$. Each of these has intrinsic guanosine triphosphatase (GTPase) activity. Binding of a ligand activates the GPCR, resulting in GDP to GTP exchange in the Gα subunit and consequent dissociation from the Gβγ dimer, triggering different downstream pathways. GTP to GDP hydrolysis in the Gα subunit leads to its reassociation with the Gβγ dimer, returning the GPCR to an inactive state[14]. The Gβγ subunit can also modulate various downstream effectors independently of Gα[15]. For example, it has been shown that the "free" Gβγ subunit resulting from GPCR activation can interact with phosphatidylinositol 3-kinase (PI3K), not only positioning this protein at the plasma membrane near its substrate, phosphatidylinositol 4,5-bisphosphate (PIP2), but also inducing conformational changes that enhance its kinase activity[16]. Activated PI3K phosphorylates PIP2 and generates phosphatidylinositol 3,4,5-trisphosphate (PIP3). PIP3 serves as a docking site for proteins containing a pleckstrin homology (PH) domain, which are crucial to modulate the pathways that regulate actin polymerization and the actomyosin cytoskeleton, shaping migration, via the Rho family of small GTPases[17,18].

1.4 Rho GTPases

Rho GTPases are membrane-bound molecular switches characterized by having two conserved and functionally distinct regions: the G-domain and a hypervariable region (HVR). The HVR, located at the C-terminus, despite exhibiting significant sequence diversity, follows

a consensus sequence known as CAAX (C is cysteine, A is any aliphatic amino acid, and X is any amino acid). This motif undergoes lipid modifications such as isoprenylation (geranylgeranyl or farnesyl), endoproteolysis, and carboxyl methylation, which are essential for membrane targeting, ensuring that Rho GTPases are localized to the correct subcellular compartments where activation and signaling occurs[19]. On the other hand, the G domain is located at the N-terminus and consists of a mix of six-stranded β-sheets surrounded by five α-helices[20,21]. This domain is responsible for the binding and hydrolysis of GTP, cycling the protein between an active GTP-bound and an inactive GDP-bound state. Together with their nucleotide binding site, all Rho GTPases also have a magnesium (Mg^{2+}) binding pocket which enhances the affinity binding of the guanine nucleotides[22].

GDP is usually tightly bound to Rho GTPases, and GTP hydrolysis is very slow; therefore, small Rho GTPases rely on auxiliary proteins to regulate the switch between their active and inactive form.

Activation of Rho GTPases is triggered by guanine exchange factors (GEFs) that catalyze the exchange from GDP to GTP[20]. On the other hand, they are inactivated by GTPase-activating proteins (GAPs) that trigger GTPase activity, and consequently GTP hydrolysis[23], or guanine nucleotide dissociation inhibitors (GDIs), which inhibit GDP dissociation, sequestering these proteins in the inactive state in the cytosol. In mammals, 22 Rho family GTPases, approximately 80 Rho GEFs, 70 Rho GAPs, and 2 Rho GDIs have been identified. Some Rho GEFs are specific for a single Rho GTPase, whereas others can activate multiple Rho GTPases[24].

1.4.1 Switching ON with Rho GEFs

Rho GTPase activation is dependent on the activity of Rho GEFs. These proteins that catalyze the exchange from GDP to GTP can be of two distinct, unrelated families depending on their homology domains: GEFs containing Dbl-homology (DH) domains represent the Dbl family, while those with Dock-homology region (DHR) domains constitute the Dock family. From the described Rho GEFs, Dbl GEFs represent 70 members, in contrast with the less prominent Dock family, with only 11 members identified.

Dbl family GEFs have their DH domain at the N-terminus, where catalysis of GTP to GDP happens. Typically associated with the DH domain, these proteins also contain a PH domain that enables them to bind to phosphoinositides or other phospholipids, thereby contributing to their membrane localization in the vicinity of membrane-associated Rho GTPases[25]. This domain can also have regulatory and autoinhibitory functions, either by directly facilitating GDP-to-GTP exchange or indirectly through interactions with other proteins[22]. Nonetheless, these functions are not consistently observed among all members of the Dbl-GEF family. The PH domain of Tiam1, intersectin, or collybistin does not seem to directly influence GTP binding or promote GTP/GDP hydrolysis. Instead, it has been suggested that the PH domain of these GEFs optimizes the orientation of the DH domain relative to the membrane, thereby enhancing its ability to catalyze nucleotide exchange[26].

In contrast, DOCK family GEFs show two different DHR domains: the DHR1 domain, which keeps these proteins bound to the plasma membrane through direct binding to phosphoinositide[27]; and the DHR2 domain, where nucleotide exchange happens[27]. Because Dock family GEF proteins are less abundant and lack a Dbl domain, they are often referred to as “atypical GEFs”; however, these GEFs seem to be way more specific, targeting individual members of the small Rho GTPase family[28,29].

Interestingly, besides the typical domains observed in either Dbl and Dock-GEF proteins, these also contain a variety of other domains which enable them to form specific complexes that activate particular pathways, as will be discussed in more detail below[25].

1.4.2 Switching OFF with Rho GAPs and GDIs

Rho GAPs and GDIs work in coordination with Rho GEFs and mediate the switch OFF of Rho GTPases. Rho GAPs recognize active Rho GTPases (GTP-bound) and accelerate the hydrolysis of GTP to GDP by several orders of magnitude[30,31]. This process is dependent on the interaction of the GAP's arginine finger (present in their Rho GAP domain) with the Rho GTPase G domain. The arginine finger neutralizes the negative charge on the γ-phosphate of GTP, helping cleave it into GDP and inorganic phosphate (Pi)[32–34]. Once GTP is hydrolyzed to GDP, the Rho GTPase undergoes conformational changes and consequently loses its affinity to effector proteins. In parallel, the inactive GDP-bound Rho GTPase is then released from the plasma membrane in a process often assisted by GDIs. While the N-terminus of a GDI binds to the G domain of the Rho GTPase, inhibiting dissociation of GDP, its highly negatively charged C-terminus attracts the HVR, resulting in membrane release. The inactivated Rho GTPases are then sequestered in the cytosol, where they are protected against degradation and non-specific activation by Rho GEFs[35]. Some GDIs also seem to interact with GTP-bound Rho GTPases, possibly maintaining a pool of Rho GTPase GTP-bound sequestered in the cytosol[36,37]. This process is reversed upon receptor activation (such as GPCRs) and consequent recruitment of the Rho GTPase-GDI complex to the plasma membrane, which is followed by rapid dissociation of the GDI and activation of the Rho GTPase via GEF activity[12].

1.5 Cycling through ON and OFF states: triggering cytoskeleton rearrangements

There are 20 canonical members of the Rho GTPase family: Rho (RhoA, RhoB, and RhoC); Rac (Rac1, Rac1c, Rac1b, Rac2, Rac3, and RhoG); Cdc42 (Cdc42, G25K, TC10, TCL, WRCH1, and WRCH2); RhoD (RhoD, RIF); RND (RND1, RND2, and RND3); and RhoH[38]. These proteins cycle between an active (switch ON) and inactive (switch OFF) state, regulated by different interacting proteins. This dynamic switching modulates a wide range of intracellular signaling pathways, such as actin cytoskeleton reorganization and cell migration[39]. In this thesis, we will focus on three of the best-characterized ones: Cdc42, Rac1, and RhoA.

1.5.1 RhoA, Rac1 and Cdc42 activation

Several ligands of GPCRs have been implicated in RhoA, Rac1, and Cdc42 activation, such as lysophosphatidic acid (LPA), sphingosine 1-phosphate (S1P), bombesin, thrombin, and endothelin. GPCR activation is neither absolutely specific nor completely promiscuous; however, it is possible to recognize specific patterns associated with the activation of specific Gα subunits. For example, activation of the G$\alpha_{12/13}$ subunits has been shown to trigger RhoA-dependent processes. G$\alpha_{12/13}$ can interact with Rho GEFs that contain PDZ domains, like PDZ-RhoGEF, which promote RhoA activation at the plasma membrane[12]. Downstream of RhoA,

Rho-associated coiled-coil containing protein kinases 1 and 2 (ROCK1 and ROCK2) are among the most extensively studied effectors. These serine/threonine kinases are activated upon binding to GTP-bound RhoA and can modulate the actin cytoskeleton via phosphorylation of two different proteins: LIM kinase and myosin light-chain (MLC)[40]. While activation of LIM kinase results in actin filament stabilization[41], MLC phosphorylation stimulates actin cross-linking by myosin[42,43]. MLC activity is further controlled through a negative feedback loop regulated by RhoA, which phosphorylates MLC phosphatase and inhibits MLC[44]. RhoA also activates the mammalian Diaphanous-related formin 1 (mDia1), promoting the organization of actomyosin bundles into stress fibers and the formation of focal adhesions[45].

On the other hand, activation of $G\alpha_i$ subunits has been shown to regulate various types of adenylyl cyclases (AC)[46]. Often found at the plasma membrane, AC converts ATP into cAMP, influencing the activity of cAMP-dependent protein kinase A (PKA), which has been shown to interact with both Rac1[47] and Cdc42[48]. Although neither Rac1 nor Cdc42 is phosphorylated by PKA, perturbation of PKA activity can promote or inhibit cell migration, depending on the cell type[49]. Besides PKA activation via the $G\alpha_i$ subunit, several studies have shown that the Gβγ subunit recruits specific GEFs to the membrane to enhance Rac1 and Cdc42 activities[50,51]. Targeting of these GEFs to the plasma membrane depends on PI3K activity, as their PH domains can directly bind its product, PIP3[52–54].

Interestingly, in neutrophils, the chemoattractant formyl-methionyl-leucine-phenylalanine (fMLP) binds to a GPCR that activates both $G\alpha_i$ and $G\alpha_{12/13}$ subunits, generating opposing signals. $G\alpha_i$ activation of PI3K and Rac1 establishes the cell front, while $G\alpha_{12/13}$ induction of RhoA-dependent actomyosin contractility defines the cell rear[55].

$G\alpha_i$ and $G\alpha_{12/13}$ family of GPCRs have a key role in polarity establishment and chemotactic responses. Efficient locomotion depends on the coordinated activation of Cdc42, Rac1, and RhoA in particular localizations in the cell. While the restricted activation of Cdc42 and Rac1 at the front of the cell establishes cell polarity and promotes leading edge formation, RhoA activity is more pronounced at the rear, where it regulates the turnover of focal adhesions and contraction[56]. Among the various mechanisms that regulate Rho GTPase activity, GEF-containing complexes represent one important means of ensuring spatial and temporal control. They help coordinate the distinct subcellular functions of Rac1, Cdc42, and RhoA, contributing to the establishment of front-back polarity and remodeling of the actin cytoskeleton[57,58,25]. Therefore, to understand locomotion, it is essential to first understand the organization and dynamics of actin filaments.

1.6 Principles of actin dynamics

Actin exists in two forms: the monomeric form, G-actin (globular), and its polymerized form, F-actin (filamentous). F-actin is formed by G-actin subunits arranged in a double helical manner, in a process that involves two different steps: nucleation and elongation.

Actin nucleation refers to the process of forming a stable actin trimer (three monomers) and is considered a rate-limiting step in the formation of new actin filaments. Although two actin monomers can associate transiently, they require the addition of a third unit to create a stable "nucleus" that supports elongation. Formation of this trimer is rare and energetically unfavorable; thus requires the presence of NPFs that accelerate and bypass the spontaneous trimer formation barrier[59,60]. Once the trimer is formed, actin filaments can be elongated. Elongation relies on the intrinsic polarity of actin filaments, which show a rapidly growing end

called the barbed (+) end, and a slowly growing end called the pointed (-) end (Figure 2A). ATP-bound G-actin is preferentially added to the barbed end, and as monomers are incorporated into the filament, ATP to ADP hydrolysis happens, promoting the addition of the next actin monomer to the pre-existing filament. The actin filament becomes a mixed nucleotide polymer, with ATP-actin at the barbed (+) end and ADP-actin at the pointed (-) end. As ADP-actin is less stable, it spontaneously dissociates[61]. In steady state, actin filaments maintain a constant overall length since, while ATP-bound G-actin is constantly added to the barbed (+) end, ADP-bound G-actin dissociates from the pointed (-) end. This results in a constant flow of monomers through the static filament, evoking the idea of a treadmill. This treadmilling behavior is crucial during cell migration, as it allows actin flows to push the cell membrane forward.

Actin polymerization is regulated by specific proteins that interact with either G-actin or F-actin (Figure 2B). For example, profilin regulates actin polymerization via interaction with G-actin. It binds to ATP-bound G-actin, promoting elongation at the barbed (+) end, and acts as a nucleotide exchange factor by catalyzing the exchange of ADP for ATP in actin monomers, preparing them for another round of filament assembly[62,63]. On the other hand, formins or Ena/VASP proteins interact with F-actin. While formin attachment to the barbed (+) ends promotes efficient monomer addition - a process that is enhanced by profilin - Ena/VASP proteins support continuous filament elongation by protecting the growing ends by capping. Indeed, capping is an effective way to inhibit polymerization as the binding of a protein, such as CapZ, to the end of an actin filament blocks both the addition and loss of actin monomers[64]. Actin polymerization can also be inhibited by Thymosin-β4. Since Thymosin-β4 and profilin share the same binding site on G-actin, the binding of Thymosin-β4 sequesters G-actin and prevents its incorporation into growing filaments.

Actin filaments can also be modulated by agents like ADF/cofilin, which specifically target ADP-actin and induce depolymerization at the pointed (-) end, or be stabilized by proteins like tropomyosins. Tropomyosin binding along actin filaments protects them from severing and depolymerizing proteins like ADF/cofilin, reducing filament turnover[65]. Orchestration and coordination of all these players result in a fast turnover – rapid assembly and disassembly – making actin filaments ideal to quickly reorganize in response to external cues to drive cell migration.

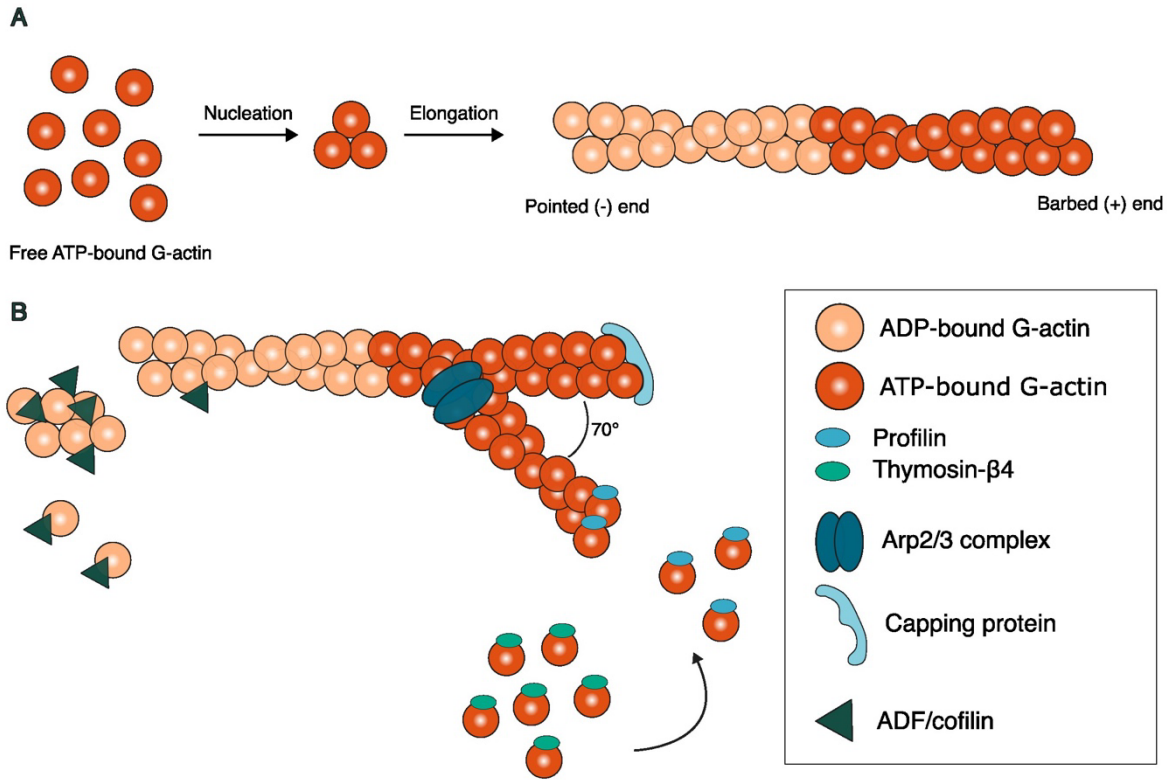

Figure 2. Principles of actin polymerization. A. *Scheme shows how trimers of ATP-bound actin monomers result in formation of an actin filament. ADP-bound actin monomers accumulate at the pointed (-) end, while ATP-bound monomers are found at the barbed (+) end, where elongation occurs.* ***B.*** *Scheme shows how profilin and thymosin-ß4 interact with actin monomers, and how Arp2/3, capping proteins and ADF/cofilin interact with actin filaments.*

1.7 Actin polymerization against the membrane drives leading-edge formation

How can a growing polymer exert mechanical force against an obstacle like the plasma membrane? Peskin et al. (1993) formulated "the Brownian ratchet" model, in which they propose that cell membranes undergo thermal (Brownian) fluctuations that create temporary gaps between the membrane and the tip of a growing actin filament. When the gap is large enough, an actin monomer can be inserted at the barbed (+) end of the filament. Filament elongation prevents the membrane from returning it its initial position, effectively ratcheting the system forward[66]. As the process repeats, the membrane gets successively pushed, resulting in protrusion of the cell front. Later, building up from this initial idea, it was proposed that actin filaments, instead of being rigid structures, are flexible and capable of storing elastic energy. As thermal fluctuations create room at the tip of the barbed (+) end of the actin filament, the filament bends and stores elastic energy. The elastic restoring force of the filaments straightening against the membrane delivers a propulsive force that results in a smoother and more efficient deformation of the membrane even under higher loads. This extended model is called "the elastic Brownian ratchet" model[67].

Although actin polymerization against the cell membrane is enough to initiate protrusion formation, activation of Rac1 or Cdc42 at the leading edge results in two distinct

morphological structures, as different sets of proteins confer different geometrical properties to the actin filament network.

Rac1, through WASP-family verprolin homologous (WAVE) proteins, promotes the formation of a broad, densely packed network of short, branched actin filaments. This type of network is best exemplified in fish and amphibian keratocytes, which assemble large, flat lamellipodia, which are ideal for visualization by both light and electron microscopy. In these cells, it has been shown that the WAVE complex attaches to the pointed end of a pre-existing actin filament (mother filament) where it recruits and activates the Arp2/3 complex, triggering nucleation of a new filament. The new filament is nucleated at a 70° angle from the mother filament[68,69] (Figure 2B), generating very thin sheet-like structures filled with a branched actin network. This organization was also observed in mammalian tissue culture cells[69,70] (Figure 3A).

On the other hand, Cdc42 activation at the membrane generates quite different actin structures. Stimulation of the Arp2/3 complex via WASp/N-WASp is one of the best-characterized effects of Cdc42 signaling. As described before, Arp2/3 activity results in highly-branched actin arrays. It has been shown that fibroblasts devoid of WASp/N-WASp, upon Cdc42 stimulation, generate thin, finger-like protrusions called filopodia that are filled with tight parallel bundles of F-actin[71]. Filopodia formation is dependent on formins, which induce the formation of unbranched actin filaments by promoting nucleation and elongation of barbed (+) end filaments[72], in coordination with ENA/VASP-family proteins, which prevent capping of the barbed ends of actin filaments[73]. In addition, motor proteins like Myosin X or fascin, an actin filament-bundling protein, confer mechanical cohesion to these F-actin bundles[74] (Figure 3B).

Contraction of the actin network can also lead to protrusion formation. In this case, protrusion formation is dependent on the activity of myosin II present in the actin cortex, which is closely attached to the plasma membrane of eukaryotic cells. Disruption of the normal membrane-cortex attachment is often a consequence of increased actomyosin contractility via the RhoA-ROCK-myosin II pathway. Phosphorylation of MLC leads to activation of myosin II. Myosin II binds to two independent actin filaments, and upon activation, slides them past one another, contracting the filaments and generating tension within the network. When these forces become too strong, they induce mechanical stress that can rupture the cortex or weaken the connections between the cortex and the membrane. The result is a weakened or detached membrane which, due to the hydrostatic pressure caused by actomyosin contraction, is pushed outwards, forming a protrusion called bleb[75,76]. These structures are transiently devoid of an actin cortex and are rapidly filled with cytosol. Within 10 to 20 seconds, a new actin cortex assembles under the bleb membrane, myosin II is again recruited and activated, retracting the bleb[75] (Figure 3C). How blebbing can be translated into forward movement is still unclear; however, it has been suggested that this mode of migration might be very similar to a lamellipodium-driven movement dependent on a highly contractile cell rear. First, cells need to generate a bleb at the cell front; the bleb should expand, pushing the membrane forward and, while the cortex is rebuilt at the cell front, contraction of the rear pushes the cell body forward.

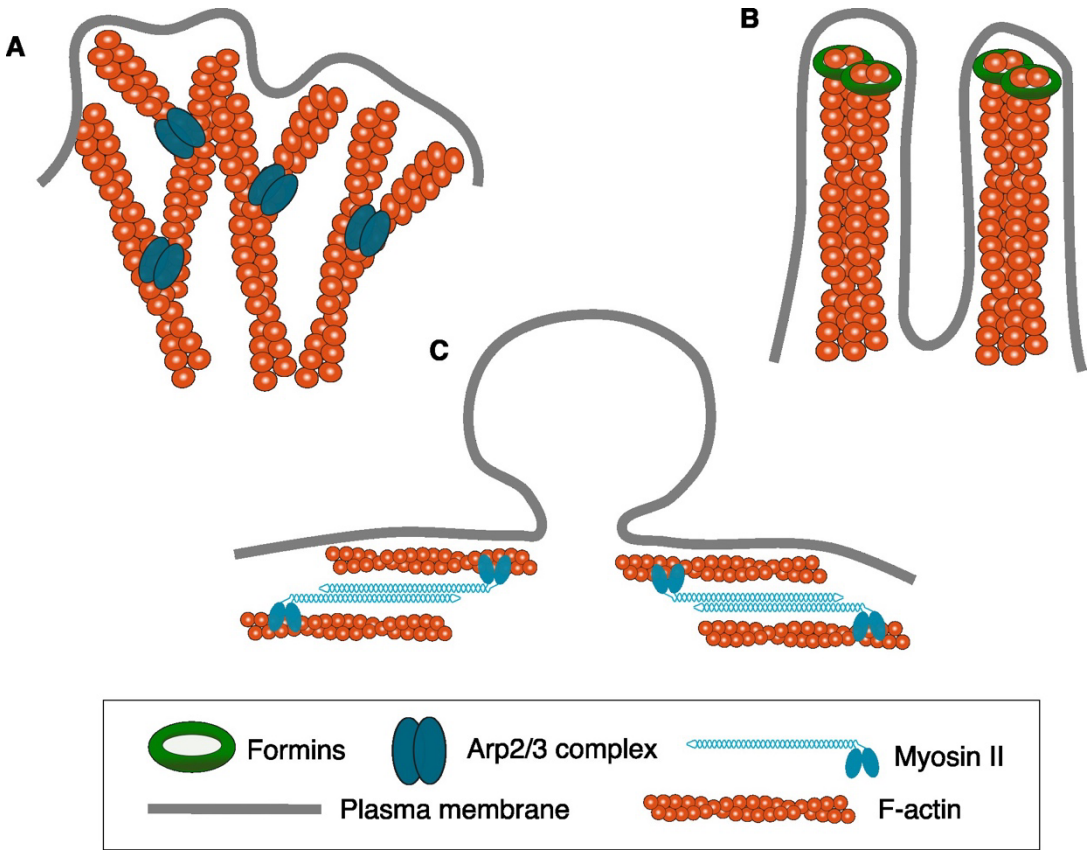

Figure 3. Scheme shows how actin polymerization against the membrane generates morphological distinct structures. A. *Lamellipodium formation is regulated by Rac1 through WAVE mediated Arp2/3 activation which generates an array of branched actin filaments.* ***B****. Filopodia formation is regulated by Cdc42 through WASp dependent Arp2/3 activation, resulting in bundled actin filaments.* ***C.*** *Myosin II dependent contraction of the actin network can also lead formation of protrusion called blebs. Adapted from "Actin dynamics in cell migration".*

1.8 From leading edge formation to locomotion

Although actin polymerization against the membrane is enough to generate a lamellipodium, locomotion requires the coordinated activity of the actin cytoskeleton to generate forces to initiate and propel forward movement. The basic concepts that characterize force generation and transmission are surprisingly conserved, even though cells can employ quite different locomotion strategies according to their surrounding environment.

1.8.1 2-dimensional (2D) vs 3-dimensional (3D) migration

Migration in two-dimensional (2D) substrates is by far the best understood. The classical model, that was first described in 1980 by Abercrombie, simplifies cell migration to three essential steps: (1) extension of a leading-edge protrusion forward; (2) stabilization of the leading edge by attachment to the substrate, mainly via specific transmembrane proteins like integrins; and finally (3) contraction of the rear of the cell and resolution of the adhesion sites. Based on his observations of fibroblasts migrating on glass, Abercrombie proposed that the addition of material to the cell front could generate a reward flux that, when mechanically

coupled to the substrate, could propel the cell forward[77]. Indeed, today we know that the addition of actin monomers at the tip of actin filaments at the leading edge simultaneously pushes the membrane forward and the filaments toward the cell center, generating an F-actin retrograde flow. This retrograde flow is further supported by myosin II mediated actin contraction that happens at the rear of the cell, and can be enhanced by coupling to the substrate via transmembrane proteins[78]. Thus, cells migrating in 2D are required to keep a tight balance between adhesion and contraction to efficiently generate traction forces parallel to the cell membrane, but opposite to the direction of movement, for effective forward locomotion.

Since the initial observations of Abercrombie, 2D cell migration has been reported in more physiological contexts. Single epithelial cells migrate along 2D sheets of basement membranes during organogenesis[79], and leukocytes patrol along the luminal surface of blood vessels[80]. This migration mode has also been observed in the collective migration of skin epithelial cells during wound healing[81]; however, this mode of migration is rather the exception than the rule.

Most cells exist and migrate within a three-dimensional (3D) environment composed of extracellular matrix (ECM) and other cells. The balance between these components and the specific composition of the ECM determines the mechanical properties of the environment surrounding a migrating cell. While fibrillar molecules, such as collagen and elastin, confer tensile strength and resilience to the environment, glycosaminoglycans and proteoglycans, like decorin, biglycan, or fibromodulin, make tissues more resistant to compressive forces, similar to hydrogels[82,83]. In addition, adhesive glycoproteins (e.g., fibronectin, laminin, and tenascin), as the name suggests, provide adhesive properties[82]. The combination of all these components dictates not only the geometry, alignment, density, and resulting pore size of the ECM, but also its deformability and rigidity[84], imposing challenges for migrating cells.

Indeed, cells have developed different migratory modes to overcome the challenges imposed by the complex 3D environment surrounding them. Their migratory behavior can be categorized into three major modes: mesenchymal, amoeboid, and lobopodial.

1.8.2 Mesenchymal migration

Mesenchymal migrating cells, such as fibroblasts and epithelial cells, share characteristics with classical 2D migration. They rely on actin polymerization at the leading edge to form a lamellipodium and establish strong interactions with the surrounding environment. In 3D settings, these cells take advantage of their robust adhesions to the ECM to circumvent the physical constraints of the environment. This strong attachment allows them to transiently remodel the ECM, creating sufficient space for the cell body to move forward - a process mainly mediated by integrins. Integrins are transmembrane proteins formed by two non-covalently binding subunits (alpha and beta subunits) with short intracellular domains. These proteins work as switches that can be activated, for example, by the binding of an external protein. Activation induces conformational changes at the intracellular domain of integrins that shift the protein from a low to a high-affinity and active binding state, promoting the binding of adaptor proteins, such as talin, which mediates interaction with the actin cytoskeleton[85,86]. Forming and breaking adhesions is coupled to the assembly and disassembly of actin attachments inside the cell, which can sometimes slow down movement. However, this active connection between the ECM and the actin cytoskeleton allows cells to

generate forces within their environment. This process is facilitated by the contractile actin network, which pulls these adhesion sites inward toward the cell body, creating openings large enough for the cell body to pass through[87–89]. Depending on the characteristics of the ECM, pulling and stretching can store elastic energy. Cells can take advantage of that by using the ECM as a slingshot: when adhesions are released, the stored energy recoils, propelling them through narrow spaces[90].
Whenever transiently remodeling the ECM is not enough, mesenchymal cells can employ destructive methods. To generate a path, these cells upregulate and release different enzymes, like cathepsins, serine proteases, and/or matrix metalloproteinases (MMPs), that can degrade ECM molecules[91–93]. ECM degradation is intricately linked to the intracellular organelle organization of mesenchymal migrating cells. These cells typically position their microtubule organizing center (MTOC), often cases, the centrosome, and the Golgi apparatus ahead of the nucleus in the direction of the movement. Such spatial organization facilitates direct trafficking of MMP-containing vesicles to the leading edge of the cell, allowing precise secretion at sites where ECM degradation is needed[94,95].

1.8.3 Amoeboid migration

Contrary to mesenchymal cells, amoeboid migrating cells, such as leukocytes, neither have the capacity to proteolytic degrade nor strongly adhere to the surrounding ECM[96–98]. Instead, they prefer to adapt to the environment by deforming their own cell body.
In 3D environments, amoeboid cells generate movement through cycles of actin polymerization (forming lamellipodia) or by hydrostatic membrane blebs at the leading edge, in coordination with actomyosin contraction at the rear, mediated by the small Rho GTPase RhoA. As it was mentioned before, activation of RhoA at the back of the cell stimulates ROCK, which in turn promotes MLC phosphorylation and myosin II activation, resulting in actomyosin contractility[25]. This contractile force propels the cell body forward, and it is aided by the frictional forces generated with the substrate by the actin cytoskeleton's retrograde flow. Actin flow along the plasma membrane can effectively generate parallel forces that generate maximal friction and boost locomotion[99–101]. Additionally, these cells position the nucleus, the bulkiest organelle in a cell, in front of the MTOC and other organelles. In this configuration, cells can probe the ECM looking for large enough pores to fit the cell body[102].
This mode of migration provides a significant advantage for cells such as leukocytes. The weak and transient interactions with the environment make this type of locomotion independent of the ECM composition, resulting in fast migration through a wide variety of tissue environments.

1.8.4 Lobopodial migration

The last, and also least studied mode of 3D migration is lobopodial migration, which can be seen as a hybrid between mesenchymal and amoeboid migration[95]. Lobopodial migration happens in tightly confined spaces. Under these circumstances, similar to some amoeboid cells, lobopodial migrating cells heavily rely on actomyosin contractility that pushes their nucleus forward. Nuclear positioning is crucial as it pressurizes the cell front, creating a bleb-like, cylindrical protrusion at the leading edge called lobopodia[103]. The intracellular pressure

generated by the combination of high confinement and nucleus positioning, coupled with the strong interactions with the surrounding ECM, propels these cells forward[103,104,95].

1.9 Plasticity within migration modes

While it is generally accepted that the choice of locomotion behavior is cell-type dependent, it is now established that, in more physiological environments, cells can flexibly adopt different migration strategies.

Literature is abundant in examples of mesenchymal to amoeboid (and even lobopodial) transitions. For instance, it has been shown that if the pathways that regulate the cell-ECM interactions are impaired or if proteolytic capacity is downregulated and degradation is hindered, mesenchymal migrating cancer cells can switch towards amoeboid migration[91,105,106]. Another set of studies in sarcoma cells showed that overexpression of constitutively active ROCK causes cortical contraction and cell rounding of these typically mesenchymal migrating cells. As a result, these cells migrate using either their small filopodia or bleb-like protrusions and mainly rely on actomyosin contractility, evoking amoeboid migration[107,108]. In many cancer cells, mesenchymal to amoeboid migration mode transitions are reversible when external conditions are favorable[109,110].

An even more fascinating case are fibroblasts. When migrating in 2D environments, these cells adopt the lamellipodium-driven migration as described by Abercrombie. If embedded in 3D collagen matrices, they resort to a 3D lamellipodium-based migration. However, in a 3D cell-derived matrix, cells show a 3D lobopodial migration[111,112].

In sum, when studying 3D cell migration, instead of trying to strictly categorize migration as mesenchymal, amoeboid, or lobopodial, we should focus on the balance between adhesive, contractile, and protrusive forces generated by cells within specific environments. This balance ultimately determines the mode of migration a cell adopts.

2 Aims

The work presented in this thesis aims to understand how immune cells navigate geometrically complex environments, where even the biggest pore precludes cell body passage, while keeping cellular cohesion.

3 WASp triggers mechanosensitive actin patches to facilitate immune cell migration in dense tissues

This chapter appears in ful in *WASp triggers mechanosensitive actin patches to facilitates immune cell migration in dense tissues*, Gaertner, Florian et al. Developmental Cell, Volume 57, Issue 1, 47-62.e9, 2022. https://doi.org/10.1016/j.devcel.2021.11.024.

Article

Developmental Cell

WASp triggers mechanosensitive actin patches to facilitate immune cell migration in dense tissues

Graphical abstract

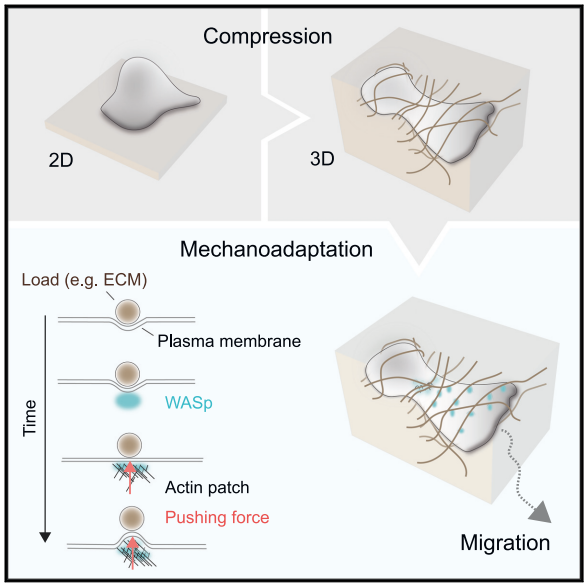

Authors

Florian Gaertner,
Patricia Reis-Rodrigues,
Ingrid de Vries, ...,
Walter Anton Kaufmann,
Robert Hauschild, Michael Sixt

Correspondence

florian.gaertner@ist.ac.at (F.G.),
michael.sixt@ist.ac.at (M.S.)

In brief

Gaertner et al. demonstrate that the actin cortex of immune cells is sensitive to mechanical load. In response to cellular indentation, Wiskott-Aldrich syndrome protein (WASp) triggers the formation of actin patches that polymerize orthogonal to the plasma membrane. Actin patches generate local pushing forces facilitating forward locomotion in obstructive tissues.

Highlights

- WASp drives cortical actin patch formation in response to mechanical load
- Actin patches polymerize orthogonal to the plasma membrane
- Actin patches locally push against obstacles to create space for locomotion

Gaertner et al., 2022, Developmental Cell *57*, 47–62
January 10, 2022
https://doi.org/10.1016/j.devcel.2021.11.024

CellPress

Developmental Cell

CellPress
OPEN ACCESS

Article

WASp triggers mechanosensitive actin patches to facilitate immune cell migration in dense tissues

Florian Gaertner,[1,*] Patricia Reis-Rodrigues,[1] Ingrid de Vries,[1] Miroslav Hons,[2] Juan Aguilera,[1] Michael Riedl,[1] Alexander Leithner,[1] Saren Tasciyan,[1] Aglaja Kopf,[1] Jack Merrin,[1] Vanessa Zheden,[1] Walter Anton Kaufmann,[1] Robert Hauschild,[1] and Michael Sixt[1,3,*]

[1]Institute of Science and Technology Austria, 3400 Klosterneuburg, Austria
[2]BIOCEV, First Faculty of Medicine, Charles University, Vestec, Czech Republic
[3]Lead contact
*Correspondence: florian.gaertner@ist.ac.at (F.G.), michael.sixt@ist.ac.at (M.S.)
https://doi.org/10.1016/j.devcel.2021.11.024

SUMMARY

When crawling through the body, leukocytes often traverse tissues that are densely packed with extracellular matrix and other cells, and this raises the question: How do leukocytes overcome compressive mechanical loads? Here, we show that the actin cortex of leukocytes is mechanoresponsive and that this responsiveness requires neither force sensing via the nucleus nor adhesive interactions with a substrate. Upon global compression of the cell body as well as local indentation of the plasma membrane, Wiskott-Aldrich syndrome protein (WASp) assembles into dot-like structures, providing activation platforms for Arp2/3 nucleated actin patches. These patches locally push against the external load, which can be obstructing collagen bers or other cells, and thereby create space to facilitate forward locomotion. We show *in vitro* and *in vivo* that this WASp function is rate limiting for ameboid leukocyte migration in dense but not in loose environments and is required for traf cking through diverse tissues such as skin and lymph nodes.

INTRODUCTION

Cells embedded in tissues are tightly confined by complex three-dimensional (3D) microenvironments. These can be dense fibrillar networks as in mesenchymal interstitia such as the dermis or cell-packed environments such as organ parenchyma or lymphatic tissues (Weigelin et al., 2016). Due to the limited availability of open space in such environments, cells frequently experience compressive loads from their surroundings, which is particularly relevant for cells that actively migrate.

Single-cell migration is an almost ubiquitous phenomenon in eukaryote biology and follows a continuum of biophysical strategies, with the mesenchymal mode on one pole and the ameboid mode on the other (Friedl and Wolf, 2010). Ameboid cells, such as metastatic cancer cells or leukocytes, migrate much faster and are more autonomous from their extracellular environment than mesenchymal (or epithelial) cells and rather than remodeling their environment they adapt to it (Paluch et al., 2016). Survival and locomotion of ameboid cells do not depend on adhesive ligands, and they migrate efficiently even in ectopic environments or artificial materials (Lämmermann et al., 2008; Reversat et al., 2020). The quick shape changes that ameboid cells owe their name to (Amoeba, from Greek *amoibe*, meaning ''change'') are entirely autonomous from the environment and the cellular envelope behaves as an active surface that rapidly deforms even when the cell floats in suspension (Barry and Bretscher, 2010).

These active adaptations of cell shape seem necessary to negotiate tissues, as ameboid cells do not digest their environment in order to create a path. Instead, in obstructive environments with heterogeneous geometry they effectively seek the path of least resistance choosing larger pores over small ones (Renkawitz et al., 2019). Whenever there is no other choice and the cell faces a small pore, it actively deforms its cell body and/or transiently dilates the pore in order to pass through (Pflicke and Sixt, 2009; Thiam et al., 2016; van den Berg et al., 2019). However, how ameboid cells generate forces underlying these processes is incompletely understood.

In animal cells, most intracellular forces are generated by the actin cytoskeleton, which produces pulling forces via actomyosin contraction and pushing forces via actin polymerization. Both pulling and pushing forces are tightly regulated by mechanical feedback. In order to test the geometrical and mechanical features of its surrounding, mesenchymal cells probe their substrate by pulling on it (Plotnikov and Waterman, 2013). To do so, they use their integrin-mediated adhesion sites as mechanosensitive organelles, which emit signals in response to traction force. Substrate probing by pulling forces seems less relevant for leukocyte migration. Whenever they move in an adhesion-free mode there is clearly no opportunity to pull. Also, whenever

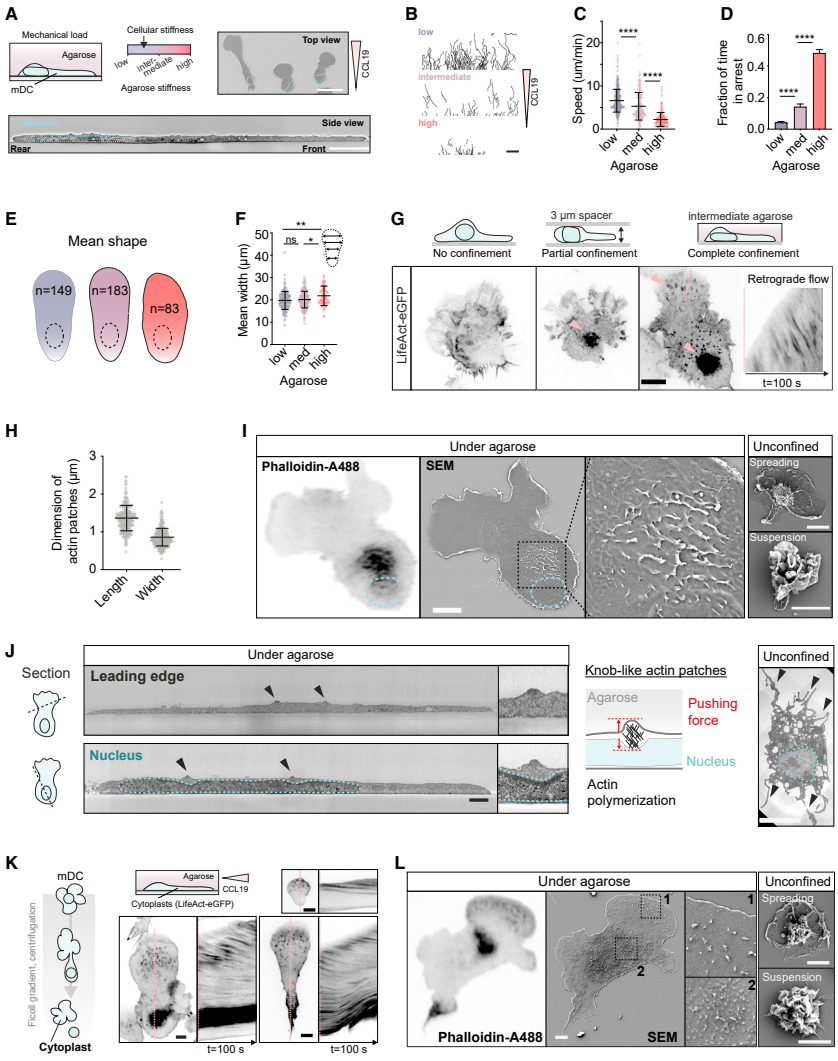

Figure 1. Dendritic cells form actin patches in response to restrictive environments

(A) Con nement of dendritic cells (DCs) under agarose. Agarose stiffness is adjusted around cellular stiffness (also see Figure S1A). Top view: SEM; scale bar, 50 µm. Side view: SEM image of a sagittal section; scale bar, 5 µm.

(B) Plot of single-cell tracks from representative experiments (Δt = 40 min); scale bar, 200 µm.

(C) Mean track speed. Each data point represents one track. Low agarose stiffness: n = 407 pooled from 6 experiments; intermediate agarose stiffness: n = 182 pooled from 4 experiments; high agarose stiffness: n = 205 pooled from 4 experiments; Kruskal-Wallis/Dunn s multiple comparisons test; ****p < 0.0001; mean ± SD. Also see Figure S1B.

(D) Fraction of time in arrest was extracted from tracks in (C); mean ± SEM; Kruskal-Wallis/Dunn s multiple comparisons test; ****p < 0.0001.

(E and F) Mean shape of cell contours (E). Contours were further analyzed for mean cell width along the centerline (F). Kruskal-Wallis/Dunn s multiple comparisons test; *p = 0.0189; **p = 0.0016. ns, not signi cant. Mean ± SD.

(legend continued on next page)

leukocytes do use adhesion receptors to generate friction with the substrate, they minimize traction: they tune their integrins so that they just transmit the extremely small traction forces required to move the cell body forward (Hons et al., 2018).

Pushing forces are generated whenever actin laments polymerize against the plasma membrane (Mogilner, 2006). The prototypic pushing structure is the lamellipodium, the at actin protrusion that forms the leading front of most ameboid and mesenchymal cells (Krause and Gautreau, 2014). Lamellipodial actin can adapt its protrusive force to the counterforce it experiences, making the tip of a cell mechanosensitive (Heinemann et al., 2011). However, lamellipodia are strictly two-dimensional (2D) lea ets, and the molecular machinery that drives actin polymerization at the lamellipodial tip does not support growth in the third dimension (Fritz-Laylin et al., 2017b, 2018). Hence, lamellipodia can protrude into open spaces, but they are insuf cient to create the active surface of an ameboid cell that adapts and deforms in 3D. In order to do that, the cell requires both mechanical sensitivity and activity across its whole cortex and not only at its lamellipodial tips. Here, we use dendritic cells (DCs) and T cells as model systems to address how ameboid cells respond to geometrical constraints of their environment. We investigate how these constraints are met by the molecular machinery that drives actin polymerization across the cellular cortex.

RESULTS

Dendritic cells form actin patches in response to restrictive environments

To study how ameboid cells respond to compressive loads, we observed the migratory behavior of dendritic cells (DCs) under a patch of non-degradable agarose cast on a serum-coated coverslip (Hons et al., 2018) (Figure 1A). In this reductionist approach, no pre-formed space is available and the highly at-tened cells need to actively lift and deform the agarose to create suf cient space between coverslip and agarose to move forward (Figure 1A) (Laevsky and Knecht, 2003). To control the mechanical load that the cells have to counter, we adjusted the stiffness of the agarose around the range of cellular stiffness as measured by atomic force microscopy (AFM) (Blumenthal et al., 2020; Guimaraes et al., 2020) (Figures 1A and S1A). With increasing stiffness, the mean migratory speed declined (Figures 1B, 1C, and S1B) and the cells shifted from continuous locomotion to a stop and go pattern where cells collapsed and stalled after short periods of movement (Figure 1D; Video S1). Notably, time spent in arrest rose only slightly from low (2.5 kPa; below cellular stiffness) to intermediate (10 kPa; slightly exceeding cellular stiffness) but drastically at high agarose stiffness (17.5 kPa) (Figure 1D). Morphometric analysis of average cell shape revealed that at low and intermediate load, DCs adopted an elongated shape with a wide leading edge and a slender cell body (Figure 1E; Video S1). Only under high load, average cell shape became substantially widened (Figures 1E, 1F, and S1C). These data indicate that DCs can successfully counter restrictive environments of stiffnesses that are in the range of cellular stiffness but frequently collapse when external load becomes exceedingly high.

When migrating under intermediate-stiff agarose LifeAct-eGFP expressing DCs displayed small actin-rich patches embedded in a homogeneous actin cortex. These patches were scattered across the whole cell, with peak intensities in the cell body (Figure 1G; Video S1). Notably, actin patches were restricted to regions of cellular con nement (Figure 1G; Video S1), formed independent of myosin II activity (Lomakin et al., 2020; Venturini et al., 2020) (Figure S1D) and were not sites of clathrin- or caveolin-mediated endocytosis (Ferguson et al., 2017) (Figures S1E S1G). Actin patches were independent of adhesive interactions with the substrate as they were equally pronounced when cells migrated between (inert) agarose and passivated coverslips (Figure 1G; Video S1). DCs migrating under non-adhesive conditions display a substantial retrograde ow of actin as both cortical and lamellipodial actin slide backward in relation to the substrate (Renkawitz et al., 2009). Actin patches moved together with this bulk actin ow, indicating linkage of the patches to the rest of the actin cortex (Figures 1G and S1H). Over time, patches occasionally evolved into elongated stripes (Figures 1H and S1I; Video S1). Confocal z scans as well as correlated light and scanning electron microscopy (CLEM) indicated that patches and stripes corresponded to short knob- or ridge-like surface structures that protrude normal to the imaging plane into the agarose (Figures 1H, 1I, and S1J). Ultrastructural analysis of serial sections suggested that these knobs generated vertical pushing forces: when actin knobs were located on top of the nucleus, the protrusions into the agarose overlay were mirrored by an indentation in the nuclear lamina (Revach et al., 2015) (Figure 1J). Supporting this notion, visualization of the cell-substrate interface by interference re ection microscopy (IRM) revealed that actin patches were, despite the lack of cell-substrate adhesions, in closer proximity to the underlying substrate than the surrounding ventral membrane (Yu et al., 2013) (Figure S1K). Collectively these experiments suggest that cells con ned under a

(G) Actin patches (LifeAct-eGFP) form in response to con nement. Representative images from spinning disk confocal microscopy movies of live cells on PMOXA-coated (non-adhesive) coverslips (con ned cells). Uncon ned cells adhere to PLL-coating. Kymograph shows retrograde actin ow. Notably, actin patches move with the bulk actin ow.

(H) Dimensions of actin patches were quanti ed from confocal z stacks (also see Figure S1J); n = 246 pooled from 7 cells (mean ± SD).

(I) Correlative light (epi uorescence) and (scanning) electron microscopy (CLEM). Note, LifeAct-eGFP signal correlates with knob- and ridge-like protrusions. Right panels: SEM of uncon ned cells (spreading and in suspension). Scale bars, 10 μm.

(J) Ultrathin section analyzed by SEM. Upper panel: section across the leading edge. Lower panel: section across the cell body with nucleus. Notably, knobs (black arrow heads) form orthogonally to lamellipodia and indent the agarose. Mirrored indentations are visible in the nuclear lamina, indicating pushing forces generated by knobs (see magni ed SEM images and scheme of a single actin knob). Scale bar, 1 μm. Right: TEM of ultrathin section of mDC in suspension. Uncon ned cells form multiple lamellipodial veils (arrow heads) but lack knob-like protrusions of con ned cells.

(K) Nucleus-free cytoplasts migrating under agarose form actin patches (spinning disk microscopy) correlating with knob-like protrusions (SEM).

(L) Of note, cytoplasts resemble the morphology of intact cells both under con nement and during uncon ned spreading or in suspension; scale bars, 5 μm (L). Also see Figure S1 and Video S1.

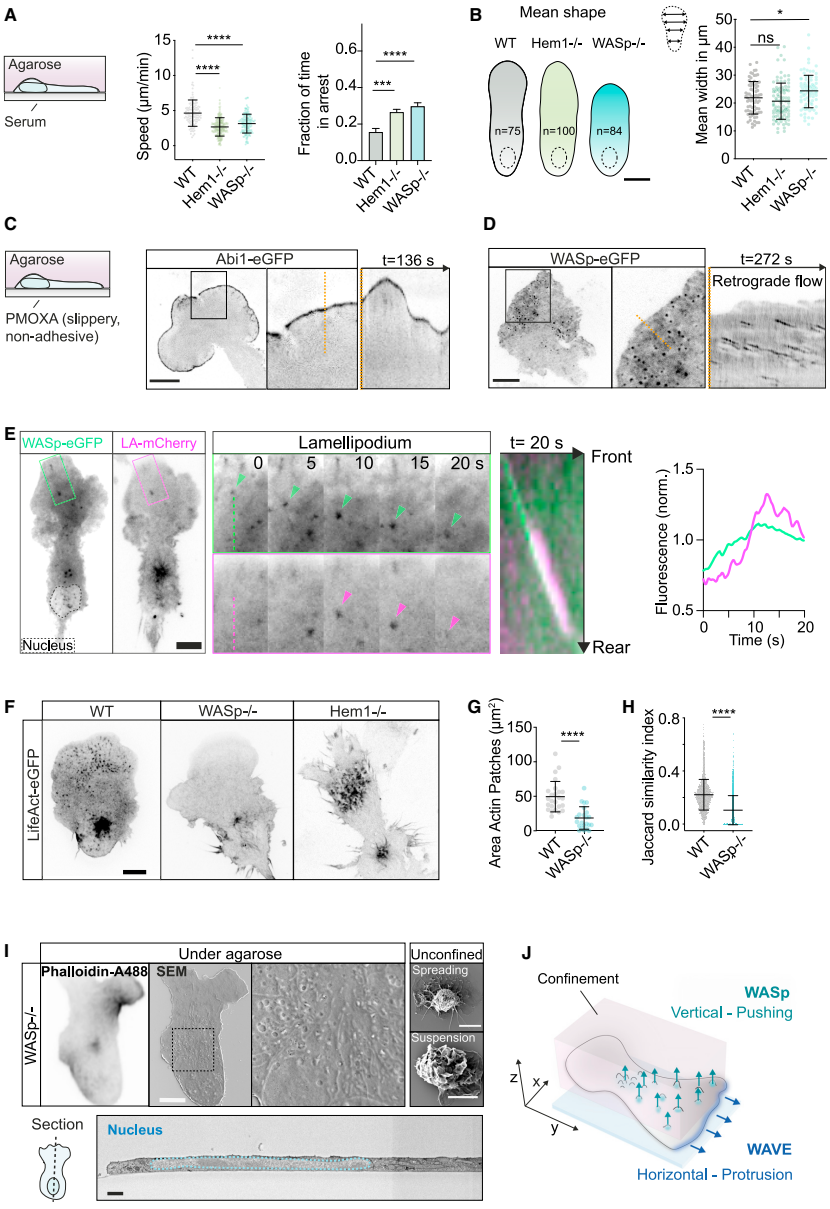

(legend on next page)

restrictive overlay respond by forming cortical actin patches that push against the compressive load.

We next tested if the nucleus is required for the formation of actin patches and generated nucleus-free cytoplasts by gradient ultracentrifugation (see STAR Methods) (Figures 1K, 1L, and S1L). Cytoplasts were viable for hours and resembled intact cells in morphology and function (Figures 1K, 1L, and S1L). When migrating under a patch of intermediate-stiff agarose cytoplasts formed actin patches that were scattered over the entire projected cell area and showed an actin ow pattern similar to intact cells (Figure 1K; Video S1). Importantly, cytoplasts accumulated prominent actin patches in the area corresponding to the perinuclear region of intact cells. Similar to intact cells CLEM revealed that actin patches correspond to short knobs on the surface of cytoplasts that grow normal to the imaging plane (Figures 1L and S1L). Together these data con rm that actin patches triggered by con nement can evolve independent of the presence of a nucleus.

WASp-driven actin patches grow orthogonal to WAVE-driven lamellipodia

Formation and dynamics of cortical actin heavily depends on the Arp2/3 nucleation complex (Bovellan et al., 2014; Laplaud et al., 2021). Upon pharmacological inhibition of Arp2/3 with CK666 actin patches in DCs under intermediate-stiff agarose were abolished, and treated cells spent most of their time in arrest (Figure S2A). We therefore compared the contribution of the two main nucleation-promoting factors (NPFs) upstream of Arp2/3: Wiskott-Aldrich syndrome protein (WASp) and WASp-family verprolin-homologous protein (WAVE) (Rotty et al., 2013). To this end, we analyzed DCs de cient in WASp or the WAVE complex subunit Hem1, which in hematopoietic cells is essential for the stability of the pentameric WAVE complex (Leithner et al., 2016). Both mutants showed reduced migration speeds and increased time in arrest under agarose of intermediate stiffness (Figures 2A and S2B; Video S2), while chemotaxis toward CCL19 was not affected (Leithner et al., 2016; Weiner et al., 2007) (Figure S2C). Hem1$^{-/-}$ DCs were devoid of lamellipodia and formed multiple, spiky protrusions at the leading edge (Figure S2D), while WASp$^{-/-}$ DCs formed normal lamellipodia (Figure S2D). Morphometric analysis showed that despite their spiky protrusions the mean overall cell body shape of Hem1$^{-/-}$ cells was comparable to WT cells, while WASp$^{-/-}$ cells were signi -cantly wider and shorter (Figure 2B). Hence, regarding the shape and migratory pattern, WASp$^{-/-}$ cells under intermediate-load conditions phenocopied WT cells under high-load conditions (Figures 1B 1F).

Next, we were interested in the spatiotemporal organization of WAVE and WASp-dependent actin networks under compressive loads. While the WAVE complex (detected with Abi1-eGFP) strictly localized to the tip of lamellipodia (Leithner et al., 2016), WASp (detected with WASp-eGFP) formed dots scattered across the cell surface, matching the distribution and ow pattern of actin patches (Figures 2C 2E, and S2E; Video S2). Simultaneous monitoring of WASp-eGFP and LifeAct-mCherry revealed co-localization of both signals, with WASp dots preceding polymerization of actin patches by about 5 10 s (Figure 2E; Video S2). Accordingly, deletion of WASp, but not the WAVE complex abrogated formation of actin patches as revealed by LifeAct-eGFP signal (Figures 2F and 2G; Video S2), and the few actin patches remaining in WASp$^{-/-}$ DCs were transient and short-lived (Figures 2H and S2F; Video S2). Ultrastructural analysis of serial sections and CLEM con rmed the morphological absence of short knobs on the dorsal surface of WASp$^{-/-}$ DCs under con nement (Figure 2I), while there were no apparent morphological differences to WT cells in the absence of con nement (Figures 1I and 2I).

Together, these data reveal a characteristic organization of branched actin networks in 3D: while WAVE-driven actin nucleation powers the horizontal forward protrusive component of cellular locomotion, WASp-driven actin nucleation counters the mechanical load of the overlay (Figure 2J).

WASp-driven actin patches are triggered by mechanical load

We next addressed if WASp-driven actin patches form in response to a mechanical trigger or if they develop spontaneously. We seeded LifeAct-eGFP-expressing DCs on poly-L-Lysine coated coverslips and locally pinched the cell body with the blunted tip of a microneedle (Figure 3A). Within seconds after

Figure 2. WASp-driven actin patches polymerize orthogonal to WAVE-driven lamellipodia

(A) WASp$^{-/-}$ and Hem1$^{-/-}$ DCs were derived from bone marrow of transgenic mice. Left panel: WT: n = 118 pooled from 3 experiments; WASp$^{-/-}$: n = 175 pooled from 4 experiments; Hem1$^{-/-}$: n = 347 pooled from 6 experiments; mean ± SD; Kruskal-Wallis/Dunn s multiple comparisons test; ****p < 0.0001. Right panel: Fraction of time in arrest was extracted from tracks; mean + -SEM; Mann-Whitney test and Kruskal-Wallis/Dunn s multiple comparisons test; ****p < 0.0001.

(B) Mean shape of contours; WT: n = 75; Hem1$^{-/-}$: n = 100; WASp$^{-/-}$: n = 84. Mean cell width along the centerline; mean ± SD; Kruskal-Wallis/Dunn s multiple comparisons test; (g) *p = 0.0491; ns, not signi cant.

(C and D) TIRF microscopy of agarose-con ned DCs expressing (C) Abi-eGFP (to label the WAVE complex) or (D) WASp-eGFP. Note, while Abi1-eGFP is restricted to the lamellipodial tip, WASp-eGFP forms dot-like structures scattered across the cell body and moving with the retrograde ow; resembling LifeAct-eGFP signal (see Figure 1G). Scale bar, 10 μm.

(E) Dual labeling of LifeAct-mCherry and WASp-eGFP (TIRF microscopy); scale bar, 10 μm; also see Figure S2F.

(F) WT, WASp$^{-/-}$ and Hem1$^{-/-}$ DCs under intermediate-stiff agarose on PMOXA-coated (non-adhesive) coverslips. Representative images from spinning disk confocal microscopy movies (LifeAct-eGFP) of live cells are shown (also see Video S2). Notably, Hem1$^{-/-}$ DCs are devoid of lamellipodia but form prominent actin patches at the leading edge and the cell body. Scale bar, 10 μm.

(G and H) Quanti cation of area (G) and dynamics (H) of actin patches in WT and WASp$^{-/-}$ cells. Jaccard index measures frame-to-frame overlap of segmented actin patches (1 = 100% similarity).

(G) Area of actin patches. WT: n = 25 cells; WASp$^{-/-}$: n = 23 cells. Mean ± SD; Mann-Whitney; ****p < 0.0001.

(H) WT: n = 2,144 frames pooled from 25 movies; WASp$^{-/-}$: 2,055 frames pooled from 23 movies. Mean ± SD; Mann-Whitney; ****p < 0.0001.

(I) Ultrastructural analysis of WASp$^{-/-}$ DCs using CLEM (upper panel; scale bars, 10 μm) and SEM of an ultrathin section (lower panel; scale bar, 1 μm). While uncon ned WASp$^{-/-}$ cells morphologically resemble WT cells (Figure 1I), they do not form knob- and ridge-like structures upon con nement.

(J) Graphical summary. Also see Figure S2 and Video S2.

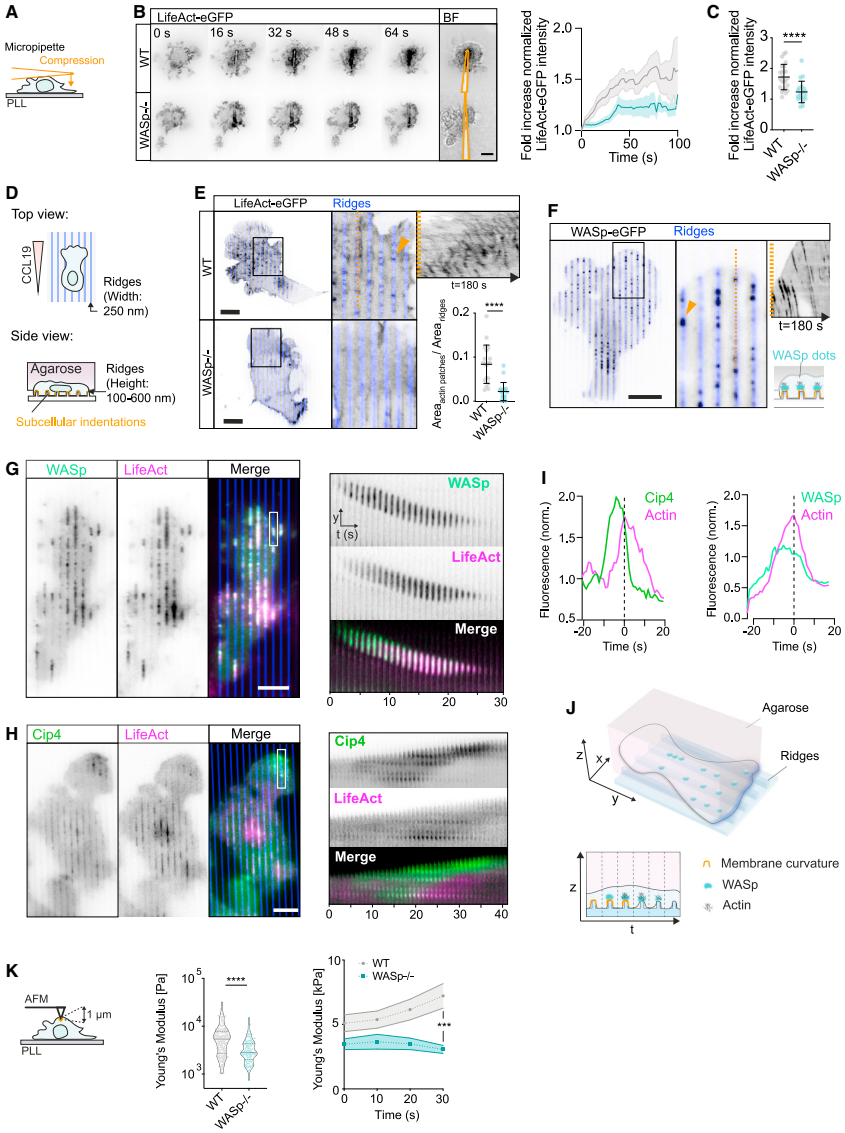

Figure 3. WASp-driven actin patches are triggered by mechanical loading

(A) DCs attached to poly-l-lysine (PLL)-coated coverslips were pinched from top with a microneedle (schematic). Micropipette was held in place during time-lapse recordings.

(B) Time traces (spinning disk confocal microscopy) of representative LifeAct-eGFP expressing DCs. The last frame shows an overlay of bright eld images of the micropipette (highlighted in orange). Right panel: time traces of LifeAct-eGFP signal at the site of micropipette indentation (normalized by mean LifeAct-eGFP signal of non-indented area). Intensity of rst frame was set to 1. WT: n = 24; WASp: n = 20; mean ± SEM. Scale bar, 10 µm.

(legend continued on next page)

indenting the cell, the actin reporter increased around the pipette tip of WT DCs, leaving behind a localized actin cloud (Gerard et al., 2014) (Figure 3B; Video S3). This mechanically induced burst of actin polymerization was substantially decreased in WASp$^{-/-}$ DCs (Figure 3C). This nding supported a role of WASp in polymerizing actin in response to mechanical loading (Figure 1G).

Migrating leukocytes constantly encounter submicron-sized obstacles such as collagen bers that restrict their passage and therefore locally indent the cell body. We mimicked this scenario *in vitro* and con ned cells onto inert substrates with a ridged topography matching the size of collagen brils (Figures 3D, S3A, and S3B). This setup allowed the precise localization of the uorescent signals. We found that ridges of 600-nm height (and 250-nm width) induced actin patches that matched the pattern of ridges (Figure 3E; Video S3). Notably, these patches exclusively formed on top of ridges and were virtually absent in the interjacent grooves (Figures 3E and S3C). This response was independent of adhesive interactions as actin patches formed ef ciently on passivated substrates, where they moved with the retrograde actin ow (Figure 3E). WASp-eGFP followed the same dynamic pattern, with sharply delineated dots precisely matching the ridge structure and preceding actin patch formation by 5 10 s (Figures 3F, 3G, and 3I; Video S3). In contrast, WAVE (detected with Abi1-eGFP) was not recruited to ridges but remained restricted to the very tip of the leading edge and occasionally to small lamellipodial protrusions forming within interjacent grooves (Figure S3D). While actin patches remained targeted to ridges after deletion of WAVE (Figure S3E), they were virtually absent after deletion of WASp (Figures 3E and S3C; Video S3). We rarely observed sparse formation of actin patches at the cell body of WASp-de cient DCs (Figure S3C), but these remnants were negative for Abi1-eGFP, arguing against a compensatory function (Veltman et al., 2012; Zhu et al., 2016) (Figure S3F). In summary, we demonstrate two non-interchangeable functions of WAVE and WASp in DCs: while WAVE drives explorative lamellipodial protrusions (Leithner et al., 2016), WASp is recruited to sites of cellular indentation where it remains on target to locally trigger actin polymerization.

Membrane curvature is a key upstream regulator of NPFs (Suetsugu and Gautreau, 2012). To analyze if curvature sensing acts upstream of WASp activation we transfected DCs with uorescently tagged Cip4, a F-BAR domain protein expressed in leukocytes, including DCs (Koduru et al., 2010). Cip4 enriched at the leading edge of con ned DCs and accumulated in dot-like structures preceding the formation of actin patches (Figure S3G). On topographic slides Cip4 formed clusters aligning with nanoridges and co-localizing with actin patches (Figure 3H). Similar to WASp, Cip4 preceded actin polymerization by approximately 10 s, but quickly dissociated from actin patches once actin polymerization reached its peak (Figures 3I and 3J).

Previous studies have shown that mechanical load can induce global stiffening of the cellular cortex, which is dependent on actin reorganization (Hu et al., 2019). To test if load-induced actin polymerization increases cortical stiffness in DCs we repetitively indented DCs immobilized on poly-L-Lysine with the tip of an AFM cantilever and measured cellular stiffness. WASp-de cient DCs showed a signi cantly reduced cortical stiffness, con rming previous reports (Blumenthal et al., 2020). While cortical stiffness gradually increased following repetitive indentation, this response was signi cantly blunted in WASp$^{-/-}$ cells, indicating a crucial role of WASp in adapting cell mechanics to mechanical load (Figures 3K and S3H). In summary, we demonstrate that cells respond to mechanical load by locally polymerizing actin, a process requiring WASp.

WASp-driven actin patches are negligible for the generation of cell-substrate friction under agarose

WASp de ciency was shown to alter integrin-dependent leukocyte functions (Zhang et al., 2006). Dependent on the availability of adhesive ligands, leukocytes can exibly shift between non-adhesive locomotion modes and modes where actin ow couples to the substrate via integrins (Hons et al., 2018). To test whether WASp and integrins lie in the same pathway we placed WASp$^{-/-}$ cells under intermediate-stiff agarose con nement on inert substrates (PMOXA coating). Similar to migration on adhesive (serum-coated) substrates (Figures 2A 2C), WASp$^{-/-}$ DCs were slower than WT cells and arrested frequently (Figure 4A), while adopting a rounded morphology (Figures 4B and S4A). This additive phenotype demonstrates that the contribution of WASp is neither upstream nor downstream of integrins but represents an independent mechanism. We saw that WASp-dependent actin

(C) Dot plot showing fold increase of LifeAct-eGFP intensity following indentation (last frame/ rst frame). Each data point is one indentation experiment (see B). Mean ± SD; Mann-Whitney test; ****p < 0.0001.
(D) Schematic shows DCs con ned on inert nano-ridges with 2 μm pitch (PMOXA coating) (see STAR Methods).
(E) Representative WT and WASp$^{-/-}$ DC migrating on nano-ridges. Notably, actin patches formed with high precision on top of ridges (also see Figure S3C). Arrow head indicates actin patches. Kymograph shows retrograde ow of actin patches. Fraction of ridges covered by actin patches (segmented in Ilastik) (also see Figure S3B). WT: n = 19 cells; WASp$^{-/-}$: n = 19 cells; Mean ± SD; Mann-Whitney test; ****p < 0.0001. Scale bar, 20 μm.
(F) Representative micrograph of WASp-eGFP-expressing DCs migrating on nano-ridges (width: 1 μm; height: 250 nm; pitch: 2 μm) (TIRF). WASp-eGFP shows same dynamic pattern as actin patches (kymograph) with sharply delineated dots matching the ridge structure. Scale bar, 20 μm.
(G) Dual labeling of LifeAct-mCherry and WASp-eGFP reveals co-localization on nano-ridges. Kymograph shows that WASp dots precede the formation of actin patches. Scale bar, 10 μm.
(H) Dual labeling of LifeAct-eGFP (false colored in magenta) and Cip4-mCherry (false colored in green) reveals co-localization on nano-ridges. Kymograph shows that Cip4 clusters precede the formation of actin patches. Scale bar, 10 μm.
(I) Cip4- and WASp dots precede actin patches. Time traces of uorescence intensities of kymographs shown in (G) and (H).
(J) Schematic summary showing the spatiotemporal sequence of actin patches formation on nano-ridges.
(K) Schematic of an AFM cantilever indenting a DC adherent to a PLL-coated coverslip. Left: using a Hertz contact mechanics model, the elastic modulus was estimated by tting the force indentation curves up to 1 μm. Each data point represents one measurement. WT: n = 160 from 37 cells (also see Figure S1A); WASp$^{-/-}$: n = 106 from 26 cells. For cellwise analysis see Figure S4F. Violin plot with median ± quartiles; Mann-Whitney test; ****p < 0.0001. Right: time series cellular response to repetitive indentations of the AFM cantilever (elastic modulus). WT = 35 cells; WASp$^{-/-}$ = 23 cells. Mean ± SEM; multiple t tests; ***p < 0.01. Also see Figure S3 and Video S3.

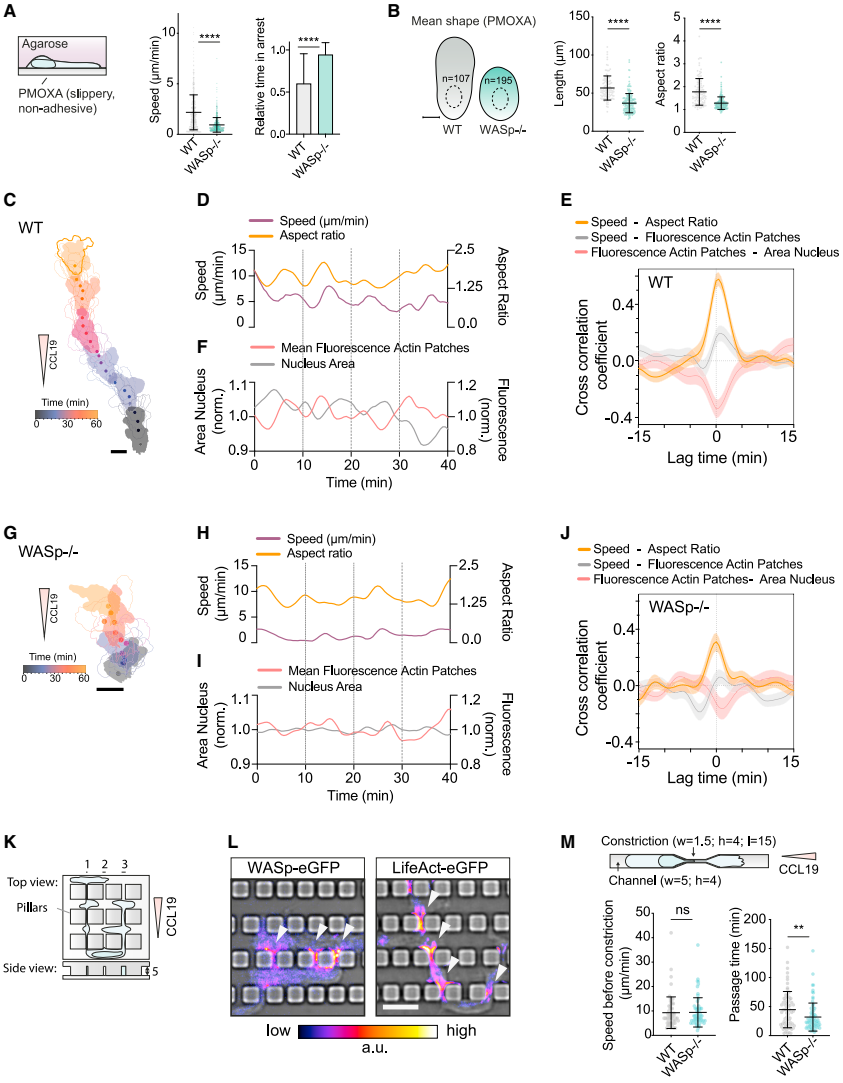

Figure 4. Vertical pushing facilitates locomotion by deforming restrictive environments

(A) Under agarose assay on inert PMOXA-coated substrates. WT: n = 642 pooled from 3 experiments; WASp$^{-/-}$: n = 597 pooled from 4 experiments; mean ± SD; Mann-Whitney test; ****p < 0.0001. Fraction of time in arrest was extracted from tracks; mean + SEM; Mann-Whitney test; ****p < 0.0001.

(B) Mean shape of contours; WT: n = 107; WASp$^{-/-}$: n = 195; mean cell width along the centerline and aspect ratio; mean ± SD; Mann-Whitney test; ****p < 0.0001.

(C) Representative color-coded WT DC outlines (time). Scale bar, 25 µm.

(D) Smoothed time traces of speed and aspect ratio extracted from WT DC contours (epi uorescence movies (LifeAct-eGFP); frame rate = 30 s).

(E) Cross-correlation between the (1) cell speed and aspect ratio, (2) cell speed and mean uorescence of actin patches, and (3) mean uorescence of actin patches and area of nucleus is shown (WT: n = 25 cells; mean ± SEM). The positive lag time (gray curve) means an increase in mean uorescence of actin patches precedes cell speed (also see Figures S4D S4F).

(legend continued on next page)

knobs at the dorsal surface of the cell occasionally reached into holes in the overlaying agarose (Figures 1I and S4B), raising the possibility that WASp function can compensate for lack of integrin-mediated adhesion. We therefore addressed if, in analogy to the molecular clutch model of integrins, actin patches can act as footholds that couple into the retrograde actin ow to generate traction forces (Figure S4C). The most sensitive readout for force-coupling in leukocytes is the rate of actin polymerization. Whenever cells slip due to a disengaged adhesive clutch, actin polymerization massively increases to compensate for the retrograde slippage (Hons et al., 2018; Maiuri et al., 2015; Renkawitz et al., 2009; Reversat et al., 2020). When we measured actin ow in WT versus WASp-de cient DCs on slippery, PMOXA-coated substrates, there was no sign of accelerated actin polymerization. In contrast, polymerization rates showed a slight drop (Figure S4C). These data indicate that the main function of WASp-dependent actin patches is not to generate traction tangential to the membrane but rather to facilitate protrusion by pushing orthogonal to the membrane.

Vertical pushing facilitates locomotion by deforming restrictive environments

The decrease in cell speed under mechanical load was accompanied by a change in cell shape (Figures 1E, 1F, and S1C). While WT cells were still able to maintain an elongated shape with a slender cell body in intermediate-stiff agarose, WASp$^{-/-}$ DCs were signi cantly shorter and had a widened cell body (Figures 2C, 4B, and S2D). To address if and how vertical pushing is embedded into the morphodynamic cycle of cellular locomotion, we next used a cross-correlation approach of cellular morphology. DCs migrating under agarose undergo repetitive phases of acceleration and deceleration with a mean phase duration of 4 5 min (Figures S4D and S4E). Acceleration of WT cells under agarose is initiated by leading-edge protrusion and elongation of the cell body (Figure 4C and 4D; Video S4). Accordingly, cross-correlating speed with aspect ratio revealed a clear positive and instantaneous correlation (Figures 4E and S4F). Incorporating the number of cortical actin patches into the correlation showed that patches preceded acceleration by 1 2 min (Figures 4E and 4F), indicating that patches facilitate rather than drive forward protrusion. We next measured nuclear-projected area as a proxy for how much a cell is able to lift the agarose: the nucleus of suspended DCs is approximately spherical, but naturally attens with increasing con nement, making it a good indicator of cell height (Lomakin et al., 2020) (Figures 1A, 1J, and S4G). WT DCs showed steady uctuations of nuclear-projected area when migrating under agarose (Figure S4H; Video S4). Nuclear area was negatively cross-correlated with the appearance of actin patches on the surface area of the cell (Figures 4E and 4F), supporting the concept that vertical WASp-driven protrusions lift the agarose so that the nucleus can expand vertically. Accordingly, cross-correlations between (residual) actin structures (Figure S4E) speed and projected nuclear area were blunted in WASp$^{-/-}$ DCs, while the speed to aspect ratio cross-correlation was retained (Figures 4G 4J; Video S4). This morphodynamic sequence suggested that actin patches are a prerequisite to lift and deform the agarose, which then facilitates forward protrusion.

We next tested if the WASp contribution to locomotion is indeed speci c for migration in deformable restrictive environments. We thus seeded DCs into PDMS-based (non-deformable) micro uidic devices large pore sizes (100-μm^2 cross-section). These can be passaged without substrate deformation. Here, migration parameters of WASp$^{-/-}$ mutants were indistinguishable from WT cells (Figure S4I; Video S4). Next, we reduced the pore sizes to cross-sections as small as 5 15 μm^2 (Figure 4K). DCs squeezing through these tight constrictions recruited WASp and actin to sites of compression (Figure 4L; Video S4), matching the observations under agarose. To functionally test if WASp-dependent pushing forces are required for squeezing through non-deformable constrictions (Thiam et al., 2016), we measured migration in channels with tight constrictions (6-μm^2 cross-section). Mean time of passage was not prolonged for WASp$^{-/-}$ compared with control cells but rather slightly reduced (Figure 4M). Together, we show that WASp-driven vertical pushing forces counter mechanical load and displace deformable microenvironments to generate space for the cell to enter into the protrusive phase of locomotion. Whenever the substrate is non-restrictive, WASp function is not required for locomotion. Whenever the substrate is restrictive but non-deformable, WASp is recruited but is not effective in facilitating locomotion.

Deformation of collagen bers is required for migration in brous environments

We next challenged our ndings in physiological environments. To initiate adaptive immunity, DCs need to migrate from the site of antigen retrieval to the draining lymph node (LN) (Worbs et al., 2017), which requires fast transit through diverse microenvironments. DCs can reach the LN without proteolytically generating a path (P icke and Sixt, 2009), suggesting that they predominantly use a mechanical strategy. We therefore adoptively transferred differentially labeled WT and WASp$^{-/-}$ DCs into footpads of WT recipients and measured homing to draining LNs (Figure S5A). After 24 h, recruitment of WASp$^{-/-}$ DCs was signi cantly reduced compared with WT controls, con rming previous reports by others and demonstrating physiological

(F) Smoothed time traces of area of nucleus (normalized by the mean of all time points) and mean uorescence of actin patches (normalized by the mean of all time points) of the same cell (see A and B).
(G) Representative color-coded WASp$^{-/-}$ DC outlines (time). Scale bar, 25 μm.
(H) Smoothed time traces of speed and aspect ratio extracted from WASp$^{-/-}$ DC contours (epi uorescence movies [LifeAct-eGFP]; frame rate = 30 s).
(I) Smoothed time traces of area of nucleus (normalized by the mean of all time points) and mean uorescence of actin patches (normalized by the mean of all time points) of the same cell.
(J) Cross-correlation analysis (also see E) (WASp$^{-/-}$: n = 22 23 cells; mean ± SEM).
(K) PDMS-based (non-deformable) micro uidic device with a constant height and constrictions.
(L) Representative images of WASp-eGFP- and LifeAct-eGFP-expressing cells squeezing through constrictions (TIRF). Arrow heads indicate increased uorescence at constrictions. Scale bar, 10 μm. (M) Mean speed of cells migrating in straight channels (mean ± SD; Mann Whitney test; p = 0.82) and passage time of constriction (mean ± SD; Mann Whitney test; **p < 0.01). Schematic shows dimension of micro uidic device in μm. Also see Figure S4 and Video S4.

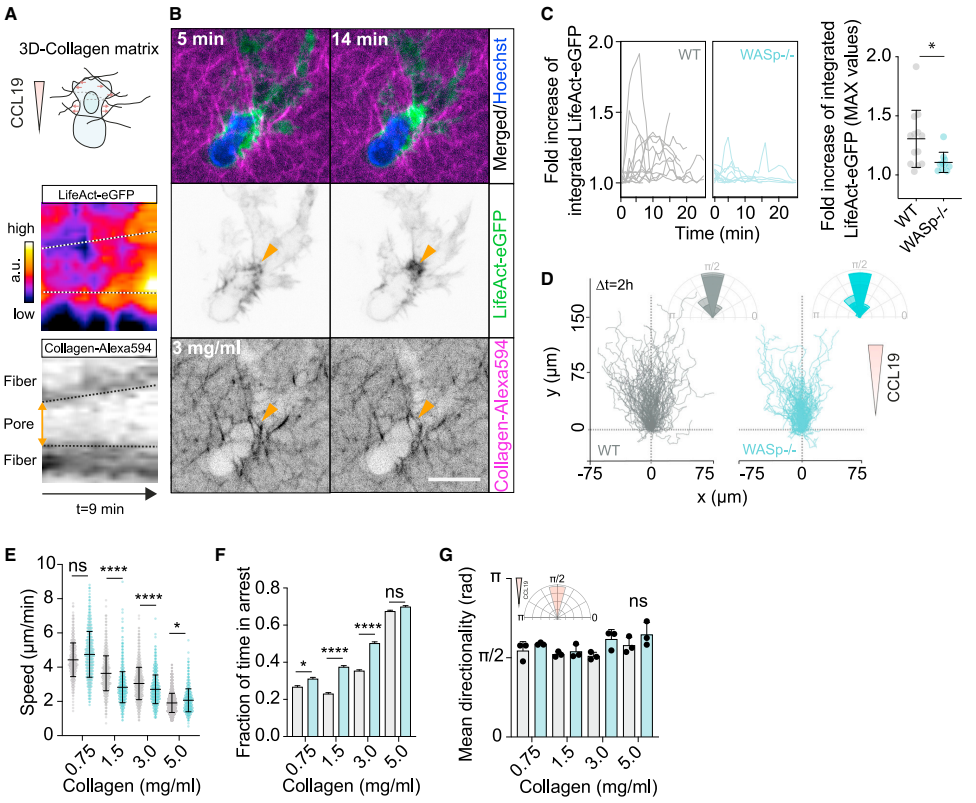

Figure 5. Deformation of collagen bers is required for migration in brous environments

(A) Schematic of experimental setup.

(B) Time-lapse spinning disk confocal microscopy reveals local deformation of obstructive collagen bers (Alexa-594 labeled; 3.0 mg/mL) and increase of pore sizes for passage of the cell body (lower panel). Arrow heads indicate pore. Kymograph (left) shows dilation of the pore. Notably, ber deformation was accompanied by local actin polymerization (middle panel). Upper panel shows merged images of LifeAct-eGFP and Collagen-Alexa-594. Scale bar, 10 μm.

(C) Left: time traces of LifeAct-eGFP signal at sites of obstructive bers (normalized to intensity of the rst frame; fold change of intensity is shown). Right: each data point shows the local maximum of LifeAct-eGFP signal from one trace (fold change of intensity; rst frame as reference). WT: n = 12 cells; WASp$^{-/-}$: n = 10 cells; mean ± SD; Mann-Whitney test; *p = 0.0358.

(D G) Bulk analysis of DCs migrating in brous 3D collagen matrices with increasing densities (gray = WT; turquoise = WASp$^{-/-}$). (D) Trajectory plot and directionality plot (inset) of DCs migrating in 1.5 mg/mL collagen gels.

(E) Shows mean speed of tracks pooled from 3 experiments. WT (0.75: n = 694; 1.5: n = 1,181; 3.0: n = 1,551; 5.0: n = 981); WASp$^{-/-}$ (0.75: n = 599; 1.5: n = 1,130; 3.0: n = 1,086; 5.0: n = 853). Mean ± SD; Kruskal-Wallis-test/Dunn s multiple comparisons test; *p = 0.0221; ****p < 0.0001.

(F) Fraction of time in arrest was extracted from tracks in (E). Mean ± SD; Kruskal-Wallis-test/Dunn s multiple comparisons test; mean ± SEM; *p = 0.047; ****p < 0.0001.

(G) Mean directionality of DCs along CCL19 gradients. n = 3 experiments; mean + SEM; Watson s Large-sample non-parametric test; ns, not signi cant. Also see Figure S5 and Video S5.

relevance (Bouma et al., 2007; de Noronha et al., 2005; Pulecio et al., 2008; Snapper et al., 2005).

We next employed brillar collagen, the most abundant matrix scaffold of mammalian tissues, as a proxy for the interstitial matrix. Collagen gels were polymerized at densities resulting in pore sizes substantially smaller than the minimal cross-section of deformed DCs (Lang et al., 2015; Renkawitz et al., 2019; Thiam et al., 2016; Wolf et al., 2013). Chemotactic locomotion under these conditions should depend on the deformation of obstructive bers (Figure 5A). Indeed, fast confocal imaging revealed that DCs locally displaced collagen bers, thereby generating space for the passage of the cell body. Locally, the deformation

of collagen bers was accompanied by a burst in actin polymerization (Figures 5B and 5C; Video S5). We then performed bulk measurements of large numbers of DCs migrating along CCL19 gradients (Figure 5D). In low-density collagen gels, where pore sizes between bers are suf ciently large to allow unconstrained locomotion, WASp$^{-/-}$ cells were not signi cantly slower than WT controls (Figure 5E). With increasing collagen gel densities (decreased pore size and increased stiffness), DCs were more reliant on displacing bers to generate space (Figure S5B), became substantially slower (Figure 5E), and often arrested (Figure 5F), indicating that matrix deformation became a rate-limiting parameter. Accordingly, under these conditions, WASp-de - cient DCs were less ef cient in recruiting actin to restrictive bers (Figures 5C and S5C). Of note, similar to migration under agarose, directionality toward CCL19 was not affected by WASp deletion, indicating a negligible role of WASp-dependent actin patches in chemotaxis (Figures 5D and 5G). Together, our data show that cells require WASp-dependent pushing to mechanically create space in dense 3D matrices and provide a mechanistic explanation for impaired migration of WASp$^{-/-}$ DCs *in vivo* (Figure S5A).

Orthogonal actin patches drive T cell migration in crowded LN

WASp de ciency affects multiple hematopoietic lineages however, the dominant phenotype of WAS patients is a congenital immunode ciency due to defective T cell functions (Ochs, 2001). Cell migration is inevitably linked to activation of naive T cells, as T cells need to constantly scan cell-packed secondary lymphoid tissues to search for cognate antigen on antigen presenting cells (Krummel et al., 2016). While WASp plays an established role in T cell development and immune synapse formation its role in interstitial T cell migration remained unclear (Thrasher and Burns, 2010). To test if the mechanism we established for DCs is relevant for lymphocytes, we puri ed naive T cells from WASp$^{-/-}$ mice and con ned them under intermediate-stiff agarose. In the presence of homogeneous CCL19, naive T cells become polarized and migrate randomly without the formation of substrate adhesions (Hons et al., 2018). Locomotion of WASp$^{-/-}$ T cells was signi - cantly impaired compared with WT controls, and cells were frequently arrested under the load of the compressive overlay (Figure 6A; Video S6). Similar to con ned DCs, WT T cells formed highly dynamic actin patches traveling backward with the retrograde actin ow (Figure 6B) and pushing vertically against the substrate (Figure S6A). These actin patches were virtually absent in WASp$^{-/-}$ cells (Figure 6B; Video S6). Subcellular mechanical loading with both micropipette tips (Figure S6B; Video S6) and nanometer-sized ridges (Figures 6C and S6C; Video S6) triggered the formation of WASp-dependent actin patches. Finally, cortical stiffness measured by submicron indentation with the tip of an AFM cantilever was signi cantly reduced in WASp$^{-/-}$ compared with WT cells (Figures 6D and S6D). Together, these data support a crucial role of WASp-dependent actin patches in the cortical mechanics of T cells. Next, we adoptively transferred labeled WT and WASp$^{-/-}$ naive T cells into WT recipient mice (Figure 6E). Since WASp$^{-/-}$ T cells show unimpaired homing to popliteal LN (Snapper et al., 2005), these experimental conditions allowed us to compare intranodal migration of both genotypes side by side (Figure 6E; Video S6). WASp$^{-/-}$ T cells were able to reach maximum speeds comparable to WT controls, indicating that WASp was not strictly required for locomotion of T cells *in vivo* (Figure S6D). However, a signi cantly larger fraction of cells showed periods of minimal displacement (<2.5 μm in 1 min) (Figure 6F), resulting in an overall reduced mean speed (Figures 6G and S6E). These data con rm that WASp-dependent actin patches are of general relevance for 3D migration under compressive loads across both myeloid and lymphoid hematopoietic lineages and provide a mechanistic framework for defective cell migration observed in X-linked WAS (Bouma et al., 2009).

DISCUSSION

First described in 1937, WAS is one of the most thoroughly investigated severe congenital immunode ciencies (Ochs, 2001). WAS patients suffer from thrombocytopenia, eczema, and recurrent bacterial infections. Although underlying defects in cell-cell interactions and motility of the hematopoietic compartment have been attributed to the well-established function of WASp as one of the upstream activators of Arp2/3 nucleated actin polymerization, the precise cell biology behind WAS remained obscure (Fritz-Laylin et al., 2017a; Graziano and Weiner, 2014; Machesky and Insall, 1998; Thrasher and Burns, 2010). We here show that WASp drives cortical actin polymerization in the third dimension and that it does so in a mechanosensitive manner. WASp-dependent forces act orthogonal to the direction of cellular locomotion, and they are dispensable when the cell migrates in environments where the pore size is suf ciently large for the cell body to passage. WASp becomes rate limiting for migration when the cell needs to pass through restrictive environments that require the cell to deform its viscoelastic surrounding. WASp assembles into dot-like structures that are embedded into the actin cortex and act as nucleation sites for actin patches that then protrude against the external obstacle.

This function of WASp contrasts with that of the Arp2/3-activating WAVE complex. The WAVE complex does not assemble in discrete spots but in traveling waves: as WAVE activity is self-amplifying and at the same time negatively regulated by polymerized actin, it creates an excitable system that travels as a linear front (Graziano and Weiner, 2014). The resulting in-plane of the membrane polymerization pattern only allows protrusion at the tip of a strictly at lamellipodium, where the sheet of plasma membrane curves to form an envelope. Accordingly, the orientation of Arp2/3 branches in lamellipodia is exclusively horizontal (Svitkina, 2018). WASp lacks the self-organizing feature of the WAVE complex. It stays con ned in dot-like assemblies, and its lateral movement seems restricted to passive co-migration within the surrounding cortex. This lack of self-organization might allow WASp activity to remain on target when the cell pushes against a structure as delicate and small as a collagen ber. When cells migrated on the nanotopographies, the precision with which the WASp dots located to the ridges was remarkable and suggested that WASp assembles in response to a highly localized signal. Importantly, this putative signal is independent of adhesive interactions, which is well in line with the ameboid principle that can work in the absence of any cognate adhesive interaction with a substrate. Topographical changes of the plasma membrane as sensed e.g., by BAR

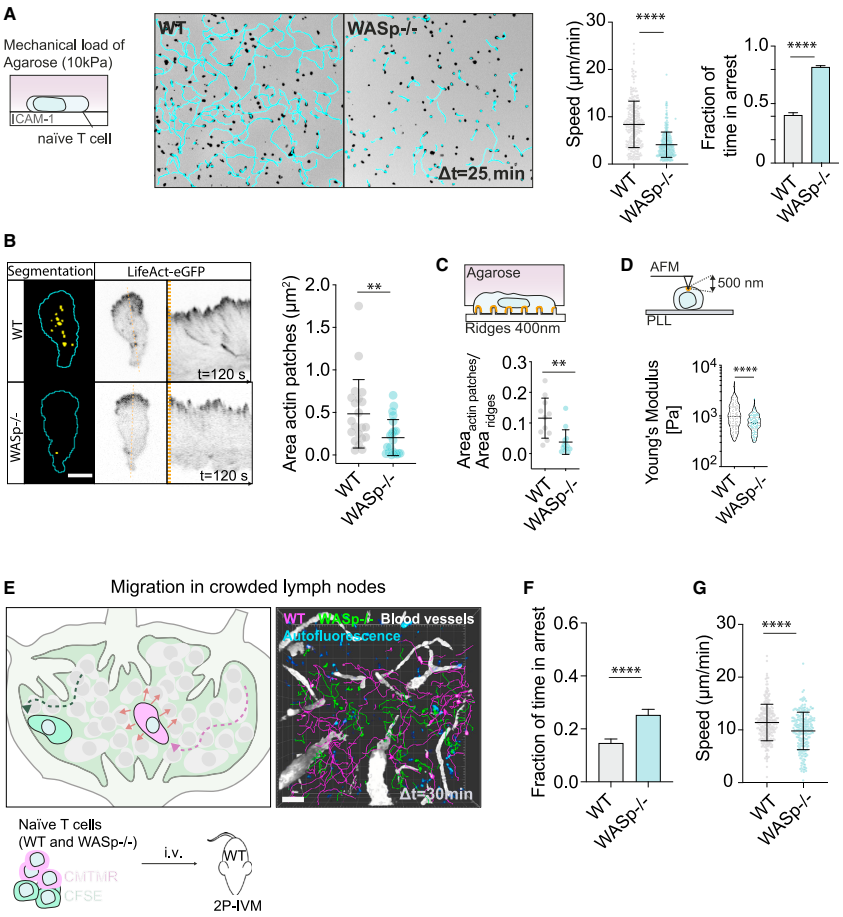

Figure 6. Orthogonal actin patches drive T cell migration in crowded lymph nodes

(A) Schematic of experimental setup. Epi uorescence images (CMTMR) from representative time series: single-cell tracks are overlaid in light-blue; scale bar, 100 μm. Mean track speed was quanti ed. Each data point represents one track. WT: n = 290, WASp$^{-/-}$: n = 335 pooled from 4 experiments; mean ± SD; Mann-Whitney test; ****p < 0.0001. Fraction of time in arrest was extracted from tracks; mean + SEM; Mann-Whitney test; ****p < 0.0001.

(B) Actin patches were segmented from LifeAct-eGFP movies (spinning disk confocal microscopy) in Ilastik and area was quanti ed. Actin patches traveled backward with the retrograde actin ow (kymographs); WT: n = 21 cells, WASp$^{-/-}$: n = 22 cells; mean ± SD; Mann-Whitney test; **p = 0.0030; scale bar, 5 μm.

(C) Fraction of ridges covered by actin patches (segmented in Ilastik) (also see Figures S4B and S6B). WT: n = 11; WASp$^{-/-}$: n = 13; Mean ± SD; Mann-Whitney test; **p = 0.0015.

(D) Schematic of an AFM experiment. Using a Hertz contact mechanics model, the elastic modulus was estimated by tting the force indentation curves up to 500 nm. Each data point represents one measurement. WT: n = 182 from 16 cells; WASp$^{-/-}$: n = 165 from 15 cells. For cellwise analysis see Figure S6C. Violin plot with median ± quartiles; Mann-Whitney test; ****p < 0.0001.

(E) Adoptive transfer of uorescently labeled T cells (WT and WASp$^{-/-}$) into wild-type recipient mice. After 24 h, T cell migration in LN parenchyma was analyzed using intravital two-photon microscopy. Representative 3D reconstruction of adoptively transferred T cells migrating in LN parenchyma (2-photon intravital microscopy). Scale bar, 50 μm.

(F) Fraction of time in arrest was extracted from tracks (see H); mean + SEM; Mann-Whitney test; ****p < 0.0001.

(H) Mean track speed. Each data point represents one track. WT: n = 262, WASp$^{-/-}$: n = 237 pooled from 5 experiments; mean ± SD; Mann-Whitney test; ****p < 0.0001. Also see Figure S6 and Video S6.

domain-containing proteins are the most attractive candidates for such an alternative sensory function (Lou et al., 2019; Suetsugu and Gautreau, 2012; Brunetti et al., 2021). Supporting this hypothesis, we show that the F-BAR domain protein Cip4 accumulates at sites of membrane indentation where it precedes the formation of actin patches.

How cells adapt to compressive load in 3D tissue environments is still incompletely understood. Recent studies proposed an evasion re ex in response to cellular compression: upon deformation of the nucleus cells increase their cortical contractility to move away and squeeze out of tight spaces or crowded tissue regions (Lomakin et al., 2020; Venturini et al., 2020). However, to reach their target sites, leukocytes often need to traverse tissues of high density. Mechanosensitive actin patches pushing against obstructing barriers facilitate this and might as such represent a very primordial invasive program. Indeed, until to date, one of the best-established functions of WASp and its non-hematopoietic isoform N-WASp are invasive podosomes and invadosomes (Murphy and Courtneidge, 2011). Podosomes are adhesive organelles, composed of a protrusive actin core, which is surrounded by an obligate adhesive ring-structure, presumably to counter the pushing force of the core (van den Dries et al., 2019). While matrix-degrading activity, due to targeted delivery of proteases is a further de ning feature of podosomes (Linder, 2007), some non-proteolytic podosome-like organelles have been described, but these structures were strictly coupled to cell-cell adhesions (Carman et al., 2007; Kumari et al., 2015; Poulter et al., 2015; Sens et al., 2010). Consequently, the WASp patches we describe may represent the most rudimentary podosome-like structure, reduced only to the protrusive actin core. It seems plausible that in very-fast-migrating and low-adhesive leukocytes WASp-driven actin patches are not locked in place by an adhesive ring and thus lack the maturation signal that would turn them into degradative podosomes. Notably, work in invasive *C. elegans* anchor cells showed that in WASp-dependent sites of basement membrane invasion, protrusive forces and proteolytic degradation synergize to drive barrier-penetration (Caceres et al., 2018). Upon inhibition of proteolysis, invasion can partially proceed in an entirely mechanically driven fashion (Kelley et al., 2019).

The protrusive actin patches we describe also share some features with early stages of clathrin-mediated endocytosis, where the positive curvature of the plasma membrane is associated with WASp-driven actin polymerization (Almeida-Souza et al., 2018). Actin polymerization on clathrin coated pits (CCP) is oriented normal to the cell surface, allowing it to push the CCP inward (Collins et al., 2011; Picco et al., 2015; Akamatsu et al., 2020). This orientation is consistent with our ndings that WASp plays a unique role in driving cortical actin polymerization in the third dimension.

Taken together, our data support the general notion that, in contrast to inside-out activated lamellipodia that protrude in the direction of migration, outside-in activated actin patches push orthogonally to the plasma membrane, thereby rendering cells mechanoactive in 3D.

Limitations of the study

While our study shows that positive membrane curvature recruits WASp-dependent actin patches to the plasma membrane, the underlying mechanisms acting upstream of WASp remain unclear. Curvature-sensing proteins, such as F-BAR domain proteins, are promising candidates, but future work still needs to decipher their functional role in this process.

STAR★METHODS

Detailed methods are provided in the online version of this paper and include the following:

- KEY RESOURCES TABLE
- RESOURCE AVAILABILITY
  - Lead contact
  - Materials availability
  - Data and code availability
- EXPERIMENTAL MODEL AND SUBJECT DETAILS
  - Mouse strains
  - Primary cells
- METHOD DETAILS
  - Differentiation and culture of mature dendritic cells
  - Puri cation and culture of na ve T-cells
  - Plasmids and lentivirus production
  - Transfection
  - Enucleation of matured dendric cells
  - Pharmacological inhibitors
  - Antibodies
  - Under-agarose migration assay of na ve T-cells
  - Under-agarose migration assay of mature dendritic cells on adhesive substrate (invasion under agarose)
  - Under-agarose migration assay of mature dendritic cells on slippery substrate (injection under agarose)
  - Migration in microfabricated pillar forests and straight and constricted channels
  - Collagen migration assay
  - Migration on nano-ridges
  - Micropipette indentation assay
  - Electron microscopy
  - Atomic force microscopy
  - Dendritic cell lymph node homing assay
  - Intravital two-photon microscopy of popliteal lymph nodes
  - Image analysis
  - 3D analysis of T-cell migration in LNs
  - 2D analysis of migration assays (under agarose; pillar forests; collagen assays)
  - Analysis of directionality
  - Fraction of time in arrest
  - Segmentation of actin patches
  - Shape analysis
  - Cross-correlation analysis and bootstrapping statistics
  - Particle Image Velocimetry of collagen matrices
- QUANTIFICATION AND STATISTICAL ANALYSIS

SUPPLEMENTAL INFORMATION

Supplemental information can be found online at https://doi.org/10.1016/j.devcel.2021.11.024.

ACKNOWLEDGMENTS

We thank N. Darwish-Miranda, F. Leite, F.P. Assen, and A. Eichner for advice and help with experiments. We thank J. Renkawitz, E. Kiermaier, A. Juanes Garcia, and M. Avellaneda for critical reading of the manuscript. We thank M. Driscoll for advice on uorescent labeling of collagen gels. This research was supported by the Scienti c Service Units (SSUs) of IST Austria through resources provided by Molecular Biology Services/Lab Support Facility (LSF)/Bioimaging Facility/Electron Microscopy Facility. This work was funded by grants from the European Research Council (CoG 724373) and the Austrian Science Foundation (FWF) to M.S. F.G. received funding from the European Union s Horizon 2020 research and innovation program under the Marie Skłodowska-Curie grant agreement no. 747687.

AUTHOR CONTRIBUTIONS

Conceptualization, F.G. and M.S.; methodology, F.G., P.R.-R., I.V., M.H., J.A., J.M., V.Z., and W.A.K.; investigation, F.G., P.R.-R., I.V., A.K., and M.H.; software, R.H. and S.T.; resources, A.L., formal analysis, F.G., R.H., P.R.-R., and M.R.; writing original draft, F.G. and M.S.; writing editing, all authors; visualization, F.G.; supervision, F.G. and M.S.; project administration, F.G.; funding acquisition, F.G. and M.S.

DECLARATION OF INTERESTS

The authors declare no competing interests.

Received: January 8, 2021
Revised: September 6, 2021
Accepted: November 24, 2021
Published: December 16, 2022

REFERENCES

Akamatsu, M., Vasan, R., Serwas, D., Ferrin, M.A., Rangamani, P., and Drubin, D.G. (2020). Principles of self-organization and load adaptation by the actin cytoskeleton during clathrin-mediated endocytosis. eLife *9*, e49840. https://doi.org/10.7554/eLife.4984.

Almeida-Souza, L., Frank, R.A.W., Garc a-Nafr a, J., Colussi, A., Gunawardana, N., Johnson, C.M., Yu, M., Howard, G., Andrews, B., Vallis, Y., and McMahon, H.T. (2018). A at BAR protein promotes actin polymerization at the base of Clathrin-coated pits. Cell *174*, 325 337. e314. https://doi.org/10.1016/j.cell.2018.05.020.

Barr, V.A., and Bunnell, S.C. (2009). Interference re ection microscopy. Curr Protoc Cell Biol *45*, 4.23.1 4.23.19. https://doi.org/10.1002/0471143030.cb0423s45.

Barry, N.P., and Bretscher, M.S. (2010). Dictyostelium amoebae and neutrophils can swim. Proc. Natl. Acad. Sci. USA *107*, 11376 11380. https://doi.org/10.1073/pnas.1006327107.

Benesch, S., Lommel, S., Steffen, A., Stradal, T.E., Scaplehorn, N., Way, M., Wehland, J., and Rottner, K. (2002). Phosphatidylinositol 4,5-biphosphate (PIP2)-induced vesicle movement depends on N-WASP and involves Nck, WIP, and Grb2. J. Biol. Chem. *277*, 37771 37776. https://doi.org/10.1074/jbc.M204145200.

Berg, S., Kutra, D., Kroeger, T., Straehle, C.N., Kausler, B.X., Haubold, C., Schiegg, M., Ales, J., Beier, T., Rudy, M., et al. (2019). ilastik: interactive machine learning for (bio)image analysis. Nat. Methods *16*, 1226 1232. https://doi.org/10.1038/s41592-019-0582-9.

Blumenthal, D., Chandra, V., Avery, L., and Burkhardt, J.K. (2020). Mouse T cell priming is enhanced by maturation-dependent stiffening of the dendritic cell cortex. Elife *9*, e55995. https://doi.org/10.7554/eLife.55995.

Bouma, G., Burns, S., and Thrasher, A.J. (2007). Impaired T-cell priming in vivo resulting from dysfunction of WASp-de cient dendritic cells. Blood *110*, 4278 4284. https://doi.org/10.1182/blood-2007-06-096875.

Bouma, G., Burns, S.O., and Thrasher, A.J. (2009). Wiskott-Aldrich syndrome: immunode ciency resulting from defective cell migration and impaired immunostimulatory activation. Immunobiology *214*, 778 790. https://doi.org/10.1016/j.imbio.2009.06.009.

Bovellan, M., Romeo, Y., Biro, M., Boden, A., Chugh, P., Yonis, A., Vaghela, M., Fritzsche, M., Moulding, D., Thorogate, R., et al. (2014). Cellular control of cortical actin nucleation. Curr. Biol. *24*, 1628 1635. https://doi.org/10.1016/j.cub.2014.05.069.

Brunetti, R.M., Kockelkoren, G., Raghavan, P., Bell, G.R.R., Britain, D., Puri, N., Collins, S.R., Leonetti, M.D., Stamou, D., and Weiner, O.D. (2021). WASP links substrate topology and cell polarity to guide neutrophil migration. bioRxiv. https://doi.org/10.1101/2021.05.12.443722.

Caceres, R., Bojanala, N., Kelley, L.C., Dreier, J., Manzi, J., Di Federico, F., Chi, Q., Risler, T., Testa, I., Sherwood, D.R., and Plastino, J. (2018). Forces drive basement membrane invasion in Caenorhabditis elegans. Proc. Natl. Acad. Sci. USA *115*, 11537 11542. https://doi.org/10.1073/pnas.1808760115.

Carman, C.V., Sage, P.T., Sciuto, T.E., de la Fuente, M.A., Geha, R.S., Ochs, H.D., Dvorak, H.F., Dvorak, A.M., and Springer, T.A. (2007). Transcellular diapedesis is initiated by invasive podosomes. Immunity *26*, 784 797. https://doi.org/10.1016/j.immuni.2007.04.015.

Collins, A., Warrington, A., Taylor, K.A., and Svitkina, T. (2011). Structural organization of the actin cytoskeleton at sites of clathrin-mediated endocytosis. Curr. Biol. *21*, 1167 1175. https://doi.org/10.1016/j.cub.2011.05.048.

Croft, D.R., Coleman, M.L., Li, S., Robertson, D., Sullivan, T., Stewart, C.L., and Olson, M.F. (2005). Actin-myosin-based contraction is responsible for apoptotic nuclear disintegration. J. Cell Biol. *168*, 245 255. https://doi.org/10.1083/jcb.200409049.

de Noronha, S., Hardy, S., Sinclair, J., Blundell, M.P., Strid, J., Schulz, O., Zwirner, J., Jones, G.E., Katz, D.R., Kinnon, C., and Thrasher, A.J. (2005). Impaired dendritic-cell homing in vivo in the absence of Wiskott-Aldrich syndrome protein. Blood *105*, 1590 1597. https://doi.org/10.1182/blood-2004-06-2332.

Ferguson, J.P., Huber, S.D., Willy, N.M., Aygün, E., Goker, S., Atabey, T., and Kural, C. (2017). Mechanoregulation of clathrin-mediated endocytosis. J. Cell Sci. *130*, 3631 3636. https://doi.org/10.1242/jcs.205930.

Friedl, P., and Wolf, K. (2010). Plasticity of cell migration: a multiscale tuning model. J. Cell Biol. *188*, 11 19. https://doi.org/10.1083/jcb.200909003.

Fritz-Laylin, L.K., Lord, S.J., Kakley, M., and Mullins, R.D. (2018). Concise language promotes clear thinking about cell shape and locomotion. BioEssays *40*, e1700225. https://doi.org/10.1002/bies.201700225.

Fritz-Laylin, L.K., Lord, S.J., and Mullins, R.D. (2017a). WASP and SCAR are evolutionarily conserved in actin- lled pseudopod-based motility. J. Cell Biol. *216*, 1673 1688. https://doi.org/10.1083/jcb.201701074.

Fritz-Laylin, L.K., Riel-Mehan, M., Chen, B.C., Lord, S.J., Goddard, T.D., Ferrin, T.E., Nicholson-Dykstra, S.M., Higgs, H., Johnson, G.T., Betzig, E., and Mullins, R.D. (2017b). Actin-based protrusions of migrating neutrophils are intrinsically lamellar and facilitate direction changes. Elife *6*, e26990. https://doi.org/10.7554/eLife.26990.

Gerard, A., Patino-Lopez, G., Beemiller, P., Nambiar, R., Ben-Aissa, K., Liu, Y., Totah, F.J., Tyska, M.J., Shaw, S., and Krummel, M.F. (2014). Detection of rare antigen-presenting cells through T cell-intrinsic meandering motility, mediated by Myo1g. Cell *158*, 492 505. https://doi.org/10.1016/j.cell.2014.05.044.

Graham, D.M., Andersen, T., Sharek, L., Uzer, G., Rothenberg, K., Hoffman, B.D., Rubin, J., Balland, M., Bear, J.E., and Burridge, K. (2018). Enucleated cells reveal differential roles of the nucleus in cell migration, polarity, and mechanotransduction. J. Cell Biol. *217*, 895 914. https://doi.org/10.1083/jcb.201706097.

Graziano, B.R., and Weiner, O.D. (2014). Self-organization of protrusions and polarity during eukaryotic chemotaxis. Curr. Opin. Cell Biol. *30*, 60 67. https://doi.org/10.1016/j.ceb.2014.06.007.

Guimaraes, C.F., Gasperini, L., Marques, A.P., and Reis, R.L. (2020). The stiffness of living tissues and its implications for tissue engineering. Nat. Rev. Mater. *5*, 351 370. https://doi.org/10.1038/s41578-019-0169-1.

Heinemann, F., Doschke, H., and Radmacher, M. (2011). Keratocyte lamellipodial protrusion is characterized by a concave force-velocity relation. Biophys. J. *100*, 1420 1427. https://doi.org/10.1016/j.bpj.2011.01.063.

Hons, M., Kopf, A., Hauschild, R., Leithner, A., Gaertner, F., Abe, J., Renkawitz, J., Stein, J.V., and Sixt, M. (2018). Chemokines and integrins independently tune actin ow and substrate friction during intranodal migration of T cells. Nat. Immunol. *19*, 606 616. https://doi.org/10.1038/s41590-018-0109-z.

Hu, J., Chen, S., Hu, W., Lü, S., and Long, M. (2019). Mechanical point loading induces cortex stiffening and actin reorganization. Biophys. J. *117*, 1405 1418. https://doi.org/10.1016/j.bpj.2019.09.012.

Kelley, L.C., Chi, Q., Caceres, R., Hastie, E., Schindler, A.J., Jiang, Y., Matus, D.Q., Plastino, J., and Sherwood, D.R. (2019). Adaptive F-actin polymerization and localized ATP production drive basement membrane invasion in the absence of MMPs. Dev. Cell *48*, 313 328. e318. https://doi.org/10.1016/j.devcel.2018.12.018.

Koduru, S., Kumar, L., Massaad, M.J., Ramesh, N., Le Bras, S., Ozcan, E., Oyoshi, M.K., Kaku, M., Fujiwara, Y., Kremer, L., et al. (2010). Cdc42 interacting protein 4 (CIP4) is essential for integrin-dependent T-cell traf cking. Proc. Natl. Acad. Sci. USA *107*, 16252 16256. https://doi.org/10.1073/pnas.1002747107.

Krause, M., and Gautreau, A. (2014). Steering cell migration: lamellipodium dynamics and the regulation of directional persistence. Nat. Rev. Mol. Cell Biol. *15*, 577 590. https://doi.org/10.1038/nrm3861.

Kremer, J.R., Mastronarde, D.N., and McIntosh, J.R. (1996). Computer visualization of three-dimensional image data using IMOD. J. Struct. Biol. *116*, 71 76. https://doi.org/10.1006/jsbi.1996.0013.

Krummel, M.F., Bartumeus, F., and Gerard, A. (2016). T cell migration, search strategies and mechanisms. Nat. Rev. Immunol. *16*, 193 201. https://doi.org/10.1038/nri.2015.16.

Kumari, S., Depoil, D., Martinelli, R., Judokusumo, E., Carmona, G., Gertler, F.B., Kam, L.C., Carman, C.V., Burkhardt, J.K., Irvine, D.J., and Dustin, M.L. (2015). Actin foci facilitate activation of the phospholipase C-gamma in primary T lymphocytes via the WASP pathway. Elife *4*, e04953. https://doi.org/10.7554/eLife.04953.

Laevsky, G., and Knecht, D.A. (2003). Cross-linking of actin laments by myosin II is a major contributor to cortical integrity and cell motility in restrictive environments. J. Cell Sci. *116*, 3761 3770. https://doi.org/10.1242/jcs.00684.

Lai, F.P., Szczodrak, M., Block, J., Faix, J., Breitsprecher, D., Mannherz, H.G., Stradal, T.E., Dunn, G.A., Small, J.V., and Rottner, K. (2008). Arp2/3 complex interactions and actin network turnover in lamellipodia. EMBO J. *27*, 982 992. https://doi.org/10.1038/emboj.2008.34.

Lämmermann, T., Bader, B.L., Monkley, S.J., Worbs, T., Wedlich-Soldner, R., Hirsch, K., Keller, M., Forster, R., Critchley, D.R., Fässler, R., and Sixt, M. (2008). Rapid leukocyte migration by integrin-independent owing and squeezing. Nature *453*, 51 55. https://doi.org/10.1038/nature06887.

Lang, N.R., Skodzek, K., Hurst, S., Mainka, A., Steinwachs, J., Schneider, J., Aifantis, K.E., and Fabry, B. (2015). Biphasic response of cell invasion to matrix stiffness in three-dimensional biopolymer networks. Acta Biomater *13*, 61 67. https://doi.org/10.1016/j.actbio.2014.11.003.

Laplaud, V., Levernier, N., Pineau, J., Roman, M.S., Barbier, L., Saez, P.J., Lennon-Dumenil, A.-M., Vargas, P., Kruse, K., du Roure, O., et al. (2021). Pinching the cortex of live cells reveals thickness instabilities caused by myosin II motors. Sci. Adv. *7*, eabe3640. https://doi.org/10.1126/sciadv.abe3640.

Leithner, A., Eichner, A., Müller, J., Reversat, A., Brown, M., Schwarz, J., Merrin, J., de Gorter, D.J., Schur, F., Bayerl, J., et al. (2016). Diversi ed actin protrusions promote environmental exploration but are dispensable for locomotion of leukocytes. Nat. Cell Biol. *18*, 1253 1259. https://doi.org/10.1038/ncb3426.

Leithner, A., Renkawitz, J., De Vries, I., Hauschild, R., Häcker, H., and Sixt, M. (2018). Fast and ef cient genetic engineering of hematopoietic precursor cells for the study of dendritic cell migration. Eur. J. Immunol. *48*, 1074 1077. https://doi.org/10.1002/eji.201747358.

Linder, S. (2007). The matrix corroded: podosomes and invadopodia in extracellular matrix degradation. Trends Cell Biol. *17*, 107 117. https://doi.org/10.1016/j.tcb.2007.01.002.

Lomakin, A.J., Cattin, C.J., Cuvelier, D., Alraies, Z., Molina, M., Nader, G.P.F., Srivastava, N., Saez, P.J., Garcia-Arcos, J.M., Zhitnyak, I.Y., et al. (2020). The nucleus acts as a ruler tailoring cell responses to spatial constraints. Science *370*, eaba2894. https://doi.org/10.1126/science.aba2894.

Lou, H.Y., Zhao, W., Li, X., Duan, L., Powers, A., Akamatsu, M., Santoro, F., McGuire, A.F., Cui, Y., Drubin, D.G., and Cui, B. (2019). Membrane curvature underlies actin reorganization in response to nanoscale surface topography. Proc. Natl. Acad. Sci. USA *116*, 23143 23151. https://doi.org/10.1073/pnas.1910166116.

Machesky, L.M., and Insall, R.H. (1998). Scar1 and the related Wiskott Aldrich syndrome protein, WASP, regulate the actin cytoskeleton through the Arp2/3 complex. Curr. Biol. *8*, 1347 1356. https://doi.org/10.1016/s0960-9822(98)00015-3.

Maiuri, P., Rupprecht, J.F., Wieser, S., Ruprecht, V., Benichou, O., Carpi, N., Coppey, M., De Beco, S., Gov, N., Heisenberg, C.-P., et al. (2015). Actin ows mediate a universal coupling between cell speed and cell persistence. Cell *161*, 374 386. https://doi.org/10.1016/j.cell.2015.01.056.

Mastronarde, D.N. (2003). SerialEM: a program for automated tilt series acquisition on Tecnai microscopes using prediction of specimen position. Microsc. Microanal. *9*, 1182 1183. https://doi.org/10.1017/s1431927603445911.

Mogilner, A. (2006). On the edge: modeling protrusion. Curr. Opin. Cell Biol. *18*, 32 39. https://doi.org/10.1016/j.ceb.2005.11.001.

Mueller, J., Szep, G., Nemethova, M., de Vries, I., Lieber, A.D., Winkler, C., Kruse, K., Small, J.V., Schmeiser, C., Keren, K., et al. (2017). Load adaptation of lamellipodial actin networks. Cell *171*, 188 200. e116. https://doi.org/10.1016/j.cell.2017.07.051.

Murphy, D.A., and Courtneidge, S.A. (2011). The ins and outs of podosomes and invadopodia: characteristics, formation and function. Nat. Rev. Mol. Cell Biol. *12*, 413 426. https://doi.org/10.1038/nrm3141.

Ochs, H.D. (2001). The Wiskott-Aldrich syndrome. Clin. Rev. Allergy Immunol. *20*, 61 86. https://doi.org/10.1385/CRIAI:20:1:61.

Paluch, E.K., Aspalter, I.M., and Sixt, M. (2016). Focal adhesion-independent cell migration. Annu. Rev. Cell Dev. Biol. *32*, 469 490. https://doi.org/10.1146/annurev-cellbio-111315-125341.

Pewsey, A., Neuhauser, M., and Ruxton, G.D. (2013). Circular Statistics in R (Oxford University Press).

P icke, H., and Sixt, M. (2009). Preformed portals facilitate dendritic cell entry into afferent lymphatic vessels. J. Exp. Med. *206*, 2925 2935. https://doi.org/10.1084/jem.20091739.

Picco, A., Mund, M., Ries, J., Nedelec, F., and Kaksonen, M. (2015). Visualizing the functional architecture of the endocytic machinery. Elife *4*, e04535. https://doi.org/10.7554/eLife.04535.

Pincus, Z., and Theriot, J.A. (2007). Comparison of quantitative methods for cell-shape analysis. J. Microsc. *227*, 140 156. https://doi.org/10.1111/j.1365-2818.2007.01799.x.

Plotnikov, S.V., and Waterman, C.M. (2013). Guiding cell migration by tugging. Curr. Opin. Cell Biol. *25*, 619 626. https://doi.org/10.1016/j.ceb.2013.06.003.

Poulter, N.S., Pollitt, A.Y., Davies, A., Malinova, D., Nash, G.B., Hannon, M.J., Pikramenou, Z., Rappoport, J.Z., Hartwig, J.H., Owen, D.M., et al. (2015). Platelet actin nodules are podosome-like structures dependent on Wiskott-Aldrich syndrome protein and Arp2/3 complex. Nat. Commun. *6*, 7254. https://doi.org/10.1038/ncomms8254.

Pulecio, J., Tagliani, E., Scholer, A., Prete, F., Fetler, L., Burrone, O.R., and Benvenuti, F. (2008). Expression of Wiskott-Aldrich syndrome protein in dendritic cells regulates synapse formation and activation of naive CD8+ T cells. J. Immunol. *181*, 1135 1142. https://doi.org/10.4049/jimmunol.181.2.1135.

Redecke, V., Wu, R., Zhou, J., Finkelstein, D., Chaturvedi, V., High, A.A., and Häcker, H. (2013). Hematopoietic progenitor cell lines with myeloid and lymphoid potential. Nat. Methods *10*, 795 803. https://doi.org/10.1038/nmeth.2510.

Renkawitz, J., Kopf, A., Stopp, J., de Vries, I., Driscoll, M.K., Merrin, J., Hauschild, R., Welf, E.S., Danuser, G., Fiolka, R., and Sixt, M. (2019). Nuclear positioning facilitates amoeboid migration along the path of least

resistance. Nature *568*, 546 550. https://doi.org/10.1038/s41586-019-1087-5.

Renkawitz, J., Schumann, K., Weber, M., Lämmermann, T., P icke, H., Piel, M., Polleux, J., Spatz, J.P., and Sixt, M. (2009). Adaptive force transmission in amoeboid cell migration. Nat. Cell Biol. *11*, 1438 1443. https://doi.org/10.1038/ncb1992.

Revach, O.Y., Weiner, A., Rechav, K., Sabanay, I., Livne, A., and Geiger, B. (2015). Mechanical interplay between invadopodia and the nucleus in cultured cancer cells. Sci. Rep. *5*, 9466. https://doi.org/10.1038/srep09466.

Reversat, A., Gaertner, F., Merrin, J., Stopp, J., Tasciyan, S., Aguilera, J., de Vries, I., Hauschild, R., Hons, M., Piel, M., et al. (2020). Cellular locomotion using environmental topography. Nature *582*, 582 585. https://doi.org/10.1038/s41586-020-2283-z.

Riedl, J., Crevenna, A.H., Kessenbrock, K., Yu, J.H., Neukirchen, D., Bista, M., Bradke, F., Jenne, D., Holak, T.A., Werb, Z., et al. (2008). Lifeact: a versatile marker to visualize F-actin. Nat. Methods *5*, 605 607. https://doi.org/10.1038/nmeth.1220.

Riedl, J., Flynn, K.C., Raducanu, A., Gärtner, F., Beck, G., Bosl, M., Bradke, F., Massberg, S., Aszodi, A., Sixt, M., and Wedlich-Soldner, R. (2010). Lifeact mice for studying F-actin dynamics. Nat. Methods *7*, 168 169. https://doi.org/10.1038/nmeth0310-168.

Rotty, J.D., Wu, C., and Bear, J.E. (2013). New insights into the regulation and cellular functions of the ARP2/3 complex. Nat. Rev. Mol. Cell Biol. *14*, 7 12. https://doi.org/10.1038/nrm3492.

Schindelin, J., Arganda-Carreras, I., Frise, E., Kaynig, V., Longair, M., Pietzsch, T., Preibisch, S., Rueden, C., Saalfeld, S., Schmid, B., et al. (2012). Fiji: an open-source platform for biological-image analysis. Nat. Methods *9*, 676 682. https://doi.org/10.1038/nmeth.2019.

Sens, K.L., Zhang, S., Jin, P., Duan, R., Zhang, G., Luo, F., Parachini, L., and Chen, E.H. (2010). An invasive podosome-like structure promotes fusion pore formation during myoblast fusion. J. Cell Biol. *191*, 1013 1027. https://doi.org/10.1083/jcb.201006006.

Sixt, M., and Lämmermann, T. (2011). In vitro analysis of chemotactic leukocyte migration in 3D environments. Methods Mol. Biol. *769*, 149 165. https://doi.org/10.1007/978-1-61779-207-6_11.

Snapper, S.B., Meelu, P., Nguyen, D., Stockton, B.M., Bozza, P., Alt, F.W., Rosen, F.S., von Andrian, U.H., and Klein, C. (2005). WASP de ciency leads to global defects of directed leukocyte migration in vitro and in vivo. J. Leukoc. Biol. *77*, 993 998. https://doi.org/10.1189/jlb.0804444.

Stewart, S.A., Dykxhoorn, D.M., Palliser, D., Mizuno, H., Yu, E.Y., An, D.S., Sabatini, D.M., Chen, I.S., Hahn, W.C., Sharp, P.A., et al. (2003). Lentivirus-delivered stable gene silencing by RNAi in primary cells. RNA *9*, 493 501. https://doi.org/10.1261/rna.2192803.

Suetsugu, S., and Gautreau, A. (2012). Synergistic BAR-NPF interactions in actin-driven membrane remodeling. Trends Cell Biol. *22*, 141 150. https://doi.org/10.1016/j.tcb.2012.01.001.

Svitkina, T.M. (2018). Ultrastructure of the actin cytoskeleton. Curr. Opin. Cell Biol. *54*, 1 8. https://doi.org/10.1016/j.ceb.2018.02.007.

Taylor, M.J., Perrais, D., and Merri eld, C.J. (2011). A high precision survey of the molecular dynamics of mammalian clathrin-mediated endocytosis. PLoS Biol. *9*, e1000604. https://doi.org/10.1371/journal.pbio.1000604.

Thiam, H.R., Vargas, P., Carpi, N., Crespo, C.L., Raab, M., Terriac, E., King, M.C., Jacobelli, J., Alberts, A.S., Stradal, T., et al. (2016). Perinuclear Arp2/3-driven actin polymerization enables nuclear deformation to facilitate cell migration through complex environments. Nat. Commun. *7*, 10997. https://doi.org/10.1038/ncomms10997.

Thrasher, A.J., and Burns, S.O. (2010). WASP: a key immunological multitasker. Nat. Rev. Immunol. *10*, 182 192. https://doi.org/10.1038/nri2724.

Tinevez, J.Y., Perry, N., Schindelin, J., Hoopes, G.M., Reynolds, G.D., Laplantine, E., Bednarek, S.Y., Shorte, S.L., and Eliceiri, K.W. (2017). TrackMate: an open and extensible platform for single-particle tracking. Methods *115*, 80 90. https://doi.org/10.1016/j.ymeth.2016.09.016.

Tsai, T.Y., Collins, S.R., Chan, C.K., Hadjitheodorou, A., Lam, P.Y., Lou, S.S., Yang, H.W., Jorgensen, J., Ellett, F., Irimia, D., et al. (2019). Ef cient front-rear coupling in neutrophil chemotaxis by dynamic myosin II localization. Dev. Cell *49*, 189 205. e186. https://doi.org/10.1016/j.devcel.2019.03.025.

van den Berg, M.C.W., MacCarthy-Morrogh, L., Carter, D., Morris, J., Ribeiro Bravo, I., Feng, Y., and Martin, P. (2019). Proteolytic and opportunistic breaching of the basement membrane zone by immune cells during tumor initiation. Cell Rep. *27*, 2837 2846. e2834. https://doi.org/10.1016/j.celrep.2019.05.029.

van den Dries, K., Linder, S., Maridonneau-Parini, I., and Poincloux, R. (2019). Probing the mechanical landscape new insights into podosome architecture and mechanics. J. Cell Sci. *132*, jcs236828. https://doi.org/10.1242/jcs.236828.

Veltman, D.M., King, J.S., Machesky, L.M., and Insall, R.H. (2012). SCAR knockouts in Dictyostelium: WASP assumes SCAR s position and upstream regulators in pseudopods. J. Cell Biol. *198*, 501 508. https://doi.org/10.1083/jcb.201205058.

Venturini, V., Pezzano, F., Català Castro, F., Häkkinen, H.M., Jimenez-Delgado, S., Colomer-Rosell, M., Marro, M., Tolosa-Ramon, Q., Paz-Lopez, S., Valverde, M.A., et al. (2020). The nucleus measures shape changes for cellular proprioception to control dynamic cell behavior. Science *370*. https://doi.org/10.1126/science.aba2644.

Walton, J. (1979). Lead aspartate, an en bloc contrast stain particularly useful for ultrastructural enzymology. J. Histochem. Cytochem. *27*, 1337 1342. https://doi.org/10.1177/27.10.512319.

Weigelin, B., Bakker, G.J., and Friedl, P. (2016). Third harmonic generation microscopy of cells and tissue organization. J. Cell Sci. *129*, 245 255. https://doi.org/10.1242/jcs.152272.

Weiner, O.D., Marganski, W.A., Wu, L.F., Altschuler, S.J., and Kirschner, M.W. (2007). An actin-based wave generator organizes cell motility. PLoS Biol. *5*, e221. https://doi.org/10.1371/journal.pbio.0050221.

Wolf, K., Te Lindert, M., Krause, M., Alexander, S., Te Riet, J., Willis, A.L., Hoffman, R.M., Figdor, C.G., Weiss, S.J., and Friedl, P. (2013). Physical limits of cell migration: control by ECM space and nuclear deformation and tuning by proteolysis and traction force. J. Cell Biol. *201*, 1069 1084. https://doi.org/10.1083/jcb.201210152.

Worbs, T., Hammerschmidt, S.I., and Forster, R. (2017). Dendritic cell migration in health and disease. Nat. Rev. Immunol. *17*, 30 48. https://doi.org/10.1038/nri.2016.116.

Yu, C.H., Ra q, N.B., Krishnasamy, A., Hartman, K.L., Jones, G.E., Bershadsky, A.D., and Sheetz, M.P. (2013). Integrin-matrix clusters form podosome-like adhesions in the absence of traction forces. Cell Rep. *5*, 1456 1468. https://doi.org/10.1016/j.celrep.2013.10.040.

Zhang, H., Schaff, U.Y., Green, C.E., Chen, H., Sarantos, M.R., Hu, Y., Wara, D., Simon, S.I., and Lowell, C.A. (2006). Impaired integrin-dependent function in Wiskott-Aldrich syndrome protein-de cient murine and human neutrophils. Immunity *25*, 285 295. https://doi.org/10.1016/j.immuni.2006.06.014.

Zhu, Z., Chai, Y., Jiang, Y., Li, W., Hu, H., Li, W., Wu, J.W., Wang, Z.X., Huang, S., and Ou, G. (2016). Functional coordination of WAVE and WASP in *C. elegans* neuroblast migration. Dev. Cell *39*, 224 238. https://doi.org/10.1016/j.devcel.2016.09.029.

STAR★METHODS

KEY RESOURCES TABLE

Reagent or resource	Source	Identifier
Antibodies		
Monoclonal rabbit anti-Cav1 (clone D46G3)	Cell Signaling	#3267; RRID: AB_2275453
Monoclonal rabbit anti-CHC (clone D3C6)	Cell Signaling	#4796; RRID: AB_10828486
Goat anti-Rabbit IgG (H+L) Cross-Adsorbed Secondary Antibody, Alexa Fluor 488	Invitrogen	#A11008; RRID: AB_143165
CD11c-APC (clone N418)	eBioscience	#17-0114-82; RRID: AB_469346
MHC II (I-A/I-E)-eFlour450 (clone M5/114.15.2)	eBioscience	#48-5321-82; RRID: AB_1272204
Chemicals, peptides, and recombinant proteins		
Lipopolysaccharide (LPS) from *Escherichia coli* 0127:B8	Sigma	#L3129
CellTracker™ Orange CMTMR Dye	Invitrogen	#C2927
CellTrace™ CFSE Cell Proliferation Kit	Invitrogen	#C34554
5-(and-6)-Carboxytetramethylrhodamine, Succinimidyl Ester (5(6)-TAMRA	Invitrogen	#C6123
CellTrace™ Oregon Green® 488 carboxylic acid diacetate	Invitrogen	#C34555
Evans blue	Merck	#E2129-10G
Blasticidin	Invivogen	#ant-bl
Polybrene	Merck	#TR-1003-G
Ficoll-400	Fisher scientific	#BP525
Cytochalasin B	Tocris	#5474
NucBlue™ Live ReadyProbes™ Reagent (Hoechst 33342)	ThermoFisher	#R37605
CK666	Sigma	#SML0006
CK689	Merck Millipore	#182517
para-nitro-Blebbistatin	Axol	#ax494693
mICAM-1/Fc	R&D Systems	#796-IC
Biozym Gold Agarose	Biozym	#850152
UltraPure Agarose	Invitrogen	#16500500
CCL19	Peprotech	#250-27B
Alexa Fluor™ 594 Phalloidin	Thermo Fisher	#A12381
PAcrAm™-g-(PMOXA)	SuSoS Surface Technology	N/A
SYLGARD™ 184 Silicone Elastomer Kit	Dow Corning	#1317318
PureCol®Type I Collagen	AdvancedBioMatrix	#5005
Nutragen®Type I Collagen	AdvancedBioMatrix	#5010
FibriCol®Type I Collagen	AdvancedBioMatrix	#5133
Alexa Fluor™ 594 NHS Ester (Succinimidyl Ester)	ThermoFisher	#A37572
Collagenase D	Roche	#11088858001
DNAse I	Roche	#10104159001
Critical commercial assays		
EasySep Mouse T cell Isolation Kit	STEMCELL Technologies	#19851
Mouse T Cell Nucleofector™ Kit	Lonza	#VPA-1006

(*Continued on next page*)

Continued		
Reagent or resource	Source	Identifier
Experimental models: Cell lines		
Lenti-X^{TM} 293T Cell Line	Takara-Bio	# 632180
Experimental models: Organisms/strains		
Mouse: C57BL/6JRj	Janvier	N/A
Mouse: B6.129S6-Was^{tm1Sbs}/J	The Jackson Laboratory	#019458
Mouse: LifeAct-eGFP	(Riedl et al., 2010)	N/A
Mouse: HEM1-/-	(Leithner et al., 2016)	N/A
Recombinant DNA		
Plasmid: eGFP-Abi1	(Lai et al., 2008)	N/A
Plasmid: eGFP-WASp	(Benesch et al., 2002)	N/A
Plasmid: Cip4-mCherry	(Taylor et al., 2011)	RRID: Addgene_27685
Plasmid: CLC-mCherry	(Taylor et al., 2011)	RRID: Addgene_27680
Plasmid: MLC-eGFP	(Croft et al., 2005)	N/A
Plasmid: LifeAct-mCherry	(Riedl et al., 2008)	N/A
Plasmid: pLenti6.3	Invitrogen	#V53306
Plasmid: pCMV-dR8.91	Creative Biogene	#OVT2971
Plasmid: pCMV-VSV-G	(Stewart et al., 2003)	RRID: Addgene_8454
Software and algorithms		
SerialEM 3.x	(Mastronarde, 2003)	https://bio3d.colorado.edu/SerialEM/
IMOD 4.7	(Kremer et al., 1996)	http://bio3d.colorado.edu/imod
FIJI imaging processing software 1.53f	(Schindelin et al., 2012)	https://fiji.sc/
Imaris software v9	Oxford Instruments	https://imaris.oxinst.com/packages
TrackMate v6	(Tinevez et al., 2017)	https://imagej.net/TrackMate
Ilastik 1.3.2rc2	(Berg et al., 2019)	https://www.ilastik.org
Celltool	Pincus and Theriot, 2007	https://zplab.wustl.edu/celltool/
MATLAB R2020a	The MathWorks	https://ch.mathworks.com/products/matlab
Prism7	GraphPad	https://www.graphpad.com/scientific-software/prism/
Python 3.9.7	Python Software Foundation	https://www.python.org
TraXpert	Original code	https://github.com/SarenT/TraXpert/10.5281/zenodo.5721237
DaVis 8	LaVision	https://www.lavision.de/en/products/davis-software/imaris
Cross-correlation analysis (MATLAB script)	(Mueller et al., 2017)	N/A
Other		
Culture-Inserts 2 Well	Ibidi	#80209
ACLAR® Fluoropolymer-Film	Science Services	#A50426
Cantilevers (spring constants: 0.1 N m^{-1}; tip radius: 10 nm)	Nanosensors	#qp-BioAC

RESOURCE AVAILABILITY

Lead contact

Further information and requests for resources and reagents should be directed to and will be fulfilled by the lead contact, Michael Sixt (michael.sixt@ist.ac.at).

Materials availability

This study did not generate new unique reagents.

Data and code availability

- all data reported in this paper will be shared by the lead contact upon request.
- TraXpert has been deposited at https://github.com and is publicly available
- Any additional information required to reanalyze the data reported in this paper is available from the lead contact upon request.

EXPERIMENTAL MODEL AND SUBJECT DETAILS

Mouse strains

C57BL/6 (Janvier); *WASp-/-* (B6.129S6-*Was*^{tm1Sbs}/J; No. 019458; The Jackson Laboratory); *LifeAct-eGFP* (Riedl et al., 2010); *LifeAct-eGFPxWASp-/-*; *LifeAct-eGFPxHEM1-/-* (Leithner et al., 2016). All strains were backcrossed to and maintained on C57BL/6-background. For *in vivo* studies mice were sex-matched and experiments were performed at the age of 8-12 weeks. Mice were bred and maintained at the local animal facility in accordance with the IST Austria ethics commission and the Austrian law. Permission was granted by the Austrian Federal Ministry of Science, Research and Economy (identi cation code: BMWF-66.018/0005-II/3b/2012).

Primary cells

All primary dendritic cells and T cells originated from 6-12-week-old, male or female mice (see above) and were isolated and cultured as described in detail below. No cell lines used in this study were found in the database of commonly misidenti ed cell lines that is maintained by ICLAC and NCBI biosample. The cell lines were not authenticated. Cell lines tested negative for mycoplasma. Cell culture medium: R10 medium, consisting of RPMI 1640, supplemented with 10% fetal calf serum (FCS), 2 mM L-glutamine, 100 U/ml penicillin, 100 μg/ml streptomycin, and 50 μM 2-mercaptoethanol (all Invitrogen), was used as basic medium for all cells unless stated otherwise. All cells were grown and maintained at 37 °C / 5% CO_2 unless noted otherwise.

METHOD DETAILS

Differentiation and culture of mature dendritic cells

Dendritic cells (DCs) were differentiated from bone marrow (2.0 x 10^6 BM-cells in 10 ml / dish) or transiently immortalized hematopoietic precursors (0.5 x 10^6 precursor cells in 10 ml / dish) (Leithner et al., 2018; Redecke et al., 2013), both originating from 6-12-week-old, male or female *C57BL/6J*, *LifeAct-eGFP*, *WASp-/-*, *LifeAct-eGFPxWASp-/-* or *LifeAct-eGFPxHem1-/-* mice. Immortalization of hematopoietic precursors: the bone marrow of 6-12-wk-old mice was isolated and hematopoietic progenitor cell lines were generated by retroviral delivery of an estrogen-regulated form of HoxB8 (Leithner et al., 2018; Redecke et al., 2013).

Cells were differentiated in 9 ml R10, supplied with 1 ml in-house-generate granulocyte macrophage colony-stimulating factor (GM-CSF) hybridoma supernatant. On day 3, 8 ml R10, supplied with 2 ml GM-CSF, was added. Half of the medium was replaced on day 6. On day 8, lipopolysaccharide (LPS) from *Escherichia coli* 0127:B8 (Sigma) was added to an end concentration of 200 ng/ml to mature DCs overnight.

Puri cation and culture of na ve T-cells

Peripheral LNs and spleens were harvested and homogenized with a 70 μm cell strainer. Untouched primary na ve T cells were isolated with an EasySep Mouse T cell Isolation Kit according to the manufacturer s protocol (STEMCELL Technologies, 19851 A). T-cells were harvested 1 d before imaging and incubated overnight at 37 °C under 5% CO_2 in R10 medium consisting of RPMI 1640 supplemented with 10% FCS, 2 mM l-glutamine, 100 U/mL penicillin 100 μg/mL streptomycin, 1 mM sodium pyruvate, 100x nonessential amino acids and 50 μM 2-mercaptoethanol (all from Invitrogen). T cells were uorescently labeled with 10 μM CMTMR (CellTracker Orange or 2 μM CFSE for 15 min at 37 °C.

Plasmids and lentivirus production

The following fusion constructs were used: eGFP-Abi1 (Lai et al., 2008), eGFP-WASp (Benesch et al., 2002), Cip4-mCherry (Taylor et al., 2011), CLC-mCherry (Taylor et al., 2011), LifeAct-mCherry (Riedl et al., 2008). The MLC-mKate2 fusion construct was generated by exchanging GFP against mKate2 from a previously generated construct (Croft et al., 2005). Fusion-protein-coding lentiviruses were produced Lenti-X^{TM} 293T Cell Line (Takara Bio) by co-transfection of the expression plasmids (pLenti6.3, Invitrogen) with pCMV-dR8.91 packaging (Creative Biogene) - and pCMV-VSV-G envelope plasmids (a gift from B.Weinberg, MIT, USA, Addgene plasmid no. 8454) (Stewart et al., 2003).

Transfection

For transgene delivery, bone marrow-derived DCs were transfected with 4 μg DNA, according to manufacturer guidelines using the nucleofector kit for primary T cells (Amaxa; Lonza Group). Brie y, 5 × 10^6 cells were resuspended in 100 μl reconstituted nucleofector solution and transferred to an electroporation cuvette, and a total amount of 4 μg plasmid DNA was added. Cells were transfected by using a protocol speci cally designed for electroporating immature mouse DCs (program X-001). Transfected DCs were used one day after transfection and enriched by FACS for GFP-expressing cells. Immortalized hematopoietic precursors were spin-infected

(1,500 g, 1 h) with lentiviruses in the presence of 8 μg/ml Polybrene. Following transduction, cells were selected for stable virus insertion using 10 μg/ml Blasticidin (pLenti6.3) for at least 1 week.

Enucleation of matured dendric cells

Enucleation was performed as described previously (Graham et al., 2018). From a 50% (wt/vol) solution Ficoll-400 with PBS (Fisher scienti c BP525) a 30% (vol/vol) stock solution was made with D10 (DMEM containing 10% FBS and 100ul/ml Pen-strep). The stock solution was ltered with a 0.4 PES lter. From the stock solution 30%, 20%, 18%, 15% Ficoll working solutions were prepared freshly on the day of experimentation by adding D10 containing cytochalasin B (10μg/ml) (#5474, Tocris) and DMSO (0.2%). 2 ml of each concentration were layered into an ultracentrifuge tube (13.2 ml thin wall, Thermo sher scienti c), starting with 30% followed by 20%, 18 % and 1ml of 15%. The tube was covered and the gradient was incubated overnight at 37°C. The next day, 1-2x10^7 matured DCs were pelleted and the pelleted was resuspend with 1 ml pre-warmed 15% Ficoll and layered on top of the gradient. The tube was then lled with D10 containing cytochalasin (10μg/ml). The samples were loaded into a pre-warmed SW641 rotor of a Sorval wx100 (Thermos Scienti c). The cells were centrifuged for 1 h at 31°C with 27000rmp (started with acceleration of 9 and stopped with deceleration of 1). After centrifugation the visible cell fraction was pipetted into a 50 ml tube. And the cells were washed 3x with 40 ml PBS at 330g. The cell pellet was resuspended in 1ml R10 medium and transferred into a 24 well plate, 1 drop of nucBlue (#R37605, Life tech.) and vitamin C (50μM) was added. After 30 min cells were spun down and used for the under-agarose assays.

Pharmacological inhibitors

The following small molecule inhibitors were used to perturb actin dynamics. Inhibitors were mixed with the cell suspension and the agarose (before polymerization) using the indicated nal concentration. The Arp2/3 Complex Inhibitor I, CK666 (100 μM; #SML0006; Sigma); the Arp2/3 Complex Inhibitor I, Inactive Control; CK689 (100 μM; #US1182517; Merck Millipore); the Formin FH2 Domain Inhibitor, para-nitro-Blebbistatin (#ax494693; Axol)

Antibodies

Monoclonal rabbit anti-Cav1 (clone D46G3) (#3267) and monoclonal rabbit anti-CHC (clone D3C6) (#4796) antibodies were both purchased from Cell Signaling. Goat anti-rabbit IgG coupled to Alexa488 (#A11008; Invitrogen) was used as secondary antibody. F-actin was labelled using AF-594-coupled Phalloidin (#A12381; Thermo Fisher).

Under-agarose migration assay of na ve T-cells

Glass coverslips were overlaid with 4 μg/mL rmICAM-1/Fc (R&D, 796-IC). An 1% agarose block was formed by mixing (i) one part 2x HBSS buffer (Sigma), (ii) two parts RPMI (Invitrogen) supplemented with 20% BSA (instead of FCS) (Sigma) with 2x concentrations of all other supplements used in R10 medium (see above) and (iii) one part 4% high-molecular weight agarose (Biozym Gold Agarose, 850152) in water at 52 °C. CCL19 (20 ng/ml) (Peprotech, 250-27B) was added to soluble agarose before casting. Liquid agarose was subsequently poured into a dish, covering the coated coverslip. The agarose blocks were allowed to solidify at room temperature and were equilibrated rst at 4 °C for 1 h and subsequently at 37 °C and 5% CO_2 for 30 min. T cells were injected under the agarose block with a micropipette and allowed to polarize for at least 30 min at 37 °C under 5% CO_2 before imaging. Epi uorescence movies were recorded using the same settings as described above. Images were taken every 30 s at 6 multi-positions with NIS Elements software (Nikon Instruments). Spinning disc microscopy was performed on an inverted spinning-disc confocal microscope (Andor) using a 100x/1.4 NA objective and a 488 nm laser line in a custom-built climate chamber (37°C under 5% CO_2). Time-lapse movies were recorded every two seconds.

Under-agarose migration assay of mature dendritic cells on adhesive substrate (invasion under agarose)

Glass coverslips were washed with isopropanol, ethanol, and dH_2O; subsequently, plasma-cleaned (pdc-002 plasma cleaner, Harrick) and glued to a petri-dish with a 17mm hole. To obtain humid migration chambers, a 17 mm plastic ring was attached to a glass-bottom dish using paraf n (Paraplast X-tra; Sigma). Agarose blocks were formed by mixing (i) one part 2x HBSS buffer (Sigma), (ii) two parts RPMI (Invitrogen) supplemented with 20% FCS (Invitrogen) with 2x concentrations of all other supplements used in R10 medium (see above) and (iii) one part 4% UltraPure Agarose (Invitrogen) in water at 52 °C. Increasing agarose stiffnesses were achieved by mixing 2% agarose for low stiffness (2.5 kPa), 4% for intermediate stiffness (10 kPa), and 6% for high stiffness (17.5 kPa) (Biozym Gold Agarose, 850152) (Hons et al., 2018). 500 μl liquid agarose was subsequently poured into a dish, covering the coverslip. The agarose blocks were allowed to solidify at room temperature for 5 min. After polymerization, two 2-mm holes (5 mm apart) were punched into the agarose pad followed by 30 min equilibration at 37°C, 5% CO_2. 2.5 μg/ml CCL19 (PeproTech) was placed into one hole to generate a soluble chemokine gradient. 0.5 x 10^6 mDCs were placed in the second hole opposite to the chemokine hole. Before the acquisition, dishes were incubated at least 2 h at 37°C, 5% CO_2 to allow invasion under the agarose (cells are now con ned between the coverslip and the agarose). During the acquisition, dishes were held under physiological conditions at 37°C and 5% CO_2. Epi uorescence movies were recorded with an inverted wide- eld Nikon Eclipse Ti-2 microscope in a humidi ed and heated chamber at 37 °C and 5% CO_2 (Ibidi Gas Mixer), equipped with a 20x/0.5 NA PH1 air objective, a Hamamatsu EMCCD C9100 camera and a Lumencor Spectra X light source (390 nm, 475 nm, 542/575 nm; Lumencor). Images were taken every 30 s or 3 min at 6 multi-positions with NIS Elements software (Nikon Instruments).

Under-agarose migration assay of mature dendritic cells on slippery substrate (injection under agarose)

Plasma-treated (pdc-002 plasma cleaner, Harrick) glass coverslips were incubated with Poly-2-methyl-2-oxazoline (1 mg/ml for 1h at RT; PAcrAm™-g-(PMOXA); SuSoS Surface Technology) to generate an inert, non-adhesive coating. Agarose blocks were generated as described above. After polymerization (5 min at RT), a 2-mm hole was punched into the agarose pad followed by 30 min equilibration at 37°C, 5% CO_2. 2.5 μg/ml CCL19 (PeproTech) was placed into the hole to generate a soluble chemokine gradient. The cell suspension was injected under the agarose opposite the chemokine hole to con ne migrating DCs between the coverslip and the agarose. Before the acquisition, dishes were incubated at least 2 h at 37°C, 5% CO_2 to allow recovery and persistent migration of cells towards the chemokine source. TIRF microscopy was performed with a 60/1.46 NA oil objective, optovar 1x or 1.6x in a humidi ed and heated chamber at 37°C and 5% CO_2 using an inverted Axio Observer (Zeiss) microscope, a 488 nm laser and an Evolve EMCCD camera (Photometrics) controlled by VisiView software (Visitron Systems). Images were recorded every two seconds. Spinning disc microscopy was performed using the same settings as described for under agarose assays. To record actin spike formation z-stacks of 3 images (0.5 μm step size) were recorded every two seconds. Interference Re ection Microscopy (IRM) was performed on a Leica SP5 inverted confocal microscope. Image acquisition was performed as previously described (Barr and Bunnell, 2009).

Migration in microfabricated pillar forests and straight and constricted channels

Micro uidic devices with pillars were micro-fabricated with polydimethylsiloxane (PDMS) (Leithner et al., 2016). Photomasks were designed using Coreldraw X18, printed on a chrome photomask (1 μm resolution; JD Photo data), followed by a spin coating step using SU-8 2005 (3,000 rpm, 30 s; Microchem) and a prebake of 3 min at 95°C. The wafer was then exposed to 100 mJ/cm^2 ultraviolet light on an EVG 610 mask aligner. After a postexposure bake of 3 min at 95°C, the wafer was developed in propylene glycol methyl ether acetate (PGMEA). A 1h silanization with Trichloro(1H,1H,2H,2H-per uorooctyl)silane was applied to the wafer. The devices were made with a 1:10 mixture of Sylgard 184 (Dow Corning), and air bubbles were removed with a desiccator. The PDMS was cured overnight at 85°C. Microdevices were attached to isopropanol/ethanol-cleaned coverslips and incubated for 1 h at 85°C after plasma cleaning (pdc-002 plasma cleaner, Harrick). Before the introduction of cells, devices were ushed and incubated with complete medium for at least 1 h. Figure S4I: Dimensions of the pillars were 5 x 30 μm (height x width). The spacing between pillars was 20 μm. Figure 4L: 5 x 5 μm (height x width) and 1 μm, 2 μm or 3 μm spacing. Figure 4M: The dimensions of the straight channels are 5 μm width, 4 μm height and the dimensions of constrictions are 1.5 μm width, 4 μm height, 15 μm length. Bright eld movies of DCs migrating pillar mazes were acquired by time-lapse acquisition (time interval of 60 s) using inverted cell culture microscopes (DM IL Led, Leica Microsystems) equipped with cameras (ECO415MVGE, SVS-Vistek) and custom-built climate chambers (5% CO_2, 37°C, humidi ed).

Collagen migration assay

Custom-made migration chambers were assembled by using a plastic dish containing a 17-mm hole in the middle, which was covered by coverslips on each side of the hole (Sixt and Lämmermann, 2011). 3D scaffolds consisting of 0.75 / 1.5 / 3 / 5 mg/ml bovine collagen I (PureCol, Nutragen, Fibricol; all AdvancedBioMatrix) were generated by mixing 1.5 × 10^5 cells in suspension (R10) with collagen I suspension buffered to physiological pH with Minimum Essential Medium and sodium bicarbonate in a 1:2 ratio. To allow polymerization of collagen bers, gels were incubated 1 h at 37°C, 5% CO_2. Directional cell migration was induced by overlaying the polymerized gels with 0.63 μg/ml CCL19 (R&D Systems) diluted in R10. To prevent drying out of the gels, migration chambers were sealed with Paraplast X-tra (Sigma). Bright- eld movies were acquired by time-lapse acquisition (time interval of 60 s) using inverted cell culture microscopes (DM IL Led, Leica Microsystems) equipped with cameras (ECO415MVGE, SVS-Vistek) and custom-built climate chambers (5% CO_2, 37°C, humidi ed).

To visualize collagen bers using spinning disc microscopy, collagen was directly conjugated to Alexa Fluor 594 NHS Ester (Succinimidyl Ester, ThermoFisher). Collagen was added to SnakeSkin Dialysis Tubes, 10K MWCO, 16mm (ThermoFisher), and immersed in 100mM $NaHCO_3$ overnight at 4°C to allow polymerization. Alexa Fluor 594 NHS Ester (1.5mg/mL) was added to the polymerized collagen and incubated for 3h. To remove the unconjugated dye, the collagen mixture was placed in 0.2% acetic acid in deionized water for further dialysis overnight at 4°C.

Imaging of LifeAct-eGFP expressing DCs in Alexa-594-labeled collagen matrices was performed on an inverted spinning-disc confocal microscope (Andor Dragon y 505) using a 60x/1.4 NA objective and a 488 nm / 561 laser line in a custom-built climate chamber (37°C under 5% CO_2). Z-stacks (1.5μm step size) of migrating cells in labeled collagen matrices were acquired using an Andor Zyla camera (4.2 Megapixel sCMOS) every 60 seconds for 20-25min.

Migration on nano-ridges

Fabrication of coverslips with nano-ridges

Clean glass coverslips were coated with a 50 nm re ective layer of chromium. An electron beam resist (AR-P 6200.13) was spin-coated on the chromium covered coverslip. The inverse pattern of ridges was written using the e-beam lithography tool and subsequently developed using AR600-546. Chromium was dry-etched in Cl_2-O_2 plasma inside an ICP (Inductively coupled plasma) chamber. The chamber was pumped to a pressure of 10 mTorr with a gas ow of 26 sccm for Cl_2 and 4 sccm for O_2. The forward power and ICP power were 20 W and 400 W, respectively. Glass was subsequently etched using a SF_6-Ar plasma inside an ICP chamber, pumped to a pressure of 10mTorr with a gas ow of 100 sccm for SF_6 and 67 sccm for Ar. The forward power and ICP power were 100 W and 1500 W, respectively. After dry-etching, the remaining chromium layer was wet etched at room temperature using Chromium etchant. The height

of the ridges is determined by the etching time of the glass surface, on average the etching rate of the glass is around 118.5 nm/min. After the wet etching step, the height of the ridges is veri ed using an atomic force microscope (NX10 from Park Systems) in non-contact mode.

Under agarose assay on nano-ridges

Glass coverslips with ridges were rinsed with isopropanol, ethanol and dH_2O, air-dried and plasma cleaned (pdc-002 plasma cleaner, Harrick). They were then incubated with Poly-2-methyl-2-oxazoline (1 mg/ml for 1h at RT; PAcrAm™-g-(PMOXA); SuSoS Surface Technology) or PLL-PEG (1 mg/ml for 1h at RT; PLL-PEG; SuSoS Surface Technology) to generate an inert, non-adhesive coating. Agarose blocks (1%) were generated as described above and matured DCs or puri ed na ve t-cells were injected under the agarose using a micropipette. Spinning-disc confocal microscopy and TIRF microscopy were performed as described above.

Micropipette indentation assay

Glass bottom dishes (50 mm dish diameter, 14 mm glass diameter, glass coverslips No. 1, Mattek) were plasma cleaned (pdc-002 plasma cleaner, Harrick) and coated with 1x poly-L-lysine (P8920, Merck) in dH_2O for 10 min. Dishes were washed twice with dH_2O and then dried for at least 4h at room temperature. Cells in R10 (mDCs or t-cells expressing LifeAct-eGFP) were incubated for 15 min at 37 °C and dishes were carefully washed once with R10 containing HEPES (10mM; Sigma) to remove oating cells. Dishes were immediately mounted on an inverted spinning-disc confocal microscope (Andor) equipped with a micromanipulator (Eppendorf) and maintained at 37°C in a custom-built climate chamber. Micropipettes (blunt; inner diameter 4 μm; bent angle 30°) (BioMedical Instruments) were centrally positioned over the cell and carefully lowered to indent the cell body. Movies were recorded using a 100x/1.4 NA objective and a 488 nm laser line. Z-stacks of 3 image (0.5 μm step size) were recorded every two seconds.

Electron microscopy

Sample preparation and light microscopy examination (CLEM)

Under-agarose assays were performed as described above with minor modi cations. Removable culture inserts (Cat.No: 81176; Ibidi) were attached to plasma-cleaned (pdc-002 plasma cleaner, Harrick) glass coverslips or tailored Aclar foil (Science Services) (used for serial sectioning). Culture inserts were then lled with 200 μl of agarose-mix and experiments were performed as described above. Dendritic cells were allowed to migrate under the agarose for > 2 H. Samples were subsequently xed in cytoskeleton buffer (10 mM MES buffer, 150 mM NaCl, 5 mM EGTA, 5 mM glucose and 5 mM $MgCl_2$; pH=6.1) containing 2% PFA; 2.5% glutaraldehyde (EMS); 0.01% Triton-X 100 (Sigma); phalloidin-Alexa488 (1:40; Invitrogen) for 30 min at 37°C. After xation, agarose pads and removable culture inserts were carefully removed using a coverslip tweezer. Z-Stacks of palloidin-Alexa488 stained cells were performed on an inverted spinning-disc confocal microscope (Andor) using a 100x/1.4 NA objective and a 488 nm laser line. For CLEM (correlative light and electron microscopy) epi uorescence images of phalloidin-Alexa488 stained cells were recorded with an inverted wide- eld Nikon Eclipse Ti-2 microscope equipped with a 20x/0.5 NA PH1 air objective, a Hamamatsu EMCCD C9100 camera and a Lumencor Spectra X light source (475 nm Lumencor). Images were taken at multi-positions with NIS Elements software (Nikon Instruments). Fluorescent and SEM images (see below) were manually aligned using FIJI.

Scanning electron microscopy

Samples were dehydrated in a graded ethanol series at RT. For further chemical drying, the samples were rst incubated in a 1:1 mixture of 100% ethanol and hexamethyldisilazane (HMDS) for 30min at RT and then transferred to 100% HMDS for 1h at RT. Access HMDS was removed with a pipette followed by overnight evaporation at RT. The cover slips with the dried cells were coated with platinum to a thickness of 5nm using an EM ACE600 coating device (Leica Microsystems). The samples were observed with a FE-SEM Merlin compact VP scanning electron microscope (Zeiss) at 5kV using a secondary electron detector.

Contrast enhancement and resin embedding for serial sectioning

Samples on Aclar foil were post- xed with 1% glutaraldehyde (GA) (EMS) in phosphate buffer (PB; 0.1M, pH 7.4) for 10 min at RT. After a brief wash with PB, samples were contrast-enhanced with 0.5% tannic acid (TA; Sigma) in PB (w/v) for 45 min at 4 °C in the dark. The solution was replaced with freshly prepared 0.5% TA in PB and samples incubated for another 45 min at 4 °C in the dark. After a wash with PB, samples were incubated in 1% aqueous osmium tetroxide (w/v; EMS) for 30 min at 4 °C in the dark. Then, they were washed with Milli-Q water and incubated in 1% aqueous uranyl-acetate (w/v; AL-Labortechnik) overnight at 4 °C in the dark. After wash with Milli-Q water, samples were contrast-enhanced further according to en bloc Walton s lead aspartate staining (Walton, 1979). Samples were incubated in lead aspartate solution for 30 min at 60 °C. After a wash with Milli-Q water, samples were dehydrated in graded ethanol (10%, 20%, 50%, 70%, 90%, 96% and 100%) for 5 min each at 4 °C. They were then placed in propylene oxide puriss. p.a. (Sigma) twice for 10 min at 4 °C and embedded in Durcupan™ ACM epoxy resin (Sigma). To that, hard grade Durcupan™ was formulated by weight as follows: component A 11.4 g, component B 10 g, component C 0.3 g, component D 0.1 g. Samples were consecutively in ltrated in mixtures of 3:1 propylene oxide/Durcupan™, 1:1 propylene oxide/Durcupan™ and 1:3 propylene oxide/Durcupan™ for 1.5 h each at 4 °C. Then they were in ltrated in mere Durcupan™ overnight at RT. The Aclar foil was removed from the resin block with a razor blade under a stereo microscope (Nikon SMZ 800). Trimmed samples were placed on PELCO® Cavity Embedding Molds (Ted Pella Inc.), cavities lled with freshly prepared Durcupan™ and resin cured at 60 °C in an oven over two days.

Serial sectioning and scanning

Embedded samples were trimmed with an Ultratrim diamond knife (Diatome) to a rectangle (70μm x ~1mm) with a slanted side for orientation using an EM UC7 ultramicrotome (Leica Microsystems). Prior to serial sectioning, a 25 x 25mm silicon wafer was plasma

treated using an ELMO glow discharge cleaning system (Agar Scienti c) for increasing the hydrophilicity of the wafer. Serial sections were cut at a thickness of 80 nm using a 4mm Leica AT-4 35° diamond knife (Diatome). Section ribbons were collected onto a plasma treated wafer using the water drain device of the knife. Then the wafer with the serial sections was coated with carbon to a thickness of 5nm using an EM ACE600 coating device (Leica Microsystems) to ensure conductivity. The serial sections were observed under a FE-SEM Merlin compact VP scanning electron microscope (Zeiss) equipped with the Atlas 5.3.2.9 Array Tomography software (Zeiss). The images were acquired using a backscattered (5nm pixel size) and a secondary electron detector (7nm pixel size) at 5kV.

Transmission electron microscopy

For transmission electron microscopy, samples were cut with 70 nm using an EM UC7 ultramicrotome (Leica Microsystems GmbH, Austria) and analyzed with a Tecnai 12 (FEI/Thermo Fisher Scienti c, The Netherlands). Large area montaged images were collected using SerialEM (Mastronarde, 2003) (Webpage: https://bio3d.colorado.edu/SerialEM/), and then stitched in IMOD software (Kremer et al., 1996) (http://bio3d.colorado.edu/imod). The acquisition was carried out using a pixel size of 2.094 px/nm and a 20% overlap of the tiles.

Atomic force microscopy

Glass bottom dishes (30 mm dish diameter, 14mm glass diameter, glass coverslip No. 1, Mattek) were plasma cleaned (pdc-002 plasma cleaner, Harrick) and coated with 1x poly-L-lysine (P8920, Merck) in dH_2O for 10min. Dishes were washed twice with dH_2O and then dried for at least 4h at RT. Cells in R10 (mDCs or t-cells expressing LifeAct-eGFP) were incubated for 15 min at 37°C and dishes were carefully washed once with R10 containing HEPES (10mM; Sigma) to remove oating cells. Dishes were immediately mounted on the atomic force microscope equipped with a climate chamber (37°C). AFM nanoindentation was performed on a Nanowizard4 AFM microscope from JPK Instruments (Bruker) interfaced to an inverted optical microscope (IX81, Olympus). We used cantilevers with spring constants of 0.1 N m^{-1} and a tip radius of 10 nm (qp-BioAC, Nanosensors). Cantilever actual spring constants were determined using the thermal noise method implemented in the JPK software. Using bright eld microscopy, we positioned the tip of the cantilever over the central region above the cell body and performed 5-10 indentation measurements. Force-distance curves were acquired with an approach speed of 2 μm s^{-1} until reaching the maximum set force of 10 nN. Measurements were restricted to indentation depths of 500 nm for T-cells and 1000 nm for DCs (<10% of the height of the cell) to minimize the contribution of the substrate, and to maximize the contribution of the cortex stiffness to cantilever de ection. Elastic moduli (young s modulus) were determined from force-distance curves with the Hertz model as implemented in the JPK analysis software (parabolic model).

Dendritic cell lymph node homing assay

Bone marrow-derived dendritic cells were differentiated and matured as described above. Mature DCs were harvested, counted, and adjusted to $1x10^7$ cells/ml at RT 1xPBS. For labeling, Tetra-Methylrhodamine (TAMRA; TAMRA, SE; 5-(and-6)-Carboxytetramethylrhodamine, Succinimidyl Ester (5(6)-TAMRA, SE; Invitrogen) and Oregon Green® (CellTrace™ Oregon Green® 488 carboxylic acid diacetate, succinimidyl ester carboxy-DFFDA, SE; Invitrogen) was added to a nal concentration of 10 μM TAMRA or 3 μM Oregon Green®, respectively. After a 10 min incubation fresh R10 medium was added to the cell suspension to stop the reaction, and the cells were pelleted. Subsequently, cells were resuspended in pre-warmed (37°C) R10 medium and incubated for another 30 min at 37°C for esteri cation. Finally, cells were washed twice with 1xPBS and subsequently used for experiments.

WT and WASp-/- were differently labeled, mixed at 1:1 ratio, and adjusted to a nal concentration of $4x10^7$ cells/ml in 1xPBS. 25 μl (= $1x10^6$ cells) were injected into the mouse hind footpads. Draining popliteal lymph nodes (LNs) were harvested after 24 h and transferred to a polystyrene FACS tube (Falcon BD) containing 0.5 ml complete DMEM (2.5% FCS (Gibco), 10 mM HEPES (Sigma-Aldrich), 5% penicillin/ streptomycin (Gibco) and 5 % glutamine (Gibco)) for subsequent isolation of the DCs for ow cytometry analysis (one LN per tube). LNs were then opened and cut into pieces in the tube using sterile scissors. Afterwards, LN fragments were incubated in digestion buffer (complete DMEM, 3mM $CaCl_2$ (Sigma-Aldrich), 0.5 mg/ml collagenase D (Roche), 40 μg/ml DNase I (Roche), EDTA 0.5 M, pH 7.2: Ethylenediaminetetraacetic acid (EDTA, Sigma-Aldrich)) for 30 min at 37 °C in a water bath and solution was thoroughly pipetted every 10 min using a 1 ml pipette to further disrupt the fragments. The enzymatic reaction was stopped after 30 min by the addition of 10 mM EDTA. The cell solution was again thoroughly pipetted to disrupt remaining LN fragments and subsequently ushed through a cell strainer into a fresh FACS tube (tube with cell strainer cap, BD Falcon). After washing with FACS-buffer, cells were directly stained with labeled primary antibodies (CD11c (Antigen: CD11c; conjugated: APC; eBioscience; Cat-No 17-0114-82; Clone N418) and mouse MHC II (I-A/I-E) (Antigen: MHC II; conjugated: eFluor450; eBioscience; Cat-No 48-5321-82; Clone M5/114.15.2)), resuspended in an appropriate volume of FACS buffer and used for FACS analysis. Flow-cytometric analysis was performed on FACS Canto II (Becton Dickinson) or FACS Aria III (Becton Dickinson) using FACS DIVA software (Becton Dickinson) for acquisition and FlowJo (Treestar) for analysis.

Intravital two-photon microscopy of popliteal lymph nodes

Freshly puri ed T cells were uorescently labeled with 20 μM CMTMR (CellTracker Orange or 5 μM CFSE for 15 min at 37 °C. After being washed, labeled T cells were i.v. injected retro-orbitally into sex-matched 5- to 10-week-old WT C57BL/6 recipient mice and were allowed to home to lymph nodes for at least 18 h. Recipient mice were anesthetized by intraperitoneal injections of ketamine (50 mg kg^{-1}), xylazine (10 mg kg^{-1}) and acepromazine (4 mg kg^{-1}). The right popliteal lymph node was prepared micro-surgically for intravital microscopy and positioned on a custom-built microscope stage. Care was taken to spare blood vessels and afferent lymph vessels. The prepared LN was submerged in normal saline and covered with a glass coverslip. A thermocouple was placed next to

the LN to monitor local temperature, which was maintained at 37°C. To label blood vessels, 50 µl of Evans blue (1mg/ml) (Merck) were i.v. injected retro-orbitally before imaging. Two-photon microscopy of right popliteal LNs was performed with a Trimscope II multiphoton imaging platform (LaVision Biotech) on an upright Olympus stand. Images were acquired using a Plan-Apochromat 20x/1.0 NA objective (Carl Zeiss Microscopy) with H_2O as an immersion medium. A Chameleon Ti:Sapphire laser (MaiTai) was tuned to 840 nm, and an optical parametric oscillator (OPO) tuned to 1100 nm for simultaneous excitation of CFSE, CMTMR, and Evans blue. Fluorescent signals were collected using four external/non-descanned photomultipliers (PMTs) (3 Hamamatsu H7422-40 GaAsP High Sensitivity PMTs and 1 Hamamatsu H7422-50 GaAsP High Sensitivity red-extended PMT). For four-dimensional analysis of cell migration, z-stacks with 11 25 slices (spacing 4µm) of 250 300 x 250 300 µm *x y* sections were acquired every 20 s for 30 45 min.

Image analysis

FIJI imaging processing software (https:// ji.sc/) was used for basic image and video microscopy analysis (Schindelin et al., 2012).

3D analysis of T-cell migration in LNs

Imaging sequences of image stacks were transformed into volume-rendered four-dimensional movies using Imaris software (v9; Bitplane), which was also used for semiautomated tracking of cell motility in three dimensions. The average track velocity and instantaneous velocities were calculated from the x, y, and z coordinates of cell centroids.

2D analysis of migration assays (under agarose; pillar forests; collagen assays)

The average track velocity and instantaneous velocities were calculated from the x, y-coordinates of the nucleus (under agarose assays of dendritic cells) or the cell centroid (under agarose assay of T-cells / dendritic cells migrating in pillar forests or in collagen gels) tracked in TrackMate (Tinevez et al., 2017) (https://imagej.net/TrackMate).

Analysis of directionality

TrackMate les (XML) were imported to TraXpert (a track analysis software based on R v4.03 and R Shiny v1.6.0). Directionality plots were generated using ggplot2 package v3.3.3 with polar coordinates. Each track was grouped in 12 cardinal directions ranging in ±15° (e.g. -15° to +15° is a cardinal direction at 0°) for each replicate and number of tracks were calculated. Percentage of tracks in each cardinal direction compared to all tracks were calculated. Replicates in each group (e.g. genotype) were aggregated by mean for each cardinal group. Watson s Large-sample non-parametric test was used to test for common mean direction (Pewsey et al., 2013). Trajectory plots were generated by plotting each trajectory starting at the origin of Cartesian coordinate system.

Fraction of time in arrest

T-cells were classi ed as being in arrest when the cell centroid remains con ned within a radius of 2.5 µm during an interval of 1 min. Dendritic cells were classi ed as being in arrest when the cell nucleus remains con ned within a radius of 2.5 µm during an interval of 3 min. Fraction of time in arrest was calculated by ratio of the time spent in arrest to the total time.

Segmentation of actin patches

To quantify the area and dynamics of actin patches we rst segmented actin patches from LifeAct-eGFP expressing cells with interactive machine-learning using Ilastik (Berg et al., 2019). Training was performed on WT cells and the same trained work ows were then applied to WASp-/- cells. To measure the dynamic changes of actin patches from frame to frame, we calculated the Jaccard similarity coef cient, de ned by the overlap of segmented actin patches of one frame with the segmentation of the previous frame divided by the area of the union of both. Hence, highly persistent actin patches would lead to a Jaccard coef cient of 1.

Shape analysis

Dendritic cell bodies were segmented from uorescent images (LifeAct-eGFP) by thresholding and conversion into binary images using FIJI (Schindelin et al., 2012). Polygonal outlines were extracted from segmentation masks and sampled at evenly spaced 200 points. To ensure that all polygons were orientated equally, an algorithm based on Procrustes analysis was used to rotate and translate the polygons until corresponding points were optimally aligned. We used the nucleus as a characteristic landmark de ning the cell body of a migrating dendritic cell. Nuclei were extracted from uorescent images (Hoechst) in FIJI and converted to another set of binary images. This additional landmark was used in the Procrustes procedure and improved the alignment. Finally, the alignment was manually veri ed. The following cellular characteristics were measured (1) aspect ratio = long axis/short axis, (2) the average diameter of the contour along the central axis, (3) length of the central axis and (4) normalized polygon curvature at the cell front was measured as an approximation of leading-edge roughness (The average of the absolute values of the point wise curvature of the contour is computed over a speci ed range, and multiplied by the contour length over the same range. Absolute values must be used because otherwise positive and negative curvatures would cancel out; the sum is multiplied by the arc length to make the measurement scale-invariant.) All algorithms are implemented in the Celltool software package (Pincus and Theriot, 2007).

Cross-correlation analysis and bootstrapping statistics

To compare the temporal dynamics of two parameters (speed, aspect ratio, uorescence of actin patches, nuclear area) and test for the statistical signi cance of the temporal offset we used cross-correlation analysis with a custom-written MATLAB script (MATLAB; R2020a) (Mueller et al., 2017). Bootstrapping statistics was performed as described in (Tsai et al., 2019). Bootstrapping was used to obtain the 95% con dence interval of each cross-correlation value. Time traces of x and y were randomly permuted, and the same cross-correlation analysis to obtain the maximal correlation with all possible temporal offsets was performed. This process was then repeated 2000 times to obtain a distribution of maximal correlation value. The 95% con dence interval indicated a correlation value better than 95% of the maximal correlation values one can obtain with a pair of randomly permuted x and y.

Particle Image Velocimetry of collagen matrices

The displacement vectors of collagen bers deformed by migrating DCs were calculated with the software Davis 8 (LaVision) applying Particle Image Velocimetry (PIV) on spinning-disc confocal images. Further post-processing was carried out using a custom-written Python script for extracting the maximum of deformation from frame-to-frame. Considered vectors were limited to the vicinity of the cell boundary corresponding to twice the cell area, which initially was determined by the LifeAct-eGFP expression.

QUANTIFICATION AND STATISTICAL ANALYSIS

All of the statistical details of experiments can be found in the gure legends, including the statistical tests used, exact value of n, what n represents, de nition of center, and dispersion and precision measures. Appropriate control experiments were performed for each biological replicate. All replicates were validated independently and pooled only when showing the same trend. Statistical analysis was conducted using Prism7 (GraphPad). D Agostino Pearson omnibus K2 test was used to test for Gaussian or non-Gaussian data distribution, respectively. When data were normal distributed t test was used. When data were non-normal distributed Kruskal-Wallis with Dunn s test or two-tailed Mann-Whitney test was used. Statistical tests used for individual experiments are indicated in the gure legends.

Developmental Cell, Volume *57*

Supplemental information

WASp triggers mechanosensitive actin patches to facilitate immune cell migration in dense tissues

Florian Gaertner, Patricia Reis-Rodrigues, Ingrid de Vries, Miroslav Hons, Juan Aguilera, Michael Riedl, Alexander Leithner, Saren Tasciyan, Aglaja Kopf, Jack Merrin, Vanessa Zheden, Walter Anton Kaufmann, Robert Hauschild, and Michael Sixt

Supplementary Figure S1. Related to Fig. 1

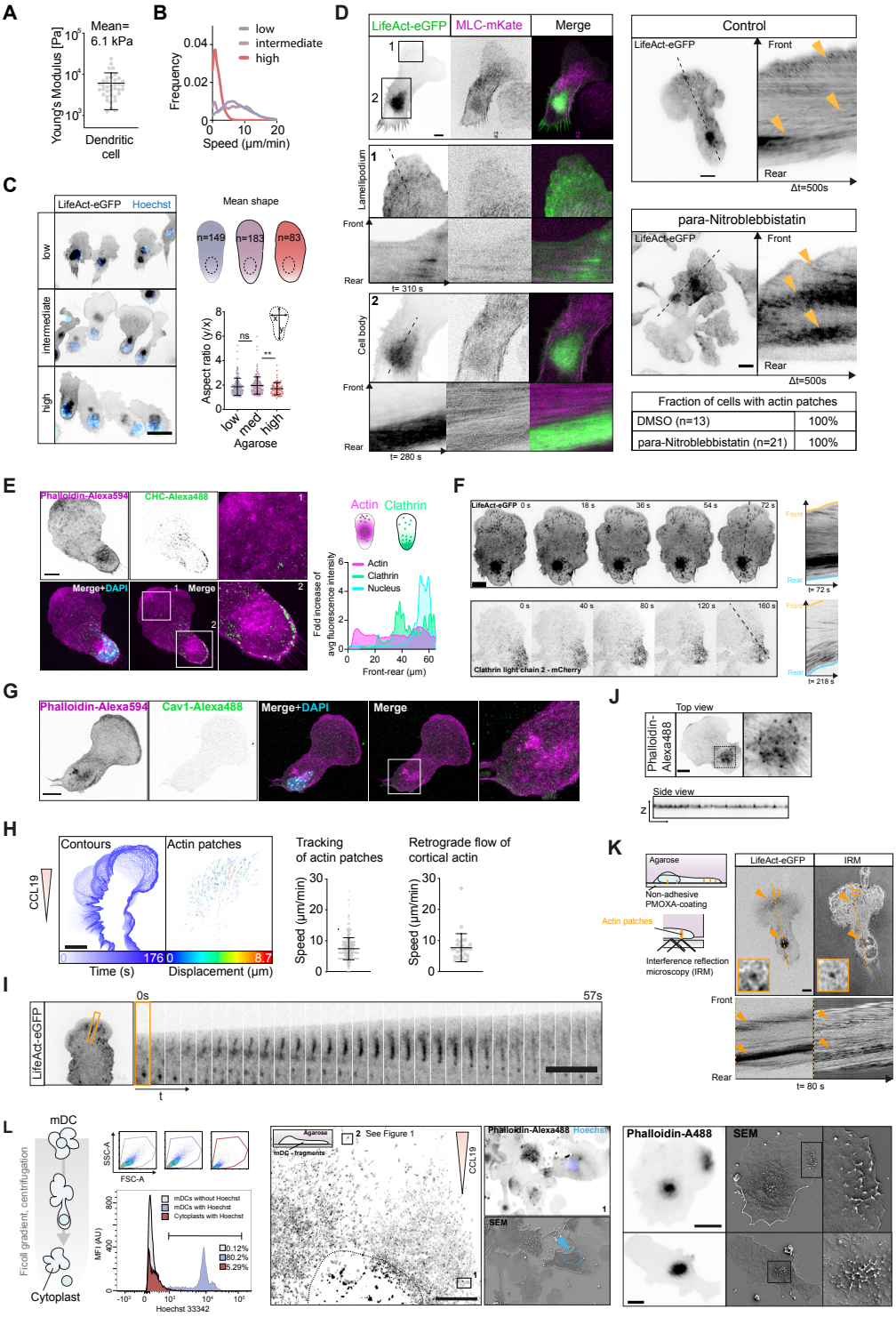

Figure S1. Related to Figure 1. Dendritic cells form actin patches in response to restrictive environments (**A**) Atomic force microscopy of mature DCs. Each data point represents one cell; n=37. (**B**) Frequency distribution of instantaneous cell speeds (smoothed histogram) under the load of agarose (also see Figure 1C). (**C**) Representative epifluorescence micrographs of DCs migrating under agarose of different stiffness; scale bar=30 µm. Cell contours were extracted from LifeAct-eGFP signal and mean cell shape and aspect ratios were calculated (right panel). Kruskal-Wallis/Dunn's multiple comparisons test; **: p=0.0093. ns=not significant. (**D**) Left: Dual labelling of actin (LifeAct-eGFP) and myosin light chain (MLC-mKate). Representative micrographs and kympgraphs show spatio-temporal distinct pattern of LifeAct-eGFP and MLC-mKate. Right: pharmacologic inhibition of myosin IIa activity using para-Nitroblebbistatin (50 µM) had no impact on the formation of actin patches. Scale bars=10 µm. (**E**) Subcellular distribution of endogenous clathrin was analyzed by immunostaining of clathrin heavy chain (CHC). Representative image shows that distribution of CHC-pve punctae is distinct from actin patches (Phalloidin); scale bar=10 µm. (**F**) Overexpression of clathrin light chain 2-mCherry confirmed spatio-temporal distinct patterns of clathrin structures compared to actin patches; scale bar=10 µm. (**G**) Subcellular distribution of endogenous caveolae was analyzed by immunostaining of Caveolin1 (Cav1). Representative Image shows that distribution of Cav1 punctae is distinct from actin patches (Phalloidin); scale bar=10 µm. (**H**) Contours and actin patches (segmented from spinning disc confocal movies (LifeAct-eGFP) in Ilastik and tracked with TrackMate) of a representative cell; Δt=176 s; also see Movie S1). Color-code shows displacement of actin patches in µm. Scale bar=10 µm. Tracking of actin patches (n=481 tracks pooled from 2 cells) revealed mean speed comparable to the mean speed of bulk cortical actin flows as analyzed in kymographs (n=28 cells); Mean±SD. (**I**) Spinning disc confocal image sequence showing elongation of actin patches into stripes. Scale bar=10 µm. (**J**) Confocal z-scan of fixed cell stained with phalloidin-Alexa488; scale bar=10 µm. (**K**) Representative micrograph of Interference Reflection Microscopy (IRM) of a dendritic cell migrating under agarose on a PMOXA-coated (non-adhesive) substrate. Dark regions in IRM image correspond to close cell-substrate contacts. Notably, dark spots in IRM image co-localize with LifeAct-eGFP-pve actin patches (see arrow-heads and insets); scale bar=10 µm. (**L**) Nucleus-free cytoplasts were generated by density-gradient ultracentrifugation. Efficiency of cytoplast formation confirmed by FACS (Hoechst staining). Cytoplasts migrate under agarose (chemotaxis towards CCL19). Epifluorescence microscopy confirms the absence of nuclei; scale bar=500 µm. Of note, the few cells with remaining nucleus were identified by Hoechst staining and excluded from the analysis. CLEM showing the presence of knob-like protrusions in cytoplasts, both at the leading edge and the center; scale bar=10 µm.

Supplementary Figure S2. Related to Fig. 2

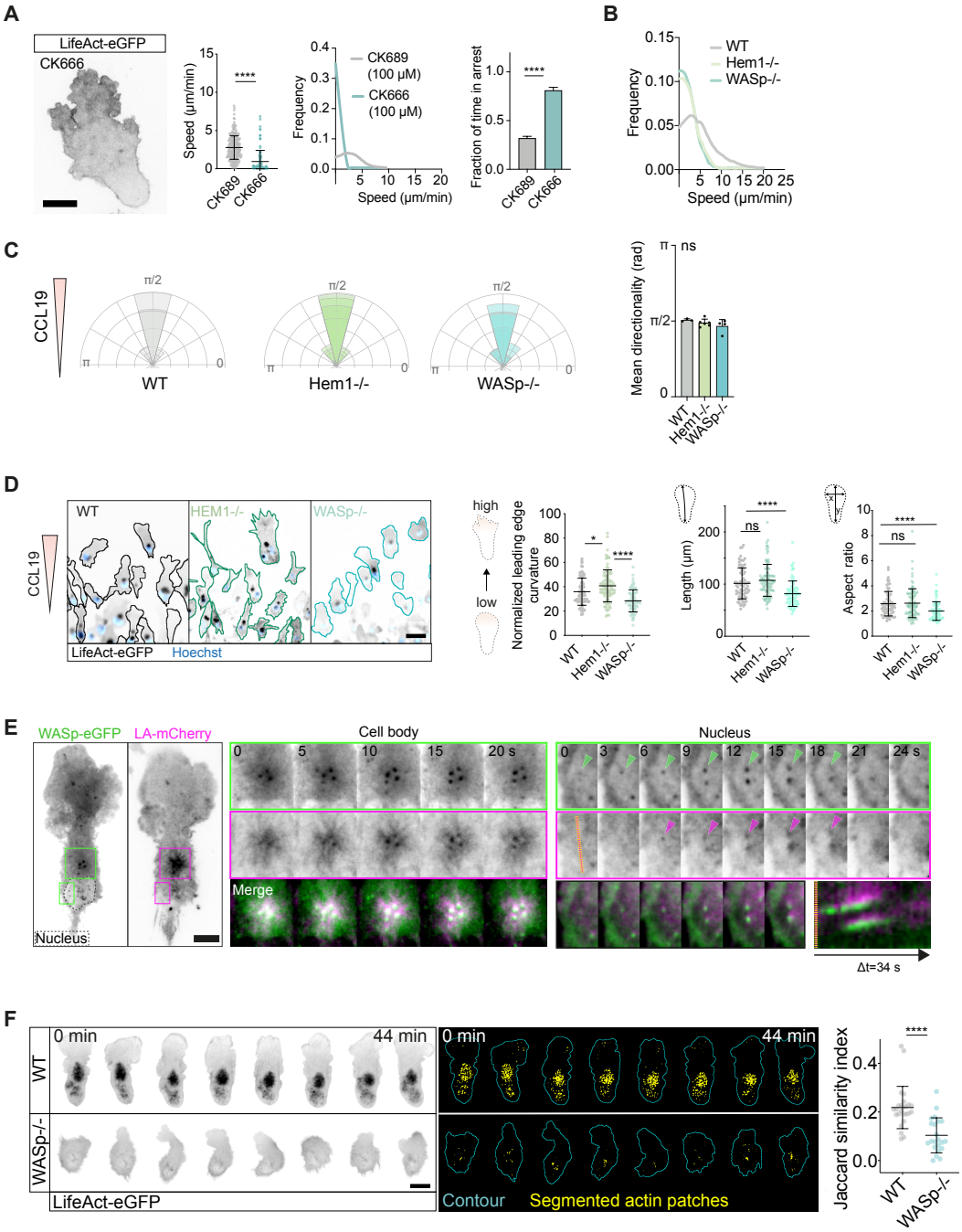

Figure S2. Related to Figure 2. WASp-driven actin patches polymerize orthogonal to WAVE-driven lamellipodia. (A) WT DCs (Hoxb8-derived) were treated with the small molecule inhibitor CK666 (Arp2/3-inhibitor) (100 µM) to block actin polymerization. Representative micrographs (spinning disc confocal microscopy): actin patches were absent in CK666-treated cells. Mean track speed of DCs migrating under intermediate-stiff agarose. Each data point represents one track; Mean±SD. CK689 (inactive control): n=289 pooled from 4 experiments; CK666: n=105 pooled from 6 experiments; Mann Whitney test; ****: p<0.0001. Middle panel: Frequency distribution of instantaneous cell speeds (smoothed histogram). Right panel: Fraction of time in arrest was extracted from tracks; Mean+SEM; Mann Whitney test and Kruskal-Wallis/Dunn's multiple comparisons test; ****: p<0.0001. (**B**) Frequency distribution of instantaneous cell speeds (smoothed histogram). (**C**) Directionality plots and quantification of mean directionality of DCs migrating along a CLL19 chemokine gradient. WT: n=3; Hem1-/-: n=6; WASp-/-: n=4 experiments; Kruskal-Wallis/Dunn's multiple comparisons test; (Mean+SD). (**D**) Representative epifluorescence micrographs of DCs migrating under intermediate-stiff agarose; scale bar=50 µm. Cell contours were extracted from LifeAct-eGFP signal; WT: n=75; Hem1-/-: n=100; WASp-/-: n=84. Contours were further analyzed for leading edge curvature, aspect ratio and cell length; Kruskal-Wallis/Dunn's multiple comparisons test; *: p=0.0466, ****: p<0.0001. (**E**) Dual-labeling of LifeAct-mCherry and WASp-eGFP (TIRF microscopy); scale bar=10 µm. (**F**) Time series of epifluorescence (LifeAct-eGFP) and segmented actin patches in WT and WASp-/- DCs (related to Figures 2 G, H). Cell contours were stabilized and motion of actin patches is shown in the cell-frame of reference. Scale bar=20 µm. Jaccard similarity index shows frame-to-frame overlap of segmented actin patches (mean of cell). WT: n=25 cells; WASp-/-: n=23 cells. Mean±SD; Mann-Whitney; ****: p<0.0001; ns=not significant.

Supplementary Figure S3. Related to Fig. 3.

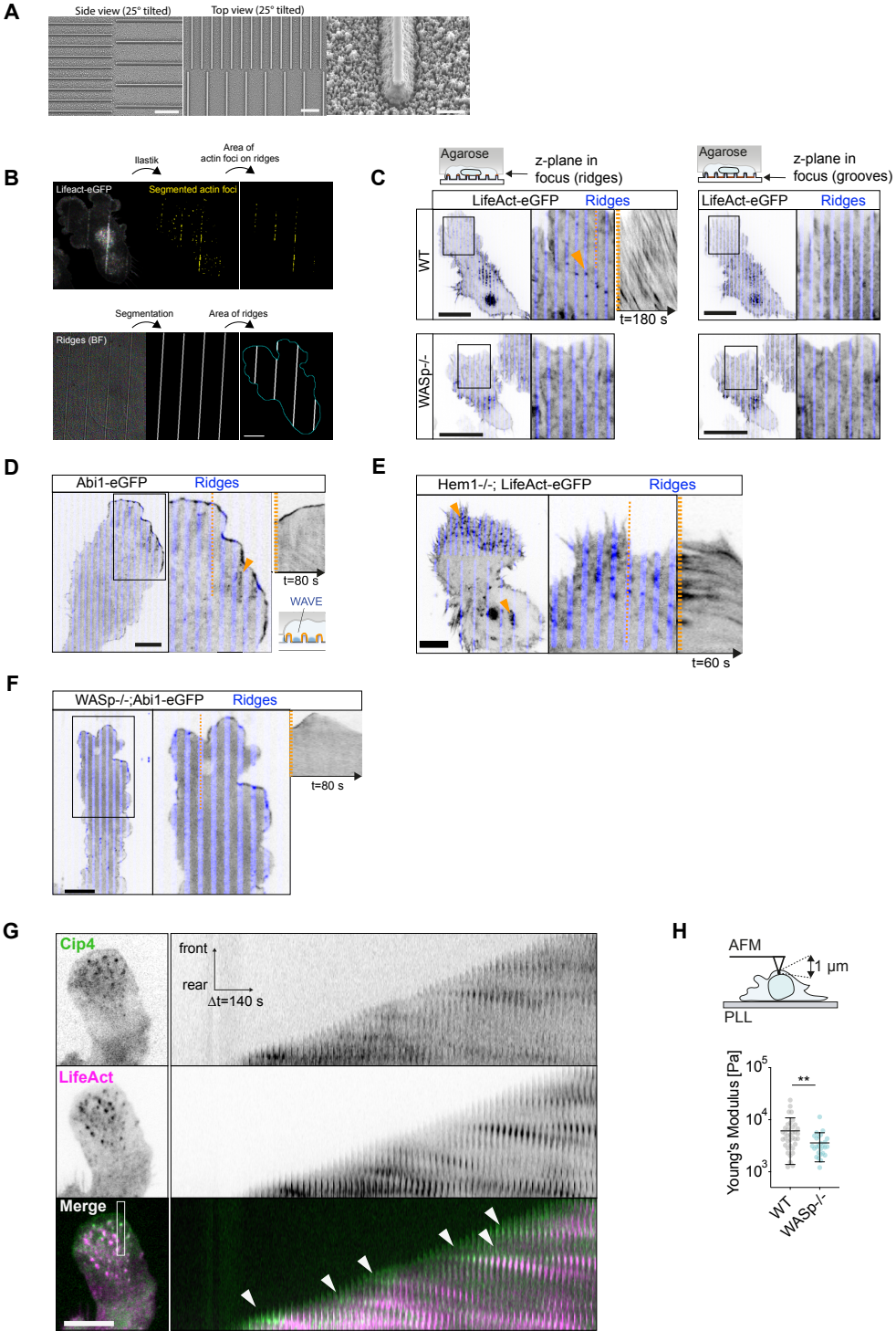

Figure S3. Related to Figure 3. WASp-driven actin patches are triggered by mechanical loading. (**A**) Scanning electron microscopy of coverslips with nano-ridges generated by electron beam lithography. Scale bars: left/middle=10 µm and right=1 µm. (**B**) Quantification of actin patches covering nano-ridges. Upper panel: Actin patches are segmented from LifeAct-eGFP micrographs (spinning disc microscopy) using Ilastik. Lower panel: Ridges are manually segmented from brightfield images using FIJI. Scale bar=10 µm. (**C**) Representative WT and WASp-/- DC migrating on nano-ridges. While actin patches precisely match the pattern of ridges, no actin patches are formed within grooves. Scale bar=20 µm. (**D**) Representative micrograph of Abi1-eGFP expressing DCs migrating on nano-ridges (width: 250nm; height: 600 nm; pitch: 2 µm) (spinning disc confocal microscopy). Abi1-eGFP is restricted to the tip of the lamellipodium. Arrow head shows Abi1-eGFP at lamellipodial protrusion between two agjacent ridges. Scale bar= 20 µm. (**E**) Representative micrograph of LifeAct-eGFP-expressing Hem1-/- DCs migrating on nano-ridges (width: 250nm; height: 600 nm; pitch: 2 µm) (spinning disc confocal microscopy). Actin patches remain targeted to ridges while lamellipodia formation was absent. Scale bar= 10 µm. (**F**) Representative micrograph of Abi1-eGFP expressing WASp-/- DCs migrating on nano-ridges (width: 250nm; height: 600 nm; pitch: 2 µm). Abi1-eGFP remains restricted to the tip of the lamellipodium of WASp-/- DCs. Scale bar= 10 µm. (**G**) Spinning disc microscopy of LifeAct-eGFP (false labeled in magenta) and Cip4-mCherry (false labeled in green) expressing DCs. Kymographs show that formation of Cip4 clusters (arrow heads) precedes the formation of actin patches. Scale bar = 10 µm). (**H**) Schematic of an AFM cantilever indenting a DC adherent to a PLL-coated coverslip (left). Using a Hertz contact mechanics model, the elastic modulus was estimated by fitting the force indentation curves up to 1 µm. Each data point represents one cell. WT: n=37 cells (also see Figure 1b); WASp-/-: n=26 cells; Mean±SD; Mann-Whitney test; **: p=0.0042.

Supplementary Figure S4. Related to Fig. 4.

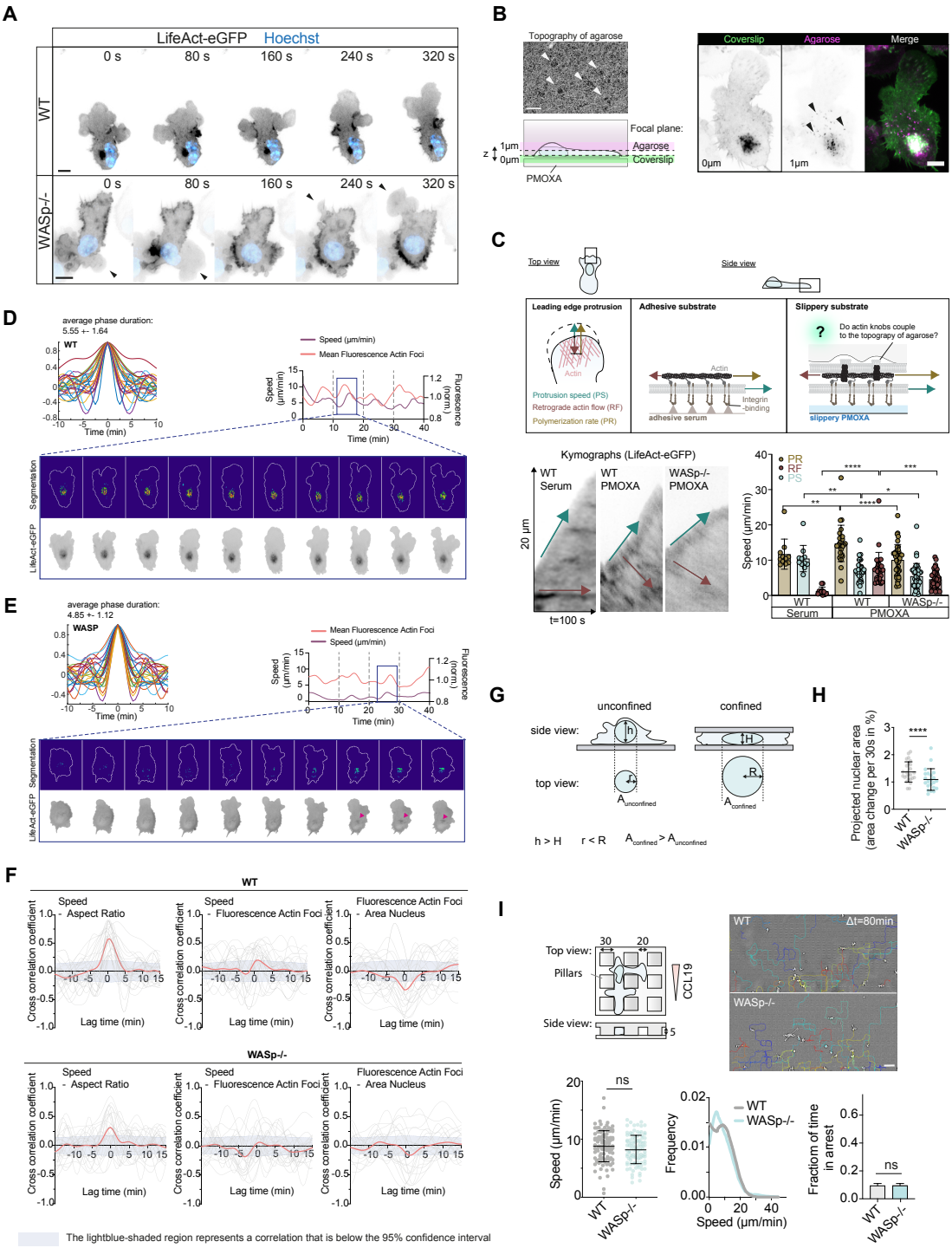

Figure S4. Related to Figure 4. Vertical pushing facilitates locomotion by deforming restrictive environments. (**A**) Representative micrographs of WT and WASp-/- Dcs migrating under agarose on inert, PMOXA-coated coverslips. Arrow heads show formation and retraction of short-lived lamellipodial protrusions. WASp-/- cells showed a less polarized morphology and remained rounded (also see Figures 4A, B). (**B**) Left: SEM image of agarose overlay showing small holes within the agarose (scale bar = 2 µm). Right: Representative z-stack of a DC migrating under agarose (LifeAct-eGFP; spinning disc microscopy). Z-plane of coverslip is indicated by green color; z-plane of agarose is shown in magenta. Of note, small protrusions forming at the dorsal surface of confined DCs can reach into holes of the agarose overlay (arrow heads); scale bar = 10 µm). (**C**) Upper row: Schematic of protrusion and retrograde actin flow velocities upon different degrees of force coupling (adhesive vs. slippery). Retrograde actin flow velocities enhance on slippery substrates (in the absence of integrin-mediated cell-substrate binding) while the protrusion velocity stays constant, leading to an enhanced actin polymerization rate (as the sum of protrusion speed and retrograde flow) at the leading edge. Dendritic cells generate unspecific friction with the topography of their microenvironment to compensate the lack of adhesive interactions with the substrate, raising the question if WASp-dependent orthogonal actin knobs are involved in this process. Lower row: Quantitative analysis of protrusion and retrograde actin flow velocities. Representative kymographs show decreased protrusion speed as well as decreased retrograde actin flows in WASp-/- cells, indicating that impaired coupling to the topography (which would increase retrograde actin flow) is unlikely to explain impaired protrusion formation in WASp-/- DCs. (**D, E**) Autocorrelation of speed traces show that both WT and WASp-/- cells migrating under agarose undergo alternating phases of high/low speed motion with an average phase duration of approx. 5 min. In WT cells, time traces of segmented (Ilastik) actin patches revealed a maximum intensity preceding the acceleration phase by approx. 1-2 mins (also see 4E). In WASp-/- cells, the formation of actin patches was virtually absent. Time traces of the remaining actin signal revealed a significant increase of actin intensity during the late deceleration phase of locomotion (approx. 3 min following maximum speed). This increase in actin intensity corresponded to leading edge retraction and a subsequent accumulation of LifeAct-eGFP at the cell body (also see Figure 4J, S4F and Movie S4). (**F**) Cross-correlation between the (1) Cell Speed and Aspect Ratio; (2) Cell speed and Mean Fluorescence of Actin Patches and (3) Mean Fluorescence of Actin Patches and Area of Nucleus. The thick red line represents the mean cross-correlation curve. Thin gray lines represent cross-correlation curves of individual cells (n=22-23). The light-blue shaded region represents a correlation that is below 95% confidence interval as obtained by bootstrapping. (**G**) Projected nuclear area as an indicator of cell height. The nucleus of unconfined DCs is approximately spherical (left), but naturally flattens with increasing confinement, making it a good indicator of cell height (right). h=height; r=radius; A=area. (**H**) Average change of nuclear area (in %) from one frame to the next frame (30s). Each data point shows

the mean of an individual cell (movies were recorded for > 30 frames). Mann-Whitney test. **: p=0.0081. (**I**) DCs migrating in PDMS-based (non-deformable) microfluidic devices with a constant height. Left: Schematic showing dimensions of the pillar array. Representative brightfield micrograph from time-lapse movie showing DCs migrating in a non-deformable (PDMS) microfluidic device with pillars. Tracks of individual cells (color coded) observed for 80 min. Mean track speed: each data point represents one track; WT: n=110; WASp-/-: n=106 pooled from 3 experiments; Mann-Whitney test. Frequency distribution of instantaneous cell speeds (smoothed histogram). Fraction of time in arrest was extracted from tracks; Mean+SEM; Mann-Whitney test; ns=not significant.

Supplementary Figure S5. Related to Fig. 5.

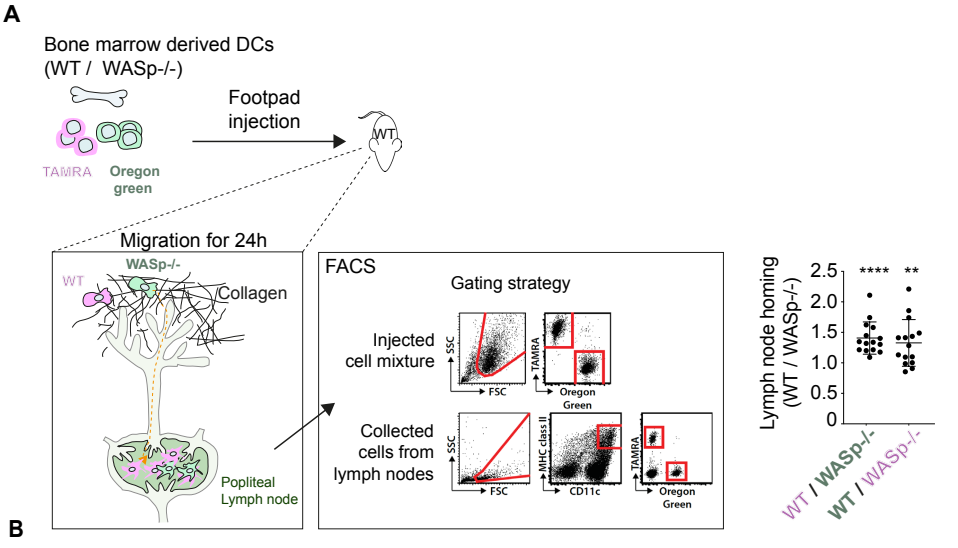

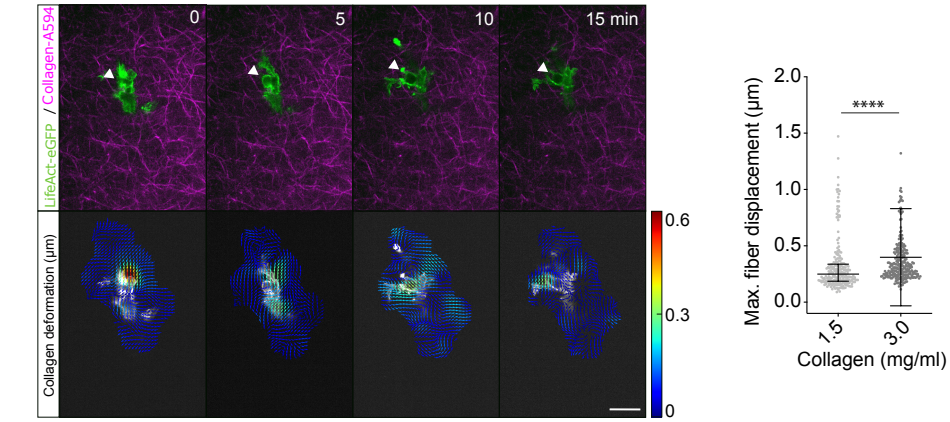

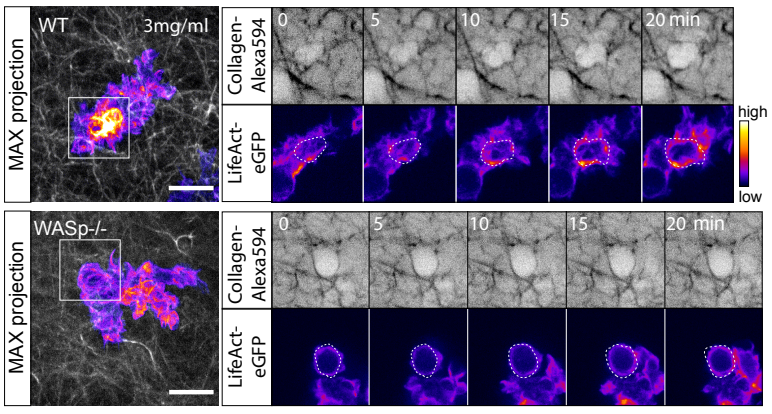

Figure S5. Related to Figure 5. Deformation of collagen fibers is required for migration in fibrous environments. (**A**) Left: Schematic drawing showing the workflow of lymph node homing experiments. Middle: Representative dot plots showing FACS gating strategy. Right: The mean ratio of WT DCs to WASp-/- DCs recruited to draining LNs was significantly larger than 1. Each data point represents the ratio of WT / WASp-/- of one experiment. To control for potential unspecific side effects of fluorescent labelling, fluorescent dyes were switched between WT and WASp-/-. WT (TAMRA) and WASp-/- (Oregon green): n=15; Ratio paired t-test; ****: p<0.0001; WT (Oregon green) and WASp-/- (TAMRA): n=15; Ratio paired t-test; **: p=0.0037. (**B**) Left: Time series of DC (LifeAct-eGFP) migrating in an Alexa-594-labeled collagen gel (3.0 mg/ml) (arrow head: collagen pore) (spinning disc confocal microscopy). Particle image velocimetry (PIV) of the same time series shows deformation of collagen fibers where a pore was dilated (arrow head). Displacement vectors are color coded for displacement in µm. Scale bar=15 µm. Right: Quantification: cells were imaged with 1 min frame-rate for 15-20 min. Each data point represents the maximum magnitude of frame-to-frame deformation; 1.5 mg/ml: n=245 data points pooled from 12 cells (3 independent experiments); 3.0 mg/ml: n=272 data points pooled from 14 cells (7 independent experiments); Median with interquartile range; Mann-Whitney test; ****=p<0.0001. (**C**) Representative time series of WT and WASp-/- DCs migrating in fibrous 3D collagen gels (3.0 mg/ml) (spinning disc confocal microscopy). Left panel shows maximum intensity projection of z scan. Scale bar=10 µm.

Supplementary Figure 6. Related to Fig. 6.

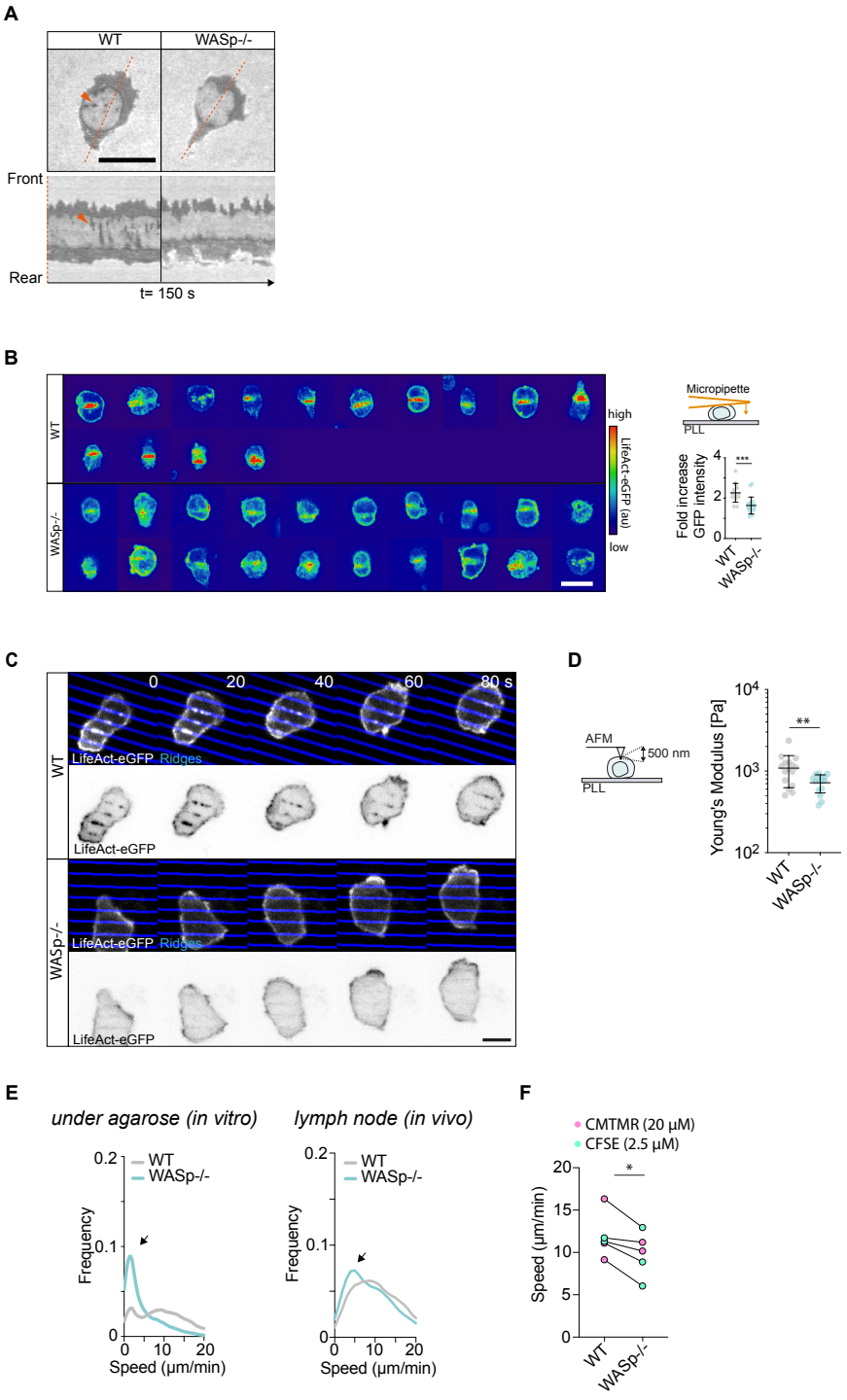

Figure S6. Related to Figure 6. Orthogonal actin patches drive T cell migration in crowded lymph nodes. (A) Representative interference Reflection Microscopy (IRM) of a t cells migrating under agarose on PMOXA-coated (non-adhesive) substrate. Dark regions in IRM image correspond to close cell-substrate contacts. Notably, dark patches flowing backwards are abundant in WT but virtually absent in WASp-/- t cells; scale bar=10 µm. (**B**) T cells attached to poly-l-lysine (PLL)-coated coverslips were pinched from top with a microneedle (schematic). Representative micrographs (spinning disc confocal microscopy) of micropipette indentation experiments. LifeAct-eGFP intensity is color-coded. Scale bar=10 µm. Dot plot showing fold increase of LifeAct-eGFP intensity (area of indentation over non-indented area). Each data point is one indentation experiment. WT: n=14; WASp-/-: n=19; Mean±SD; Mann-Whitney test; ***: p=0.0002. (**C**) Representative time series (spinning disc confocal microscopy) of T cells migrating on nano-ridges. WT cells show sharply delineated actin patches matching the ridge structure. In contrast, formation of actin patches is abrogated in WASp-/- cells. Scale bar= 5 µm. (**D**) Schematic of an AFM experiment. Using a Hertz contact mechanics model, the elastic modulus was estimated by fitting the force indentation curves up to 500 nm. Each data point represents one cell. WT: n= 16; WASp-/-: n= 15; Mean±SD; Mann-Whitney test; **: p=0.0063. (**E**) Frequency distribution of instantaneous cell speeds (smoothed histogram). Left: under agarose (related to Figure 6A). Right: in lymph node (related to Figures 6F-H). (**E**) Pairwise analysis of differentially labeled WT and WASp-/- T cells migrating within the same LN. To control for potential unspecific side effects of fluorescent labelling, fluorescent dyes were switched between WT and WASp-/-. WT: n=5; WASp-/-: n=5; paired t-test; *: p= 0.0196.

4 Migrating immune cells globally coordinate protrusive forces

This chapter appears in full in:
Reis-Rodrigues, P., Avellaneda, M.J., Canigova, N. et al. Migrating immune cells globally coordinate protrusive forces. Nat Immunol 26, 1258–1266 (2025).
https://doi.org/10.1038/s41590-025-02211-w

§Migrating immune cells globally coordinate protrusive forces

Patricia Reis-Rodrigues[1], Mario J. Avellaneda[1], Nikola Canigova[1], Florian Gaertner[1,2], Kari Vaahtomeri[1,3], Michael Riedl[1], Ingrid de Vries[1], Jack Merrin[1], Robert Hauschild[1], Yoshinori Fukui[4], Alba Juanes Garcia[1], Michael Sixt[1]

[1]Institute of Science and Technology Austria (ISTA), am Campus 1, 3400 Klosterneuburg, Austria

[2]Department of Medicine I, University Hospital, LMU Munich, Germany

[3]Translational Cancer Medicine Research Program, University of Helsinki and Wihuri Research Institute, Biomedicum Helsinki, Haartmaninkatu 8, 00290 Helsinki, Finland

[4]Division of Immunogenetics, Department of Immunobiology and Neuroscience, Medical Institute of Bioregulation, Kyushu University; Fukuoka 812-8582, Japan

Correspondence:
Michael Sixt; Sixt@ist.ac.at, phone +43 2243 90003801

Abstract

Efficient immune responses rely on the capacity of leukocytes to traverse diverse and complex tissues. To meet such changing environmental conditions, leukocytes usually adopt an amoeboid configuration, utilizing their forward-positioned nucleus as a probe to identify and follow the path of least resistance among pre-existing pores. We show that in dense environments, where even the largest pores preclude free passage, leukocytes position their nucleus behind centrosome and organelles. The local compression imposed on the cell body by its surroundings triggers assembly of a central F-actin pool, located between cell front and nucleus. Central actin pushes outward to transiently dilate a path for organelles and nucleus. Pools of central and front actin are tightly coupled and experimental depletion of the central pool enhances actin accumulation and protrusion formation at the cell front. Although this shifted balance speeds up cells in permissive environments, migration in restrictive environments is impaired, as the unleashed leading edge dissociates from the trapped cell body. Our findings establish an actin regulatory loop that balances path dilation with advancement of the leading edge to maintain cellular coherence.

Main Text

The composition and geometry of the interstitium can vary substantially between tissue-types, physiological and inflammatory states, posing physical and biochemical challenges for migrating immune cells. Opposed to immune cells, mesenchymal cells, form tight adhesive interactions with the environment and use acto-myosin mediated pulling forces to deform the interstitial matrix[1]. Whenever transient deformation is not sufficient, mesenchymal cells release proteolytic enzymes to digest a path for the cell body[2,3]. This is facilitated by positioning the centrosome and the secretory machinery in front of the nucleus to support local delivery of proteases and adhesion molecules[4,5]. In contrast, fast migrating amoeboid cells, like leukocytes, are more opportunistic[6]. Usually, they neither permanently remodel nor tightly adhere to their environment and position their nucleus forward, followed by the centrosome and organelles[5,7]. This allows them to utilize the nucleus as a gauge to probe their vicinity, select larger pores over smaller ones and thereby navigate along a path of least resistance[8]. Amoeboid and mesenchymal locomotion strategies were long considered cell-intrinsic properties[9]. However, new evidence suggests that in response to specific environmental parameters like extreme confinement, inability to proteolyse and lack of adhesive ligands, mesenchymal cells can also adopt amoeboid features[10,11]. To what extent amoeboid cells can adopt characteristics from mesenchymal migration is less clear[12,13].

Although amoeboid and mesenchymal cells operate in quantitatively very different force-regimes, both rely on the actin cytoskeleton to generate forces. Pulling forces strictly require substrate-specific adhesions that can be accurately quantified by traction force microscopy[14]. Less is known about pushing forces. These can result from cortical acto-myosin contractility due to the build-up of hydrostatic pressure, as exemplified in cellular blebs[15]. Alternatively, actin can also directly polymerize against, and thereby protrude the plasma membrane, as seen in lamellipodia and filopodia. To what extent polymerization-driven pushing forces are sufficient to displace or deform external obstacles is not firmly established[16]. Pushing forces seem especially relevant for amoeboid cells that do not transmit strong pulling forces via adhesion receptors.

To ultimately understand how a cell translates intracellular forces into locomotion of the whole cell body it is important to not only study how isolated adhesions or protrusions act on a substrate, but also how mechanical forces are coordinated on the scale of the whole cell. We used mature dendritic cells (DCs) that we derived from immortalized hematopoietic progenitor cells as a model system for highly migratory immune cells[17]. To test whether DCs can adapt

their locomotion strategy to environments of differential density, we observed the migration of DCs expressing centrin-eGFP, which labels the microtubule-organizing center (MTOC) directionally migrating towards a CCL19 chemokine gradient in collagen gels of varying concentrations (1.7-3.5 mg/mL) **(Fig. 1a)**. After fixation, we quantified the relative position of the MTOC and nucleus (Hoechst) along the polarization axis. In low density gels only 20% of DCs migrated MTOC-first, while this orientation was observed in 60% in high density gels **(Fig. 1b, c)**, indicating that DCs can reorient their organelles when encountering narrow pores. As positioning the MTOC in front of the nucleus is typical for mesenchymal cells, which rely on tight adhesions to the substrate, we generated DCs deficient for talin 1[18] **(Extended Data Fig. 1a, b)**. *Tln1*$^{-/-}$ DCs migrated comparably to *Tln1*$^{+/+}$ in both low and high density collagen gels **(Supplementary Video 1 and Extended Data Fig. 1c)** and displayed similar percentages of cells migrating MTOC-first (15 and 45%, respectively) **(Fig. 1d, e)**, indicating that organelle reorientation was triggered by geometrical changes, but did not depend on substrate adhesions. To challenge this finding in controlled geometries, we chemotactically guided DCs expressing the microtubule plus-end protein EB3 fluorescently labeled with mCherry (EB3-mCherry^{+}) through 1D microfluidic channels with narrow constrictions at the entrance **(Fig. 1f)**. EB3-mCherry^{+} dynamics showed that virtually all microtubules originated from a single location **(Fig. 1f)**, indicating that in DCs the centrosome served as the sole MTOC. Like in collagen gels, organelle orientation was dependent on the cross section of the constriction, with the MTOC-first orientation being more prevalent in smaller cross-sections **(Fig. 1g)**. When advancing through the straight, unconstricted part of the channel, cells frequently reverted to a nucleus-first configuration **(Fig. 1g and Supplementary Video 2)**. Upon entering constrictions, DCs co-expressing EB3-mCherry and the actin reporter LifeAct-eGFP consistently showed an intense actin signal inside the constricted area that, like the MTOC, was located in front of the nucleus **(Fig. 1f, h)**. The intensity of the actin signal increased with decreasing cross-section of the constriction **(Fig. 1i, j)**. In contrast, we observed no obvious actin accumulation in cells migrating through straight channels **(Fig. 1f)**, suggesting that actin accumulation was a response to compression of the cell body. LifeAct-eGFP^{+} DCs migrating under vertical confinement between two surfaces separated by varying distances (3-8 μm) showed a prominent circular-shaped pool of actin that located in the cell center **(Extended Data Fig. 1d and Supplementary Video 2)**. The number of DCs showing the central actin pool increased with decreasing height of confinement **(Extended Data Fig. 1e)**.

Being confined within stiff environments (like in the microfluidic setting) and soft environments (like in vivo tissues, in collagen gels or under layers of soft material), can have different effects on migrating cells. We therefore imaged LifeAct-eGFP^{+} DCs migrating under soft (0.5%) and stiff (1.0%) agarose. In this set-up, where DCs have to lift the deformable layer of agarose **(Fig. 1k)**, the central actin pool was present in virtually all cells **(Extended Data Fig. 1f)**. To understand if adhesions are necessary for the formation of the central actin pool we imaged DCs expressing a GFP tagged version of the focal adhesion protein VASP (Vasp-GFP^{+}) and found that VASP-GFP was absent from the region of the central actin pool **(Supplementary Video 3)**. Moreover, the central actin pool was detectable both in *Tln1*$^{-/-}$ LifeAct-eGFP^{+} and wild-type LifeAct-eGFP^{+} DCs migrating in passivated substrates **(Supplementary Video 3)**, suggesting that formation of the central actin pool did not require adhesive interactions with the substrate. Under soft agarose, only 50% of DCs showed the central actin pool positioned in front of the nucleus **(Fig. 1k, l)**. The prevalence of this configuration increased to 80-85% under stiff agarose, which was accompanied by a higher intensity of the central actin pool **(Fig. 1k-m and Supplementary Video 3)**. Similarly, we also observed a higher prevalence of MTOC-first migrating DCs in stiff agarose (75%) compared to DCs migrating under soft agarose (50%) **(Extended Data Fig. 1g, h and Supplementary Video 3)**. Other organelles like the Golgi apparatus and lysosomes also positioned in front of the nucleus, close to the central actin pool **(Extended Data Fig. 1i)**. Formation of the central pool of actin was not exclusive to DCs, but was also detected in primary activated T cells isolated from wild-type LifeAct-eGFP^{+} mice[19] **(Supplementary Video 5 and Extended Data Fig. 1j, k)**. These observations indicated that, whenever amoeboid migrating immune cells, like DCs and T cells, transited through narrow spaces, they positioned the MTOC and bulk of organelles in front of the nucleus and assembled a mechanosensitive central pool of actin that responded to physical confinement.

To test whether the mechanoresponsiveness of the central actin pool might counter external forces acting orthogonal to the direction of migration, we developed pushing force microscopy. We incorporated fluorescent beads in agarose and tracked bead displacement using kymographic analysis of fast confocal microscopy stacks **(Fig. 2a, Extended Data Fig. 2a and Supplementary Video 6)**. In the absence of cells, beads remained stationary over time. In contrast, when DCs migrated below them, beads were vertically displaced, indicating that DCs transiently deformed the agarose **(Fig. 2b)**. To locate more precisely which cell components contributed to these deformations, we simultaneously imaged the nucleus (Hoechst) and actin (LifeAct-eGFP), while probing bead displacement. Although beads were detectably displaced

by the whole cell body, including the periphery, the displacement was most prominent above the central actin pool **(Fig. 2c and Extended Data Fig. 2b)**. Passage of the nucleus sustained the deformations induced by the central actin pool before the substrate relaxed to its original position during nuclear exit **(Fig. 2d)**. Cross-correlation analysis between bead-displacement and either LifeAct-eGFP or Hoechst signals indicated that bead displacement was strongly correlated with the presence of actin, while the nucleus showed a weaker and asymmetric correlation **(Fig. 2e)**. Similar bead displacements induced by the central actin pool were observed in enucleated DCs **(Fig. 2 f-h and Supplementary Video 6)**, indicating that the ability of the central actin pool to deform the substrate did not depend on the nucleus. We detected similar local substrate deformations associated with actin bursts in DCs migrating through collagen I matrices **(Extended Data Fig. 2c-e and Supplementary Video 7)**. Spatial maps of collagen fiber deformation and actin intensity maxima showed that local maxima of fiber displacements were in close proximity to peaks in LifeAct-eGFP signal **(Extended Data Fig. 2f, g)**. These findings supported the notion that cells encountering confined spaces resorted to actin polymerization in order to locally deform the extracellular environment.

Next, we wondered how perturbations of the central actin pool would impact the ability of cells to migrate and interact with the substrate. Actin dynamics is controlled by the small Rho GTPases Rac1 and Cdc42. While Rac1 mainly triggers actin polymerization at the tip of the lamellipodia via direct interaction with the WAVE complex, which in turn activates Arp2/3 dependent nucleation of new branched filaments, Cdc42 has more pleiotropic effects on cytoskeletal dynamics and cell polarity[20,21]. To probe whether and how these pathways affected the central actin pool, while avoiding deranging the homeostasis of cell shape and membrane dynamics, we treated wild-type DCs migrating under agarose with low concentrations of Rac1 and Cdc42 inhibitors **(Extended Data Fig. 3a-c and Supplementary Video 8)**. While the Rac1 inhibitor NSC23766 did not have an obvious effect on the percentage of DCs showing a detectable central actin pool**(Extended Data Fig. 3d, e)**, Cdc42 perturbation using either ZCL278 or ML141 inhibitors led to a two-fold decrease in the prevalence of the central actin pool **(Fig. 3a, b and Extended Data Fig. 3f, g)** and a reduction of the local F-actin signal in the central pool in comparison to untreated cells **(Fig. 3c and Extended Data Fig. 3h)**. No changes in the total amount of cellular F-actin were observed **(Fig. 3d)**. Moreover, wild-type DCs transiently transfected with a dominant negative mutant of Cdc42 ($Cdc42^{T17N}$-GFP) showed a similar decrease of the percentage of cells with a detectable central actin pool **(Extended Data Fig. 3i, j)**, confirming the key regulatory role of Cdc42.

Among other effectors, Cdc42 triggers WASp-dependent Arp2/3 activation. Analysis of DCs expressing WASp-GFP migrating under agarose showed that WASp-GFP localized not only at the lamellipodium, but also at the region of the central actin pool **(Supplementary Video 9)**[22]. In line with a role for WASp in formation of the central actin pool, the number of *Wasp*$^{-/-}$ DCs with a phalloidin positive central actin pool was reduced to 55% **(Extended Data Fig. 3k, l)**.

Cdc42 interacts with several guanine exchange factors (GEFs), among them DOCK8, which is prominently expressed in the hematopoietic lineage and causative for a severe congenital immunodeficiency associated with actin dysregulation[23–25]. In suspension, *Dock8*$^{-/-}$ DCs were morphologically indistinguishable from wild-type DCs, in line with previous studies[26]. However, when confined under stiff agarose, phalloidin staining revealed a complete lack of the central actin pool **(Fig. 3e, f)**. Notably, WASp-GFP localization at the cell center was also lost, with WASp-GFP dots only detectable at the cellular periphery **(Supplementary Video 9)**. Re-expression of DOCK8-GFP in *Dock8*$^{-/-}$ DCs was sufficient to rescue the wild-type phenotype, and showed that DOCK8-GFP colocalized with the central actin pool but was not present anywhere else throughout the cell, including the leading edge **(Fig. 3g, h)**. DOCK8-GFP also accumulated at the constriction of microfluidic channels **(Fig. 3i, j and Supplementary Video 10)**. Thus, DOCK8 localization at the center of the cell triggered activation of Cdc42 and recruitment of WASp. While actin polymerization triggered by WASp contributed to the formation of the central actin pool, it was not essential, suggesting the participation of other Cdc42 effectors.

To investigate the role of the central pool of actin in cell motility, we imaged the chemotactic migration of *Dock8*$^{-/-}$ DCs confined under agarose. The migration speed of *Dock8*$^{-/-}$ DCs was not different compared to wild-type DCs **(Fig. 4a)**. In pushing force microscopy, *Dock8*$^{-/-}$ DCs inflicted smaller actin-mediated deformations on the agarose **(Fig. 4b, c and Supplementary Video 11)**, with the nucleus being the main bearer of the load in the absence of the central actin pool **(Fig. 4d and Extended Data Fig. 4a)**. In addition, *Dock8*$^{-/-}$ DCs displayed distinct elongated morphology and an incoherent leading edge that often branched in two or more lobes **(Fig. 4e and Supplementary Video 12)**. Phalloidin staining of fixed *Dock8*$^{-/-}$ DCs migrating under agarose revealed that, while the amount of global F-actin was minimally reduced compared to wild-type DCs **(Extended Data Fig.4 b, c)**, the F-actin signal at the leading edge was substantially enhanced (**Fig. 3e, Fig. 4f and Extended Data Fig. 4d**). Our results suggest that the lack of the central actin pool in *Dock8*$^{-/-}$ DCs impaired substrate deformation and was compensated by an hyperstabilized leading edge which resulted in jamming of the cell body.

To better understand the communication between actin at the cell front and actin at the cell body, we imaged the dynamics of these two pools in wild-type LifeAct-eGFP^{+} DCs migrating in polydimethylsiloxane (PDMS) pillar mazes, where small obstacles in the migratory path promote splitting of the lamellipodium **(Extended Data Fig. 4e)**. We observed that lamellipodium retractions were accompanied by an increase of LifeAct-eGFP intensity at the central pool (**Extended Data Fig. 4f, g and Supplementary Video 12)**, while no significant signal variations were detected in other areas of the cell body (**Extended Data Fig. 4g**). Similarly, we observed a strong negative correlation between actin intensity at protrusion sites and in the central pool in actin-eGFP^{+} DCs migrating under agarose **(Fig. 4g, h and Supplementary Video 12)**, suggesting that the two actin pools were strongly coupled and might compete for actin polymerization. To quantitatively assess how this coupling corresponds to migratory dynamics, we perfomed cross-correlation analysis and found that LifeAct-eGFP intensity at the central pool was negatively correlated with both the projected cell area and cell speed **(Fig. 4i, Extended Data Fig. 4h, i and Supplementary Video 12)**. The positive correlation between cell speed and the projected area was lost in *Dock8*$^{-/-}$ DCs **(Fig. 4j)**. These observations suggested that cells redistributed actin between the leading edge and the central pool of actin on demand. Under conditions in which the cell body was largely unobstructed (i.e. in the absence of tight constrictions), actin was enriched at the cell front, enhancing leading edge protrusion and accelerating forward locomotion; when cells faced more constrictive environments, actin was recruited to the central pool **(Fig. 4k)**. This dual use allows actin polymerization to dilate a path for organelles and nucleus, preventing cell entrapment in areas of high confinement, and serves as a "capacitor" by restricting actin accumulation at the cell front, preventing leading edge advancement whenever the cell body is trapped.

Next, we tested whether dysregulation of the central actin pool had a different impact on cell migration depending on the geometry and complexity of the environment. *Dock8*$^{-/-}$ DCs migrating in collagen gels were substantially slower than wild-type DCs **(Fig. 5a, b and Supplementary Video 13),** as previously reported[26–28], and showed signs of enhanced leading edge stabilization as indicated by the formation of multiple simultaneous protrusions **(Fig. 5c).** We also observed a high rate of fragmentation in *Dock8*$^{-/-}$ DCs, which often resulted in cell death **(Fig. 5d),** consistent with findings in T cells[29]. The cell fragments, especially those originating from the leading edge, were often motile and chemotactic **(Fig. 5e).** *Dock8*$^{-/-}$ DCs chemotactically migrating in PDMS mazes with 1-μm to 3-μm-distanced pillars extended multiple protrusions, entangled and often fragmented **(Fig. 5f and Supplementary Video 13)**. However, occasionally, the *Dock8*$^{-/-}$ DCs that adopted a monopolar configuration migrated

significantly faster than *Dock8*$^{-/-}$ DCs with multiple competing leading edges **(Fig. 5g).** To test whether the enhanced leading edge boosted forward locomotion in simple geometries, in which confinement and leading edge splitting was limited, we tested the migration of *Dock8*$^{-/-}$ DCs in straight microfluidic channels. In this set-up, *Dock8*$^{-/-}$ DCs migrated substantially faster than wild-type DCs **(Fig. 5h and Supplementary Video 13)**. Thus, if DCs were not slowed down by restrictions imposed by the environment, redistribution of the central actin pool towards the leading edge enhanced migration**.**

Here we showed that, when confronted with very narrow constrictions, amoeboid cells changed their polar configuration by sweeping the nucleus to the back and positioning the MTOC in front. The local confinement imposed by the environment also triggered the polymerization of a central pool of actin that associated with the MTOC and the bulk of cellular organelles. Actin polymerization in this central region generated pushing forces that not only deformed the surrounding environment of the cell, but could potentially protect the nucleus and other organelles from fatal damage[19,29,30]. This central actin pool was controlled by the activity of the Cdc42 GEF DOCK8 through a mechanosensitive pathway that remains to be identified. An upstream activator of DOCK8 is the Hippo kinase MST1, raising the possibility that this key mechanosensitive pathway that regulates organ shape and size via controlling cell proliferation, might also control the shape of cells through its non-canonical effectors DOCK8 and Cdc42[31]. How different actin pools communicate is poorly understood in animal cells[32], but better studied in yeast, where F-actin forms either patches or cables. In yeast reduction of one structure is balanced by the increase of the other, leaving the overall levels of F-actin conserved[33]. We found a similar homeostatic balance in DCs and described a regulatory loop between the central and the leading-edge pools of actin. Our results suggest that, through this communication axis, cells can coordinate protrusions in two orthogonal directions. Accordingly, DOCK8-deficient cells that lack this coordination fragment, because a chemotactically enhanced leading edge loses contact with an immobilized cell body that is unable to push obstacles away. Together, our findings establish a regulatory loop between cell front and cell body that is essential for maintaining cellular coherence.

Acknowledgements

This research was supported by the Scientific Service Units of ISTA through resources provided by the Imaging and Optics, Preclinical and Lab Support Facilities. In particular, we thank M. A. Symth and F. G. G. Leite, from the Virus Service Team, who helped generating the lentiviral particles used in this study. We thank all the members of the Sixt group for

valuable discussions and feedback. In particular, I. Mayer, for helping with the T cell isolation, and Z. (P.) Li, for providing the Actin-GFP DC line. We are also thankful to J. Mandl and C. Shen for their feedback during the writing of this manuscript. This work was supported by a European Research Council grant ERC-SyG 101071793 to M.S.. M.J.A. was supported by an HFSP Postdoctoral Fellowship LTF 177 2021 and A.J.G by a Lise Meitner Fellowship of the FWF (Austrian Science Fund). Y.F. was supported by the AMED-CREST (JP19gm1310005), the Medical Research Center Initiative for High Depth Omics, and CURE:JPMXP1323015486 for MIB, Kyushu University.

Author Contributions Statement

P.R.-R., A.J.G, K.V, N.C. and M.S conceived the experiments. P.R.-R. performed and analyzed experiments with the help of N.C. and M.J.A.: N.C. performed and analyzed MTOC-nucleus position in microfabricated channels and under agarose; P.R.-R. and M.J.A. performed and analyzed bead displacement experiments in agarose. F.G. provided data of DCs migrating under different agarose stiffness. M.R. wrote image analysis scripts for quantification of the collagen I fiber deformation and actin bursts proximity. I.d.V. and P.R.-R. performed experiments in enucleated dendritic cells. J.M. generated microfabricated channels and pillar arrays. R.H. wrote image-analysis scripts for the analysis of the central actin pool in cells moving in pillar mazes, and cross-correlation analysis of central actin pool, protrusions and cell area/cell speed. Y.F. provided reagents, technical support and advice. P.R.-R., M.J.A. and M.S. wrote the manuscript which was critically reviewed by all other authors.

Competing Interests Statement

The authors declare no competing interests.

Figure Legends

Figure 1: Organelle re-orientation in dendritic cells. **a** Scheme showing the shape and the position of the nucleus in a dendritic cell (DC) migrating in collagen **b**. Representative images of centrin-eGFP^{+} DCs (MTOC, red), labeled with Hoechst in 1.7 and 3.5 mg/mL collagen matrices. Scale bar, 10 µm. **c**. Percentages of DCs with a MTOC-first orientation in 1.7 mg/mL collagen (n=125 cells) and 3.5 mg/mL collagen (n=97 cells) pooled from at least twoindependent experiments. **** P<0.0001. **d**. Representative images of *Tln1*$^{+/+}$ and *Tln1*$^{-/-}$ centrin-eGFP^{+} DCs (MTOC, red) and labeled with Hoechst in 1.7 and 3.5 mg/mL collagen matrices. Scale bar, 10 µm. **e.** Percentages of *Tln1*$^{+/+}$ and *Tln1*$^{-/-}$ DCs with a MTOC-first orientation in 1.7 mg/mL collagen (*Tln1*$^{+/+}$, n=42 cells; *Tln1*$^{-/-}$ n=33 cells) or 3.5 mg/mL collagen (*Tln1*$^{+/+}$, n=44 cells; *Tln1*$^{-/-}$, n=38 cells). 1.7 mg/mL collagen, ns p=0.7640; 3.5 mg/mL collagen, ns P>0.9999. **f**. Scheme showing DCs migrating in microfluidic channels (top) and EB3-mCherry^{+} (MTOC, red, middle) and LifeAct-eGFP^{+} (actin, black, bottom) DCs labeled with Hoechst (middle and bottom) migrating in channels with constrictions of 6 µm x 2.5 µm, 1.7 µm, or 1.2 µm vs. straight 6 µm x 6 µm channels. Scale bar, 10 µm. **g**. Percentages of cells showing MTOC-first orientation in straight channels (CH) and channels with constrictions as in (**f)** CH, n=426 cells; 2.5 µm, n=137 cells; 1.7 µm, n=117 cells; 1.2 µm, n=172 cells fromthree independent experiments. p=0.5495 (CH vs 2.5 µm), p=0.0566 (CH vs 1.7 µm), and **** P<0.0001 (CH vs 1.2 µm). **h**. Percentages of cells with actin-first orientation in channels with constrictions of 2.5 µm (n=138 cells), 1.7 µm (n=119 cells) or 1.2 µm (n=162 cells). Data are pooled from three independent experiments. **** P<0.0001; ns, P=0.6405. **i**. Time lapse of a LifeAct-eGFP^{+} (actin, black) DC labeled with Hoechst entering a 1.7 µm constriction (top three rows) and temporal maximum projection of LifeAct-eGFP of the same DC, with the constricted area is highlighted in blue (bottom). Scale bar, 10 µm. **j**. Ratios between maximum signal within and outside constrictions of 2.5, 1.7 and 1.2 µm width in single LifeAct-eGFP^{+} DCs. Data are pooled from three independent experiments. 2.5 µm, n= 101 cells; 1.7 µm, n=95 cells; 1.2 µm, n=129 cells. **** P<0.0001, ns P=0.5831. **k**. Representative images of LifeAct-eGFP^{+} (actin, black) DCs labeled with Hoechst under 0.5% and 1.0% agarose. Scale bar, 15 µm. **l.** Percentages of DCs with actin-first orientation in 0.5% agarose (n=145 cells) or 1.0% agarose (n=88 cells) pooled from three independent experiments. **** P<0.0001. **m**. Mean intensities of central actin in LifeAct-eGFP^{+} DCs under agarose, normalized to global actin intensity of the same cell integrated over time. Data are pooled from three independent experiments. 0.5% agarose, n= 155 cells; 1.0% agarose, n= 67 cells. ****

P<0.0001. **(b, d, f, i, k)**Hoechst shows nucleus in blue. **c, e, g, h, j, l** Histogram bars are mean +/- s.e.m. **c, e, g, h, l** Two-sided Fisher's exact test. **j, m** two-tailed unpaired Mann-Whitney test .

Figure 2: The central actin pool induces substrate deformations. a. Top view (top) and lateral projection (bottom) of a LifeAct-eGFP$^+$ DC (actin, black) labeled with Hoechst (nucleus, blue) migrating under agarose with fluorescent beads labeled with AF555 showing the cell body under the bead (1), the central actin cloud under the bead (2), the nucleus under the bead (3) (left); and scheme showing a migrating DC under agarose with fluorescent beads (right). Scale bar, 10 μm. **b.** Maximum bead displacement in the absence (no DCs, n=333 beads) or presence (DCs, n=205 beads) of LifeAct-eGFP$^+$ DCs migrating under agarose. **** P<0.0001. Two-tailed unpaired Mann-Whitney test. **c.** Change in bead displacement in Z (beads) and intensities of LifeAct-eGFP (actin) and Hoechst (nucleus) in LifeAct-eGFP$^+$ DCs over 80 minutes. Dashed gray lines highlight the three time points shown in **(a)**. **d.** Contribution of cytoplasmatic, central actin pool and nuclear actin to bead displacement in Z in LifeAct-eGFP$^+$ DCs (n=16 beads) pooled from at leastthree independent experiments (top); and scheme showing bead displacement inflicted by LifeAct-eGFP$^+$ DCs migrating under agarose(botttom). Grey lines connect measurements in the same bead. Dark blue dots show the mean displacement in Z. * P=0.0241 (cytoplasm vs central actin), * P=0.0230 (cytoplasm vs nucleus) and ns, P=0.9998 (central actin vs nucleus). One-way ANOVA. **e**. Temporal cross-correlation between bead displacement and nucleus or actin intensities in LifeAct-eGFP$^+$ DCs migrating under agarose with AF555$^+$ beads. **f.** Top view (top) and lateral projection (bottom) of enucleated LifeAct-eGFP$^+$ DCs (actin, black) labeled with Hoechst (nucleus, blue) migrating under agarose with AF555$^+$ beads showing the cell body under the bead (1) and the central actin pool under the bead (2)**.** Scale bar, 10 μm. **g.** Change in bead displacement in Z (beads) and intensity of LifeAct-eGFP (actin) in LifeAct-eGFP$^+$ enucleated DCs over 60 minutes. Dashed gray lines highlight the two time points shown in **(f)**. **h.** Contribution of cytoplasmic and central actin pool to bead displacement in Z in LifeAc-eGFP$^+$ DCs (n=10 beads) pooled from three independent experiments. ** P=0.083. Two-tailed paired t-test. **b, d, e, h** Error bars are s.e.m.

Figure 3: Cdc42 and its exchange factor DOCK8 regulate the central actin pool. a. Representative images of wild-type DCs migrating under 1.0% agarose treated with DMSO or the Cdc42 inhibitor ZCL278 that were fixed and stained for phalloidin (F-actin, black or red)

and DAPI (nucleus, blue). Scale bars, 10 μm. **b.** Percentages of wild-type DCs treated with DMSO or ZCL278 with a central actin pool in three independent experiments. DMSO, n= 147 cells; ZCL278, n=66 cells. **** P<0.0001. **c.** Mean central actin pool intensity in wild-type DCs as in **(b)**. Mean intensities were normalized to the global actin intensity in each cell. DMSO, n=45 cells; ZCL278, n=61 cells. **** P<0.0001. **d.** Mean total F-actin intensity in wild-type DCs as in **(b)**. DMSO n=45 cells; ZCL278, n=61 cells. ns P=0.7455. **e.** Representative images of wild-type and *Dock8*$^{-/-}$ DCs migrating under 1.0% agarose treated as in **(a)**. Scale bars, 10 μm. **f.** Percentages of wild-type and *Dock8*$^{-/-}$ DCs migrating under 1.0% agarose with a central actin pool in three independent experiments. WT, n= 240 cells; *Dock8*$^{-/-}$, n= 171 cells. **** P<0.0001. **g.** Representative images of *Dock8*$^{-/-}$ DCs expressing GFP (left) or DOCK8-GFP (right) migrating under 1.0% agarose treated as in **(a)**. The red dashed box marks the area used for the inset: top, phalloidin (F-actin, red); bottom, DOCK8-GFP (DOCK8, cyan). Scale bars, 10 μm. Inset, 5 μm**. h.** Percentages of *Dock8*$^{-/-}$ DCs expressing GFP or DOCK8-GFP showing a central actin pool during migration under 1.0% agarose treated as in **(a)**. Data pooled from two independent experiments. GFP, n=47 cells; DOCK8-GFP, n=92 cells. **** P<0.0001. **i.** Top images of *Dock8*$^{-/-}$ DCs expressing GFP (top, black) or DOCK8-GFP (bottom, black) and labeled with Hoechst (nucleus, blue) migrating in PDMS microchannels with 1.7 μm x 6 μm constriction. Scale bar, 20 μm. **j.** Ratio between maximum GFP or DOCK8-GFP density at the constriction and outside of the constriction in GFP^{+} and DOCK8-GFP^{+} DCs as in **(i)**. Data pooled from three independent experiments. GFP, n= 91 cells; DOCK8-GFP, n=53 cells. **** P<0.0001. **b, f, h** Histogram bars are mean +/- s.e.m. **c, d, j** Error bars are s.e.m. **b, f, h** Two-sided Fisher's exact test. **c, d, j** two-tailed unpaired Mann-Whitney test.

Figure 4: Central actin communicates with leading edge actin. a. Scheme showing DCs migrating under agarose(top) and mean speed of wild-type (WT) and *Dock8*$^{-/-}$ DCs migrating under 1.0% agarose (bottom). WT, n=86 cells; *Dock8*$^{-/-}$, n=111 cells from three independent experiments. P=0.1658. **b.** Top view (top) and lateral projection (bottom) of a *Dock8*$^{-/-}$ LifeAct-eGFP^{+} (actin, black) DCs migrating under agarose with AF555^{+} fluorescent beads showing cell body under the bead (left) and nucleus under the bead (right). Hoechst shows the nucleus in blue. Scale bar, 10 μm. **c.** Bead displacement generated by the cell body (excluding the nucleus) in wild-type or *Dock8*$^{-/-}$ DCs for beads on top of the nucleus (nucleus) or beads displaced by the central pool of actin (central actin). WT, n=80 cells; *Dock8*$^{-/-}$, n=17 cells from

three independent experiments. * P=0.0239. **d.** Change in bead displacement in Z (beads) or intensity of LifeAct-eGFP (actin), and Hoechst (nucleus) in *Dock8*$^{-/-}$ LifeAct-eGFP^{+} DCs over 60 minutes. The dashed gray lines highlight the two time points shown in **(b)**. **e.** Time-lapse projection of wild-type (WT, left) and *Dock8*$^{-/-}$ (right) LifeAct-eGFP^{+} (actin, black) DCs migrating under 1.0% agarose. Hoechst shows nucleus in blue. Scale bar, 15 μm **f.** F-actin density at the lamellipodium normalized to the total F-actin density in WT or *Dock8*$^{-/-}$ DCs migrating under 1.0% agarose. WT, n=34 cells; *Dock8*$^{-/-}$, n=26 cells. **** P<0.0001. **g.** Time-lapse projection of a GFP-actin^{+} DC (left) or of segmented protrusions and central actin pool in DCs (right) migrating under 1.0% agarose. Cell contours are shown black. Scale bar, 15 μm **h.** Temporal cross-correlation between central actin and protrusion actin intensities in GFP-actin^{+} DCs (n=81 cells) migrating under 1.0% agarose pooled from three independent experiments. **i.** Temporal cross-correlation between central actin intensity and cell speed or cell area in LifeAct-eGFP^{+} DCs pooled from three independent experiments. n=68 cells. **j.** Temporal cross-correlation between cell area and cell speed in wild-type (WT) and *Dock8*$^{-/-}$ LifeAct-eGFP^{+} DCs migrating under 1.0% agarose pooled from three independent experiments. WT, n=68 cells: *Dock8*$^{-/-}$ n=177 cells. **k.** Scheme showing DCs migrating with a nucleus-first configuration and an actin enriched leading edge in unconstricted environments (1) or DCs with recruitment of actin to the central pool, which promotes deformation of the surrounding environment and reduction of actin at the leading edge in constricted environments (2). **a, c, f, h, i, j,** error bars are s.e.m.**. a, c, f,** Two-tailed Man-Whitney test.

Figure 5: DOCK8 affects dendritic cell locomotion depending on environmental factors. **a.** Representative images of wild-type (WT, top) and *Dock8*$^{-/-}$ (middle, bottom) LifeAct-eGFP^{+} (actin, black) DCs migrating in 1.7 mg/mL collagen showing representative cell shapes during migration (min0-35, top) fragmention(min0-75,middle)or apoptosis (min 0-175, bottom). Cell contour is shown in red. Scale bar, 10 μm **b.** Mean speed of WT and *Dock8*$^{-/-}$ DCs migrating in 1.7 mg/mL collagen over four to six hours. WT, n=59 cells; *Dock8*$^{-/-}$, n=69 cells, from two independent experiments. **** P<0.0001. **c**. Number of simultaneous protrusions in wild-type and *Dock8*$^{-/-}$ DCs migrating as in **(a)**. Dashed lines correspond to the overall mean number of protrusions observed during migration. WT, n=54; *Dock8*$^{-/-}$, n= 67 from two independent experiments P<0.0001. **d.** Fragmentation (left) and death (right) rates in wild-type (WT) and *Dock8*$^{-/-}$ DCs migrating as in **(a)**. WT, n=54 cells; *Dock8*$^{-/-}$, n= 67 cells from two independent experiments. **** P<0.0001. **e.** Percentage of migrating fragments originated from protrusions (Front, n=11 fragments) or the rear (Rear, n= 25 fragments) of *Dock8*$^{-/-}$ DCs in two independent

experiments. ** P=0.0042. **f.** Representative images of wild-type (WT, top) and *Dock8*$^{-/-}$ (middle, bottom) LifeAct-eGFP^{+} (actin, black) DCs labeled with Hoechst (nucleus, blue) moving in pillar mazes with 6 µm in height and 1-µm, 2-µm or 3-µm-distanced pillars (top right) showing *Dock8*$^{-/-}$ DC with a monopolar configuration (*Dock8*$^{-/-}$ single, middle) and with multiple lamellipodia (*Dock8*$^{-/-}$ multi, bottom). Cell contour is shown in red. Scale bar, 20 µm. **g.** Migration speed of wild-type (WT) and *Dock8*$^{-/-}$ DCs with either single lamellipodium (*Dock8*$^{-/-}$ single) or multiple lamellipodia (*Dock8*$^{-/-}$ multi) migrating as in **(f)**. WT, n=45 cells, *Dock8*$^{-/-}$ single, n=18 cells, and *Dock8*$^{-/-}$ multi, n=34 cells from three independent experiments. **** P<0.0001, ** P=0.0033, ns P=0.2748. **h.** Schematic of DC (top) and mean speed of wild-type (WT) and *Dock8*$^{-/-}$ DCs (bottom) in straight PDMS channels. WT, n=83 cells; *Dock8*$^{-/-}$, n= 69 cells in three independent experiments **** P<0.0001. **b, g, h,** error bars are s.e.m. **c, d, e,** histogram bars are mean +/- s.e.m. **b, h,** two-tailed unpaired t-test . **c, d, e,** two-sided Fisher's exact test . **g,** two-tailed unpaired Mann-Whitney test.

References

1. Doyle, A. D., Sykora, D. J., Pacheco, G. G., Kutys, M. L. & Yamada, K. M. 3D mesenchymal cell migration is driven by anterior cellular contraction that generates an extracellular matrix prestrain. *Dev. Cell* **56**, 826-841.e4 (2021).
2. Wolf, K. *et al.* Multi-step pericellular proteolysis controls the transition from individual to collective cancer cell invasion. *Nat. Cell Biol.* **9**, 893–904 (2007).
3. Wolf, K. & Friedl, P. Extracellular matrix determinants of proteolytic and non-proteolytic cell migration. *Trends Cell Biol.* **21**, 736–744 (2011).
4. Infante, E. *et al.* LINC complex-Lis1 interplay controls MT1-MMP matrix digest-on-demand response for confined tumor cell migration. *Nat. Commun.* **9**, 2443 (2018).
5. Yamada, K. M. & Sixt, M. Mechanisms of 3D cell migration. *Nat. Rev. Mol. Cell Biol.* **20**, 738–752 (2019).
6. Wolf, K. *et al.* Physical limits of cell migration: Control by ECM space and nuclear deformation and tuning by proteolysis and traction force. *J. Cell Biol.* **201**, 1069–1084 (2013).

7. Pfisterer, K., Shaw, L. E., Symmank, D. & Weninger, W. The Extracellular Matrix in Skin Inflammation and Infection. *Front. Cell Dev. Biol.* **9**, (2021).
8. Renkawitz, J. *et al.* Nuclear positioning facilitates amoeboid migration along the path of least resistance. *Nature* **568**, 546–550 (2019).
9. Barros-Becker, F., Lam, P.-Y., Fisher, R. & Huttenlocher, A. Live imaging reveals distinct modes of neutrophil and macrophage migration within interstitial tissues. *J. Cell Sci.* jcs.206128 (2017) doi:10.1242/jcs.206128.
10. Wolf, K. *et al.* Compensation mechanism in tumor cell migration : mesenchymal–amoeboid transition after blocking of pericellular proteolysis. *J. Cell Biol.* **160**, 267–277 (2003).
11. Liu, Y.-J. *et al.* Confinement and Low Adhesion Induce Fast Amoeboid Migration of Slow Mesenchymal Cells. *Cell* **160**, 659–672 (2015).
12. Friedl, P. Prespecification and plasticity: shifting mechanisms of cell migration. *Curr. Opin. Cell Biol.* **16**, 14–23 (2004).
13. Alexandrova, A. Y., Chikina, A. S. & Svitkina, T. M. Chapter Four - Actin cytoskeleton in mesenchymal-to-amoeboid transition of cancer cells. in *International Review of Cell and Molecular Biology* (eds. Thomas, C. & Galluzzi, L.) vol. 356 197–256 (Academic Press, 2020).
14. Plotnikov, S. V. & Waterman, C. M. Guiding cell migration by tugging. *Curr. Opin. Cell Biol.* **25**, 619–626 (2013).
15. Schick, J. & Raz, E. Blebs—Formation, Regulation, Positioning, and Role in Amoeboid Cell Migration. *Front. Cell Dev. Biol.* **10**, (2022).
16. Schaks, M., Giannone, G. & Rottner, K. Actin dynamics in cell migration. *Essays Biochem.* **63**, 483–495 (2019).

17. Redecke, V. *et al.* Hematopoietic progenitor cell lines with myeloid and lymphoid potential. *Nat. Methods* **10**, 795–803 (2013).
18. Reversat, A. *et al.* Cellular locomotion using environmental topography. *Nature* **582**, 582–585 (2020).
19. Shen, C. *et al.* DOCK8 regulates a mechanosensitive actin redistribution that maintains immune cell cohesion and protects the nucleus during migration. 2024.07.26.605273 Preprint at https://doi.org/10.1101/2024.07.26.605273 (2024).
20. Lämmermann, T. *et al.* Cdc42-dependent leading edge coordination is essential for interstitial dendritic cell migration. *Blood* **113**, 5703–5710 (2009).
21. Etienne-Manneville, S. Cdc42 - the centre of polarity. *J. Cell Sci.* **117**, 1291–1300 (2004).
22. WASp triggers mechanosensitive actin patches to facilitate immune cell migration in dense tissues | Elsevier Enhanced Reader. https://reader.elsevier.com/reader/sd/pii/S1534580721009497?token=DD1D1937F09C0247B7592407706C0CFD7FDA9D7F99C95D53CF5541D03FF67CAFC6501CB104814494D0001626BCF9B2B4&originRegion=eu-west-1&originCreation=20221109091232 doi:10.1016/j.devcel.2021.11.024.
23. Su, H. C. Dedicator of cytokinesis 8 (DOCK8) deficiency. *Curr. Opin. Allergy Clin. Immunol.* **10**, 515–520 (2010).
24. Kearney, C. J., Randall, K. L. & Oliaro, J. DOCK8 regulates signal transduction events to control immunity. *Cell. Mol. Immunol.* **14**, 406–411 (2017).
25. Su, H. C., Jing, H., Angelus, P. & Freeman, A. F. Insights into immunity from clinical and basic science studies of DOCK8 immunodeficiency syndrome. *Immunol. Rev.* **287**, 9–19 (2019).

26. Harada, Y. *et al.* DOCK8 is a Cdc42 activator critical for interstitial dendritic cell migration during immune responses. *Blood* **119**, 4451–4461 (2012).
27. Krishnaswamy, J. K. *et al.* Coincidental loss of DOCK8 function in NLRP10-deficient and C3H/HeJ mice results in defective dendritic cell migration. *Proc. Natl. Acad. Sci.* **112**, 3056–3061 (2015).
28. Schneider, C. *et al.* Migration-induced cell shattering due to DOCK8 deficiency causes a type 2–biased helper T cell response. *Nat. Immunol.* **21**, 1528–1539 (2020).
29. Zhang, Q. *et al.* DOCK8 regulates lymphocyte shape integrity for skin antiviral immunity. *J. Exp. Med.* **211**, 2549–2566 (2014).
30. Thiam, H.-R. *et al.* Perinuclear Arp2/3-driven actin polymerization enables nuclear deformation to facilitate cell migration through complex environments. *Nat. Commun.* **7**, 10997 (2016).
31. Alraies, Z. *et al.* Cell shape sensing licenses dendritic cells for homeostatic migration to lymph nodes. *Nat. Immunol.* **25**, 1193–1206 (2024).
32. Rotty, J. D. *et al.* Profilin-1 Serves as a Gatekeeper for Actin Assembly by Arp2/3-Dependent and -Independent Pathways. *Dev. Cell* **32**, 54–67 (2015).
33. Burke, T. A. *et al.* Homeostatic Actin Cytoskeleton Networks Are Regulated by Assembly Factor Competition for Monomers. *Curr. Biol.* **24**, 579–585 (2014).

Methods

Mouse strains

In this study, the following mice lines were used: *C57BL/6 (Janvier); LifeAct-eGFP*[34]; *Dock8*$^{-/-}$ [26]; *Wasp*$^{-/-}$ (B6.129S6-Wastm1Sbs/J; No. 019458; The Jackson Laboratory). All mice used were bred on a *C57BL/6* background and maintained at the Institute of Science and Technology Austria Institutional animal facility following the guidelines from its ethics commission and the Austrian law for animal experimentation.

Generation and maintenance of immortalized hematopoietic progenitor cells

Hematopoietic progenitor cells were generated from the isolated bone marrow of 8 to 10-week-old mice which were retrovirally infected with an estrogen-regulated HoxB8 as described before[35,36]. Conditionally immortalized early hematopoietic progenitor cells were kept in R10 medium (RMPI 1640 supplemented with 10% fetal calf serum (FCS), 2 mM L-glutamine, 100 U/mL penicillin, 100 µg/mL streptomycin, and 50 µM β-mercaptoethanol (all Invitrogen), supplemented with 0.01% β-estradiol and 5% of in-house-generated Flt3l containing supernatant). All cells were kept at 37 °C and 5% CO_2 until differentiation.

Constructs used for reporter progenitor cell lines

eGFP-Centrin positive cells were generated from a human centrin1 construct (a gift from Ana-Maria Lennon-Dumenil's lab)[37]. eGFP-WASp[38], LifeAct-mCherry, LifeAct-GFP[39], EMTB-mCherry and EB3-mCherry expressing DCs[40] were generated as described before[42]. GFP and DOCK8-GFP plasmids[43] and GFP-actin plasmid[41] (a gift from Michael Davidson to Addgene, plasmid #56421) were modified to a pLenti6.3 backbone using Gibson Assembly strategy.

Lentivirus production and transduction into progenitor cells

Fusion-protein-coding lentiviruses were produced in Lenti-X-293 cells derived from HEK 293 cells (TakaraBio). Lenti-X-293 cells were maintained in DMEM (Invitrogen) at 37 °C and 5% CO_2 and transfected with the above-mentioned plasmids and two helper plasmids in OptiMEM (Invitrogen) and PEI (1 mg/mL, Polysciences). The supernatant was collected 48 hours after transfection and the resulting lentivirus preparation was concentrated using Lenti-X™ Concentrator (Clontech) according to the manufacturer's instructions. Progenitor cells were transduced with the concentrated lentiviral preparations by spin infection (1500 g, 1 hour) with 8 µg/mL Polybrene. Cells expressing the virus insertion were sorted in a Sony SH800 SFP cell sorter (sorting chip: 100 µm) for mCherry or GFP expression before DC differentiation.

CRISPR-Cas9 Ribonucleoprotein electroporation for generation Talin 1 knock-out precursor cells

Synthetic guide RNAs (crRNAs)[42] were designed using the Horizon Discovery online tool (https://horizondiscovery.com/en/ordering-and-calculation-tools/crispr-guide-rna-designer),

targeting the exon 25 of the mouse gene encoding Talin 1 (Tln1). crRNA sequences: Talin 1 control (Ctrl): Non-targeting control #1 (Horizon Discovery); Talin 1 knock-out (*Tln1*$^{-/-}$): s(5′–3′) CTCACTGTTTCCCCGGGTA[18]. Precursor cells were generated following manufacture's instructions. Briefly, 1x106 precursor cells were spun down, washed with PBS and resuspended in 100 µL of OptiMEM (Invitrogen). A mix of tracrRNA, crRNA and Cas9 (all Horizon Discovery) was added to the cell suspension and transferred to an electroporation cuvette. The mixture was electroporated using a specifically designed protocol (program A30) with an Amaxa nucleofector (Lonza) and promptly transferred to a well-plate pre-warmed at 37 °C and 5% CO2. Cells were further incubated for 72 hours before single cell sorted with a Sony SH800 SFP cell sorter (sorting chip: 100 µm). Single cell clones were tested as described before[43] and further confirmed by sequencing of the region of interest.

Purification and maintenance of T cell

T cells were isolated from the spleens *C57BL/6J, LifeAct-eGFP* mice using an EasySep Mouse T cell Isolation Kit (STEMCELL Technologies, 19851) according to the manufacturer's instructions. Isolated T cells were plated on cell-culture wells coated with anti-CD3e and anti-CD28 antibodies (1 µg/mL, Invitrogen, 16-0031-82, RRID:AB_468847 and 16-0281-82, RRID:AB_468921) for 2 days in R10 medium supplemented with interleukin-2 (IL-2) (10 ng/mL; R&D Systems). Activated T-cells were collected and expanded in IL-2 containing R10. Activated T cells were kept at 37 °C and 5% CO_2 for a maximum of one week.

Differentiation and maturation of DCs

DCs, with exception of *Tln1*$^{+/+}$and *Tln1*$^{-/-}$ DCs, were differentiated by seeding 3x10^5 precursor cells in a 10 mL dish containing R10 medium supplemented with 10% of in-house-generated granulocyte-macrophage colony-stimulating factor (GM-CSF) hybridoma supernatant. On the third day of differentiation, 10 mL of R10 medium containing 20% GM-CSF was added to each dish. Half of the medium was replaced with R10 medium containing 20% GM-CSF on day 6 and cells were either harvested for maturation or frozen on day 8.
Tln1$^{+/+}$and *Tln1*$^{-/-}$ DCs were differentiated by seeding 1x10^5 and 3x10^5 precursor cells, respectively, in a 10 mL dish containing R10 medium supplemented with 10% of in-house-generated granulocyte-macrophage colony-stimulating factor (GM-CSF) hybridoma supernatant and 1% of in-house-generated Flt3l containing supernatant. On the third day of differentiation, all medium was removed and 20 mL of R10 medium containing 20% GM-CSF

was added to each dish. On day 6, medium was replaced as described above and cells were frozen or harvested for maturation on day 8.
Maturation of all DCs was induced by overnight stimulation with lipopolysaccharide (LPS) from *Escherichia coli* 0127:B8 (Sigma) at a final concentration of 200 ng/mL.

Enucleation of mature DCs

Enucleation of mature DCs was performed as described previously[44]. Briefly, from a 50% (vol/vol) solution Ficoll-400 (Fisher scientific), prepared with phosphate-buffered saline (PBS), a 30% (vol/vol) stock solution was made with D10 (DMEM supplemented with 10% FBS and 100ul/ml Pen-strep, all Invitrogen). The stock solution was filtered with a 0.4 PES filter and diluted using D10 supplemented with cytochalasin B (10 mg/mL) (Tocris) and DMSO (0.2%), to the final concentrations of: 20%, 18%, and 15%. 2 ml of each of these solutions were layered into an ultracentrifuge tube (13.2 mL thin wall, Thermofisher scientific) from the most to the least concentrated. The tube was covered and the gradient was incubated at 37 °C overnight. Next day, 1-2x10^7matured DCs resuspended in 1 mL of pre-warmed 15% Ficoll were added on top of the gradient. The tube was filled with D10 medium containing cytochalasin (10mg/ml) and loaded into a pre-warmed (31 °C) SW641 rotor of a Sorval wx100 (Thermos Scientific). Cells were centrifuged for 1 hour at 27000rmp (started with acceleration of 9 and stopped with deceleration of 1). After centrifugation, cells were extracted and washed three times with PBS (5 minutes, 300g). Cells were then resuspended in 1 mL of R10 medium, labeled with NucBlue (Life tech.) and incubated at 37 °C and 5% CO_2 for at least 30 minutes before usage.

Flow Cytometry analysis of DCs

DCs were routinely checked for correct surface expression markers using antiboides against MHCII and CD11c (48-5321-82 and 17-0114-82, respectively, both eBiosciences). Stainings were performed in FACS buffer (1xPBS, 2 mM EDTA, 1% BSA) with Fc receptor blockage (anti-mouse CD16/CD32, BioLegend). Analysis was carried either on a FACSCanto BD Biosciences or in a BC CytoFLEX LX.

Transient transfection of DCs

The following plasmids were used: eGFP, pcDNA3-EGFPCdc42(wt), and pcDNA3-EGFP-Cdc42(T17N)[45] (gifts from Klaus Hahn to Addgene, plasmids #12599 and #12601). DCs

derived from progenitor cells were transfected with 4 μg of DNA using the nucleofector kit for primary T cells (Amaxa, Lonza Group) following the manufacturer's guidelines. Briefly, 4-5x10^6 cells were resuspended in 100 μL of DMEM (Invitrogen) and 4 μg of plasmid DNA. Cells were transferred to a cuvette and electroporated using a specifically designed protocol (program X-001). Transfected DCs were incubated overnight in R10 supplemented with 10% GM-CSF and LPS (200 ng/mL). Experiments were carried out the next day, and only GFP-expressing cells were analyzed.

Pharmacological Inhibitors

The following small molecule inhibitors were used: ZCL278[46] (MedChemExpress) and ML141[47] (Sigma) to perturb Cdc42 activity; and NSC23766 (MedChemExpress) to perturb Rac1 activity[48]. Inhibitors were diluted in DMSO, mixed with the DC suspension after maturation for at least 30 minutes and kept through the assays at the indicated final concentration. ZCL278, 10 μM; ML141, 20 μM; NSC23766, 50 μM.

FACS F-actin analysis in DCs

After overnight stimulation with LPS, wild-type and *Dock8*$^{-/-}$ DCs were recovered in 12-well plates in 500 μL R10 for 30 minutes at 37 °C. Cells were stained during fixation (4% PFA, 20 μM FITC-phalloidin and 0.5% saponin in phosphate-buffered saline (PBS), 500 μL, 20 minutes at 37 °C) and analyzed on a FACS Aria III. Stainings were carried out in three biologically independent samples.

Immunodetection of whole cell lysates

1.6 × 10^5 DCs were harvested and washed with PBS. The cell pellet was lysed using RIPA buffer (Cell Signaling), mixed in a 1:1 proportion with 2x Leammli buffer (Sigma) and incubated for 5 min at 90°C. Boiled samples were loaded on precast 3%–8% Tris-Acetate gel (Invitrogen) and ran in 1x Tris-Acetate running buffer. Resulting samples was transferred to a nitrocellulose membrane using the iBlot Dry Blotting System (Invitrogen) and blocked for 1 h with 5% powder milk in TBS containing 0.01% Tween-20. For whole-cell lysate protein detection, the following primary antibodies were used: mouse monoclonal anti-talin antibody (1:400 dilution, T3287, Sigma), and rabbit polyclonal HSPA1A (anti-HSP70) antibody (1:10 000 dilution, PA5-34772, ThermoFisher Scientific). Membranes were incubated with the primary antibody solutions overnight at 4 °C. After, membranes were washed and incubated with the secondary antibody solutions for 1 hour at room temperature. The following secondary antibodies were used: goat anti-mouse IgG (H/L):HRP (1:10 000 dilution, BioRad), and goat

anti-rabbit IgG (H/L):HRP (1:3 000 dilution, BioRad). Enzymatic reaction was started by addition of chemoluminescent substrate for HRP using Clarity Western ECL substrate and acquired on a ChemieDoc MP imaging system (all BioRad).

Adhesion assay

Wild-type, *Tln1*$^{+/+}$ and *Tln1*$^{-/-}$ DCs were matured with LPS as described above. Upon addition of LPS cells were seeded in a TPP 10 cm^2 round tissue culture plate (Sigma) and incubated at 37 °C and 5% CO_2 for 45 minutes. Low magnification images were acquired in an inverted DM IL Led Fluo Leica Microsystems microscope, using a 20x/0.3 NA air objective equipped with an iDS U3-36PxXCP-C camera. Cells were considered adherent based on their morphology.

Under-agarose migration assay of mature DCs

Glass coverslips were glued to the bottom of a petri dish with a 17 mm diameter hole where a custom-made plastic ring was attached using paraffin (Paraplast X-tra; Sigma). Agarose solution was prepared by mixing one part of 2x Hank's buffered salt solution (HBSS, Sigma), pH 7.3 with 2 parts RPMI (Invitrogen) supplemented with 20% FCS (Invitrogen) and 2x the concentration of all the other supplements used in R10 medium (see above) and either 2% or 4% of UltraPure Agarose (Invitrogen) dissolved in one part water to achieve different agarose stiffnesses. 400 µL of the liquid agarose was poured into the dish, covering the coverslip. The agarose was allowed to solidify at room temperature for 5 minutes, after which two holes (1.5 mm and 2.0 mm) were punched into the agarose. The dishes were incubated at 37 °C and 5% CO_2 for 30 minutes for equilibration. 2.5 µg/mL of CCL19 (PrepoTech) diluted in R10 was placed in the 2 mm hole and 0.5-1x10^6 mature DCs were placed in the 1.5 mm hole opposite to the chemokine. Before acquisition, dishes were incubated for at least 1 hour at 37°C and 5% CO_2 to allow invasion under the agarose. All images were acquired under physiological conditions using custom-built climate chambers (37 °C, 5% CO_2, humidified).

Passivation of coverslips using PLL-PEG

Glass coverslips (22x22 mm, FisherScientific) were sonicated in a solution of 70% ethanol and for at least 15 minutes. After sonication, coverslips were air dried glued to the bottom of a petri dish with a 17 mm diameter hole where a custom-made plastic ring was attached using paraffin

(Paraplast X-tra; Sigma). Coverslips were then covered with a solution of PLL-PEG (1 mg/mL, SuSoS Surface Technology) overnight at 4 °C. After incubation, coverslips were washed at least three times with PBS. Dishes were further assembled for the under-agarose assay as described above.

Immunofluorescence under-agarose

For analysis of fixed samples, a round-shaped coverslip (#1.5, 10 mm, Mentzel, Thermo Fisher Scientific) was placed in a glass-bottom dish before casting the agarose. DCs and chemokine were added to the dishes as described above. Cells were allowed to invade and migrate for at least 3 hours at 37 °C and 5% CO_2. Migrating cells were fixed with prewarmed PBS supplemented with 4% paraformaldehyde (PFA) for 20 minutes at 37 °C. After fixation, the agarose patch was carefully removed and the coverslip was recovered and thoroughly washed with PBS. Coverslips were incubated with 0.1% Triton X-100 in PBS for 20 minutes at room temperature, washed with PBS, and blocked with 1% Bovine Serum Albumin (BSA) for 1 hour at room temperature. Primary antibodies were diluted in PBS with 1%BSA and incubated either overnight at 4 °C or for 2 h at room temperature. After primary antibody incubation, cells were washed 3 times with PBS and incubated with secondary antibody diluted in PBS with 1% BSA 1 hour at room temperature. Stained coverslips were washed 3 times with PBS and mounted on a slide using Flourmount-G mounting medium with DAPI (00-4959-52, ThermoFisher Scientific). Slides were imaged the next day or stored at 4 °C in the dark until image acquisition. Confocal imaging of fixed samples was performed using an upright confocal microscope + Airyscan (LSM800, Zeiss) equipped with 2 GaAsP Photomultiplier Modules (PMTs) detectors using 40x/1.3 oil DIC, UV-IR objective. Multi-positions of Z-stacks (0.4µm step size) of fixed migrating cells were acquired using Zeiss software (ZEN 3.8).

Primary and Secondary Antibodies

Target	Primary Antibodies	Secondary Antibodies
MTOC	anti-γTubulin (abcam, ab11317, 1:400)	Goat anti-Rabbit IgG (H+L) Alexa Fluor™ 488 (Invitrogen, A-11008, 1:200)
Golgi complex	anti-Giantin (Sysy antibodies, 263003, 1:100)	
Lysosomes	anti-LAMP2 (abcam, ab13524, 1:100)	Donkey anti-Rat IgG (H+L) Alexa Fluor™ 488

		(Jackson Immuno Research, AB_2340686, 1:200)
F-actin	Alexa Flour™ 647 Phalloidin (Invitrogen, A22287, 1:400)	

2D analysis of cells migrating under-agarose

For 2D analysis of cells migrating under agarose, LifeAct-eGFP or actin-eGFP expressing DCs labeled with Hoechst (NucBlue™, Hoechst 33342, Invitrogen) were imaged with an inverted widefield Nikon TiE2 microscope equipped with either a 20x/0.75 DIC 1 air PFS or a 40x/0.95 NA DIC air PFS objectives using a DS-Qi2 CMOS monochrome camera and a Lumencor Spectra III light source (390/22 nm, 440/20 nm, 475/28 nm, 511/16 nm, 555/28 nm, 575/25 nm, 635/22 nm, 747/11 nm; Lumencor). Images were taken every 30 seconds at multi-positions using the NIS Elements software (Nikon Instruments).

Single cells moving under agarose and their central actin pool were segmented based on either the LifeAct-eGFP or the GFP-actin signal using Ilastik pixel classification[49] and tracked using Fiji - Trackmate[50]. Resulting tracks were manually curated and only non-interacting, well-isolated cells with tracks longer than 10 frames (5 minutes) were further processed. Cell speed was calculated for LifeAct-eGFP cells using their center of mass, based on the outline generated by the segmentation. Protrusion areas were defined by the GFP-actin signal and correspond to the non-overlapping regions of the cell segmentations at time t and t+1. All actin intensities are the integrated and background-corrected to the actin signal in the respective areas. Comparison of the temporal cross correlation of two parameters (central actin intensity, cell area, cell speed) and test for the statistical significance of the temporal offset we used cross-correlation analysis[51] with a custom-written MATLAB script (MATLAB, R2020a).

Total internal reflection (TIRF) microscopy of cells migrating under-agarose

TIRF imaging of DCs migrating under agarose was performed at 37 °C and 5% CO_2 using a Zeiss Axio Observer.Z1 inverted flourescence microscope equipped with a 63x/1.46 oil TIRF (WD 0.10 mm) objective, four fibre-coupled laser for TIRF (405 nm, 488 nm, 561 nm and 640 nm), and 2x photometric Evolve 512 EM-CCD cameras. Images were acquired every second for at least 10 minutes using VisiView software (Visitron). Resulting movies were further processed using Fiji/ImageJ.

Bead displacement in agarose

To track the force cells exert on the agarose, polystyrene microspheres with a nominal diameter of 1 μm and labeled with a fluorescent red dye (Red-580/605, F-13083 Invitrogen) were added to the agarose solution (1:100 dilution). The agarose cast and cell addition were performed as mentioned above.

Imaging of LifeAct-eGFP expressing DCs labeled with Hoescht (NucBlue™, Hoechst 33342, Invitrogen) was performed under physiological conditions using custom-built climate chambers (37 °C, 5% CO_2, humidified) on an inverted spinning-disc confocal microscope (Nikon CSU-W1) cameras using a 40x/1.15 water objective. Z-stacks (0.1 μm step size) of migrating cells were acquired using two teledyne photometric BSI (USB3) sCMOS cameras with 95% quantum efficiency and a 6.5x6.5 μm pixel area. Images were acquired every 30 seconds for approximately 20 minutes.

Bead displacement analysis was performed using custom Python scripts. First, beads were individually segmented and labeled using their maximum intensity projection in Z and time to discard non-stationary beads, and a size filter was used to exclude bead aggregates. Next, we defined a fixed volume around each bead spanning the whole z-stack and 5x5 pixels in XY. In order to track the movement in Z, we generated a time kymograph of the bead intensity projected along the x and y-axis and tracked the moving bead edge, detected using Otsu threshold method **(Extended Data Fig. 2a)**. We then computed the total actin and nuclear intensity in each time frame within a similar volume of 20x20 pixels in XY, centered around each bead. In order to classify the actin contribution between none, cytoplasmic and central actin, we run a K-means clustering algorithm with two (*Dock8*$^{-/-}$ DCs) or three (wild-type DCs) clusters on the actin intensity curves. Hoechst (blue) signal was used to classify the nuclear contribution to the displacement. We then computed the average position of the bead for each of the regions and subtracted it from the baseline (no cell).

Manufacturing and migration assay in polydimethylsiloxane (PDMS) Height Confiners

The microfabricated PMDS devices used to confined the cells in environments with different heights consist of two glass coverslips spaced by PDMS micropillars. One of the glass coverslips (#1.5, 22x22 mm, Mentzel, Thermo Fisher Scientific) was glued to a petri-dish with a 17 mm diameter hole using aquarium sealant, while the other, containing the PDMS micropillars, was attached to a PDMS cylinder which is secured by a magnetic device.

The pattern mold was produced by photolithography on a silicon wafer. The wafer was coated with SU8-GM1050 (Gersteltec) and soft-baked for 1 minute at 120 °C, followed by 5 minutes

at 95 °C. The wafer was developed in SU8 developer for 17 seconds and then silanized with trichloro(1H,1H,2H,2H-perfluorooctyl)silane in a vacuum desiccator for 1 hour.

To produce the PDMS piston, silicone elastomer and curing agent were mixed in a 30:1 ratio, degassed as described before, and poured into an aluminium mold with the required dimensions. The PDMS pistons were cured at 80 °C for 6 hours and peeled off the silicon wafer with isopropanol.

Micropillars were produced by mixing silicone elastomer and curing reagent (PDMS Sylgard 184 Elastomere Kit, Dow Corning) in a 7:1 ratio. The mixture was then degassed using a planetary centrifugal mixer (ARE250, Thinky) and carefully poured onto the wafer. Round coverslips (#1.5, 10 mm diameter, Mentzel, Thermo Fisher Scientific) were plasma activated for 2 minutes (Plasma Cleaner, Harrick Plasma) and placed on the wafer with the activated surface facing the elastomere/curing agent mixture. The wafer was cured on a heating plate for 15 minutes at 95 °C, and the micropillar-coated coverslips were removed with a sharp razor blade and isopropanol.

The confiner devices were assembled by mounting a micropillars-bearing coverslip onto the PDMS piston with the micropillars facing upward and stuck to the glass bottom of the magnetic device. R10 medium was added to the micropillars-bearing coverslip and the petri dish containing the second glass coverslip, and incubated at 37 °C and 5% CO_2 for at least 30 minutes to equilibrate. Matured DCs were resuspended in R10 with 2.5 µg/mL of CCL19 (PrepoTech) in a final volume of 20 µL and added to the micropillars. The PDMS piston with the micropillars and the cell mixture were then pressed onto the glass coverslip in the petri dish and sealed by a metal ring. Confined cells were incubated for at least 1 hour at 37 °C and 5% CO_2 before imaging.

Imaging was performed as described in “bead displacement under agarose”. Z-stacks (0.4 µm step size) of migrating cells were every 30 seconds for approximately 20 minutes.

Manufacturing and migration assays in PDMS Pillar mazes, straight and constricted channels

The microfabricated PDMS devices containing pillar forest, straight, or constricted channels consist of PDMS blocks (fabricated as above, but using a 1:10 elastomer to curing agent ratio) attached to one glass coverslip. The devices were then cut in small squares (approximately 1x1 cm^2) and attached to plasma-cleaned coverslips (#1.5, 22x22 mm, Thermo Fisher Scientific), and incubated at 85 °C for 1 hour.

The coverslips with the PDMS devices were then glued to a petri dish containing a 17mm diameter hole using aquarium sealant. Before adding the cells, devices were flushed and incubated with R10 medium for at least 1 hour at 37 °C and 5% CO_2. 0.5-1x10^6 matured DCs were added to one side of the devices and R10 with 2.5 µg/mL of CCL19 (PrepoTech) was added to the opposite side. Cells were incubated for at least 1 hour before image acquisition.

Analysis of the central actin pool intensity changes in cells moving in pillar mazes

Widefield images of LifeAct-eGFP expressing DCs moving in pillar mazes were acquired as described in "2D analysis of cells migrating under agarose". Images were taken every 30 seconds at multi-positions with NIS Elements software (Nikon Instruments).
Cell area and nucleus were segmented and tracked employing the Ilastik pixel classification/cell tracking workflows. Non-interacting, well-isolated cells were identified and stabilized to their center of mass. For each cell, all regions of interest were manually annotated. The F-actin intensity in these regions was normalized to the overall F-actin intensity. All retraction events were pooled by shifting the events relative to each other such that t=0 marks the beginning of the retraction event and by setting the intensity in all regions to 1.

Analysis of cells moving in straight and constricted channels

Imaging of EB3-mCherry and LifeAct-eGFP expressing DCs in straight and constricted channels was performed in an inverted widefield Nikon TiE-2 microscope equipped with 40x/0.95NA DIC air objective using a Nikon DS-Qi2 CMOS monochrome camera and a Lumencor Spectra III light source (390/22 nm, 440/20 nm, 475/28 nm, 511/16 nm, 555/28 nm, 575/25 nm, 635/22 nm, 747/11 nm; Lumencor). Images were taken every 60 seconds at multi-positions with NIS Elements software (Nikon Instruments).
Actin distribution in cells during constriction passage was quantified using custom scripts in Python. First, channels were segmented using the bright field images, and the actin signal was averaged vertically (y-axis, only in segmented areas) in order to create a longitudinal actin density profile for each time frame. A maximum projection of these profiles resulted in a final time-averaged actin density profile, which was used to compute the ratio between the actin signal inside and outside the constriction.

Collagen migration assay of mature DCs

Custom-made migration chambers were assembled using a petri-dish with a 17mm diameter hole in the middle which was covered by 2 glass coverslips[52] (#1.5, 22x22 mm, ThermoFisher Scientific).

The collagen mixture, consisting of either 1.5 or 3mg/mL bovine collagen I (PureCol, Nutragen; both AdvancedBioMAtrix), was reconstituted by mixing 1.5-3.0x10^5 matured DCs in suspension (R10 medium) with collagen I solution buffered to physiological pH with Minimum Essential Medium (Sigma) and sodium bicarbonate (Sigma) in a 1:2 ratio. In the experiments where labeled collagen was used, a mix of unlabeled and labeled collagen was used on a ratio of 1:2.

The collagen and cell mixture were then added to the migration chamber and allowed to polymerize in a vertical position for 1 hour at 37°C, 5% CO_2. Directional cell migration was induced by overlaying the polymerized gels with 0.63µg/mL CCL19 in R10. To prevent drying out of the gels, chambers were sealed with paraffin (Paraplast X-tra, Sigma).

Brightfield movies were acquired in inverted cell culture microscopes (DM IL Led, Leica Microsystems) using either a 10x/NA or a 40x/NA air objective equipped with cameras (ECO415MVGE, SVS-Vistek) and custom-built climate chambers (37 °C, 5% CO_2, humidified). Images were acquired with a time interval of either 30 or 60 seconds and global y-displacement was analyzed by a custom-made tracking tool.

Collagen fiber displacement and F-actin accumulation analysis

To visualize collagen fibers, collagen was directly conjugated to Alexa Fluor 594 NHS Ester (Succinimidyl Ester, ThermoFisher Scientific). Collagen was added to SnakeSkin Dialysis Tubes, 10K MWCO, 16 mm (ThermoFisher Scientific), and immersed in 100 mM NaHCO3 overnight at 4 °C to allow polymerization. Alexa Fluor 594 NHS Ester (1.5 mg/mL) was added to the polymerized collagen and incubated for 3 hours. To remove the unconjugated dye, the collagen mixture was placed in 0.2% acetic acid in deionized water for further dialysis overnight at 4 °C. Labeled collagen was kept at 4 °C until usage.

Movies of LifeAct-eGFP expressing DCs in Alexa-594-labeled collagen matrices were acquired on an inverted spinning-disc confocal microscope (Andor Dragonfly 505) using a 60x/1.4 NA objective and 488/561 nm laser lines in a custom-built climate chamber (37 °C under 5% CO_2). Z-stacks (1.5 µm step size) of migrating cells were recorded using an Andor Zyla camera (4.2 Megapixel sCMOS) every 60 seconds for 20 to 25 minutes.

Collagen fiber displacement was calculated using the software Davis 8 (Lavision) applying Particle Image Velocimetry (PIV) as described before[22]. Computation of the closest distance between a collagen fiber deformation maxima and an F-actin intensity maxima across multiple time-lapse images and z-slices was performed using a standardized Python function. Briefly, this function independently finds the local maxima of collagen fiber deformation or F-actin intensity within a predefined neighborhood radius and calculates the minimum distances between these two structures per Z-slice and time point.

Fixation and immunofluorescence of collagen matrices

To visualize the nucleus-MTOC orientation during migration in different collagen matrices Centrin-eGFP expressing DCs labeled with Hoechst (NucBlue™, Hoechst 33342, Invitrogen) were seeded in the collagen mixture and collagen gels were cast as described above. Three hours after the introduction of the CCL19 gradient, the collagen gels were isolated and immediately bathed in a PBS solution with 4% paraformaldehyde for 10 minutes at room temperature. The fixed collagen gels were washed with PBS at least three times and incubated with Phalloidin-Atto647N (1:400 dilution, Sigma) diluted in PBS supplemented with 0.2% BSA and 0.05% saponin for 2 hours at room temperature. After three more washes with PBS, the gels were mounted using Flourmount-G mounting medium with DAPI (00-4959-52, ThermoFisher Scientific).
Imaging was performed in an inverted confocal microscope (LSM800 inverted, Zeiss) equipped with 2 GaAsP PMTs detectors using a 40x/1.2 water objective. Multi-positions of Z-stacks (0.5 μm step size) of fixed cells migrating in the collagen matrices were acquired using Zeiss software (ZEN 3.8).

Statistics and reproducibility

Statistical details for each experiment can be found in the figure legends. Appropriate controls were performed for each biological replicate. All replicates were validated independently and pooled only when all showed the same trend. Statistical analysis was conducted in Prism10.2.2 (GraphPad). Data was tested for normal distribution using the D'Agostino Pearson Omnibus k2 test. Normally distributed data was tested using a student's t-test or ANOVA. Non-normally distributed data was tested using the Mann-Whitney test. Categorical data (e.g. presence/absence of the central actin pool) was tested using Fisher's exact test.

Data availability

Data sets generated during this study are available from the corresponding author on request.

Code availability

Script used to quantify proximity between collagen fibers displacement and actin bursts can be found here: https://github.com/mirifaj/actin_deformation_cell_migration. Scripts used to quantify bead displacement induced by DCs migrating under agarose can be found here: https://github.com/avesar/protrusion-forces. Scripts used for the correlative analysis between central actin pool and actin at the protrusions, cell area and cell speed can be found here: https://git.ista.ac.at/rhauschild/movingactincellseg
All custom-made scripts are available from the authors on request.

References

34. Riedl, J. *et al.* Lifeact mice for studying F-actin dynamics. *Nat. Methods* **7**, 168–169 (2010).
35. Redecke, V. *et al.* Hematopoietic progenitor cell lines with myeloid and lymphoid potential. *Nat. Methods* **10**, 795–803 (2013).
36. Leithner, A. *et al.* Fast and efficient genetic engineering of hematopoietic precursor cells for the study of dendritic cell migration. *Eur. J. Immunol.* **48**, 1074–1077 (2018).
37. Piel, M., Meyer, P., Khodjakov, A., Rieder, C. L. & Bornens, M. The respective contributions of the mother and daughter centrioles to centrosome activity and behavior in vertebrate cells. *J. Cell Biol.* **149**, 317–330 (2000).
38. Benesch, S. *et al.* Phosphatidylinositol 4,5-Biphosphate (PIP2)-induced Vesicle Movement Depends on N-WASP and Involves Nck, WIP, and Grb2. *J. Biol. Chem.* **277**, 37771–37776 (2002).
39. Riedl, J. *et al.* Lifeact: a versatile marker to visualize F-actin. *Nat. Methods* **5**, 605–607 (2008).
40. Kopf, A. *et al.* Microtubules control cellular shape and coherence in amoeboid migrating cells. *J. Cell Biol.* **219**, e201907154 (2020).

41. Rizzo, M. A., Davidson, M. W. & Piston, D. W. Fluorescent Protein Tracking and Detection: Fluorescent Protein Structure and Color Variants. *Cold Spring Harb. Protoc.* **2009**, pdb.top63 (2009).
42. Jinek, M. *et al.* A Programmable Dual-RNA–Guided DNA Endonuclease in Adaptive Bacterial Immunity. *Science* **337**, 816–821 (2012).
43. Mashal, R. D., Koontz, J. & Sklar, J. Detection of mutations by cleavage of DNA heteroduplexes with bacteriophage resolvases. *Nat. Genet.* **9**, 177–183 (1995).
44. Graham, D. M. *et al.* Enucleated cells reveal differential roles of the nucleus in cell migration, polarity, and mechanotransduction. *J. Cell Biol.* **217**, 895–914 (2018).
45. Nalbant, P., Hodgson, L., Kraynov, V., Toutchkine, A. & Hahn, K. M. Activation of Endogenous Cdc42 Visualized in Living Cells. *Science* **305**, 1615–1619 (2004).
46. Small molecule targeting Cdc42–intersectin interaction disrupts Golgi organization and suppresses cell motility. https://www.pnas.org/doi/10.1073/pnas.1116051110 doi:10.1073/pnas.1116051110.
47. Hong, L. *et al.* Characterization of a Cdc42 Protein Inhibitor and Its Use as a Molecular Probe. *J. Biol. Chem.* **288**, 8531–8543 (2013).
48. Gao, Y., Dickerson, J. B., Guo, F., Zheng, J. & Zheng, Y. Rational design and characterization of a Rac GTPase-specific small molecule inhibitor. *Proc. Natl. Acad. Sci.* **101**, 7618–7623 (2004).
49. Berg, S. *et al.* ilastik: interactive machine learning for (bio)image analysis. *Nat. Methods* **16**, 1226–1232 (2019).
50. Tinevez, J.-Y. *et al.* TrackMate: An open and extensible platform for single-particle tracking. *Methods* **115**, 80–90 (2017).
51. Mueller, J. *et al.* Load Adaptation of Lamellipodial Actin Networks. *Cell* **171**, 188-200.e16 (2017).

52. Sixt, M. & Lämmermann, T. In Vitro Analysis of Chemotactic Leukocyte Migration in 3D Environments. in *Cell Migration: Developmental Methods and Protocols* (eds. Wells, C. M. & Parsons, M.) 149–165 (Humana Press, Totowa, NJ, 2011). doi:10.1007/978-1-61779-207-6_11.

Figure 1

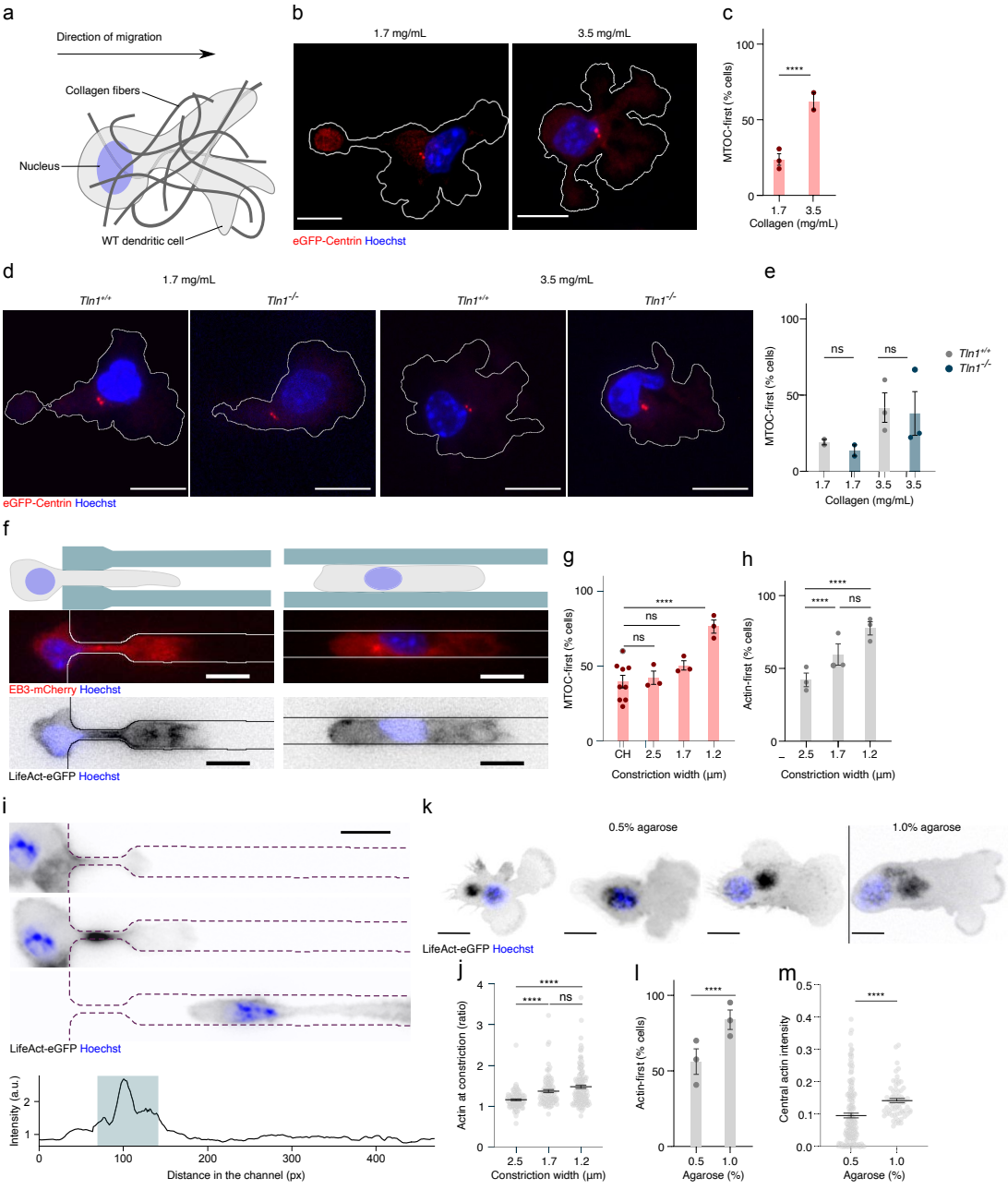
a
Direction of migration
Collagen fibers
Nucleus
WT dendritic cell
b
1.7 mg/mL
3.5 mg/mL
eGFP-Centrin Hoechst
c
MTOC-first (% cells)
Collagen (mg/mL)
d
1.7 mg/mL
3.5 mg/mL
Tln1+/+
Tln1-/-
eGFP-Centrin Hoechst
e
MTOC-first (% cells)
ns
Collagen (mg/mL)
f
EB3-mCherry Hoechst
LifeAct-eGFP Hoechst
g
MTOC-first (% cells)
Constriction width (µm)
h
Actin-first (% cells)
Constriction width (µm)
i
LifeAct-eGFP Hoechst
Intensity (a.u.)
Distance in the channel (px)
k
0.5% agarose
1.0% agarose
LifeAct-eGFP Hoechst
j
Actin at constriction (ratio)
Constriction width (µm)
l
Actin-first (% cells)
Agarose (%)
m
Central actin intensity
Agarose (%)

Figure 2

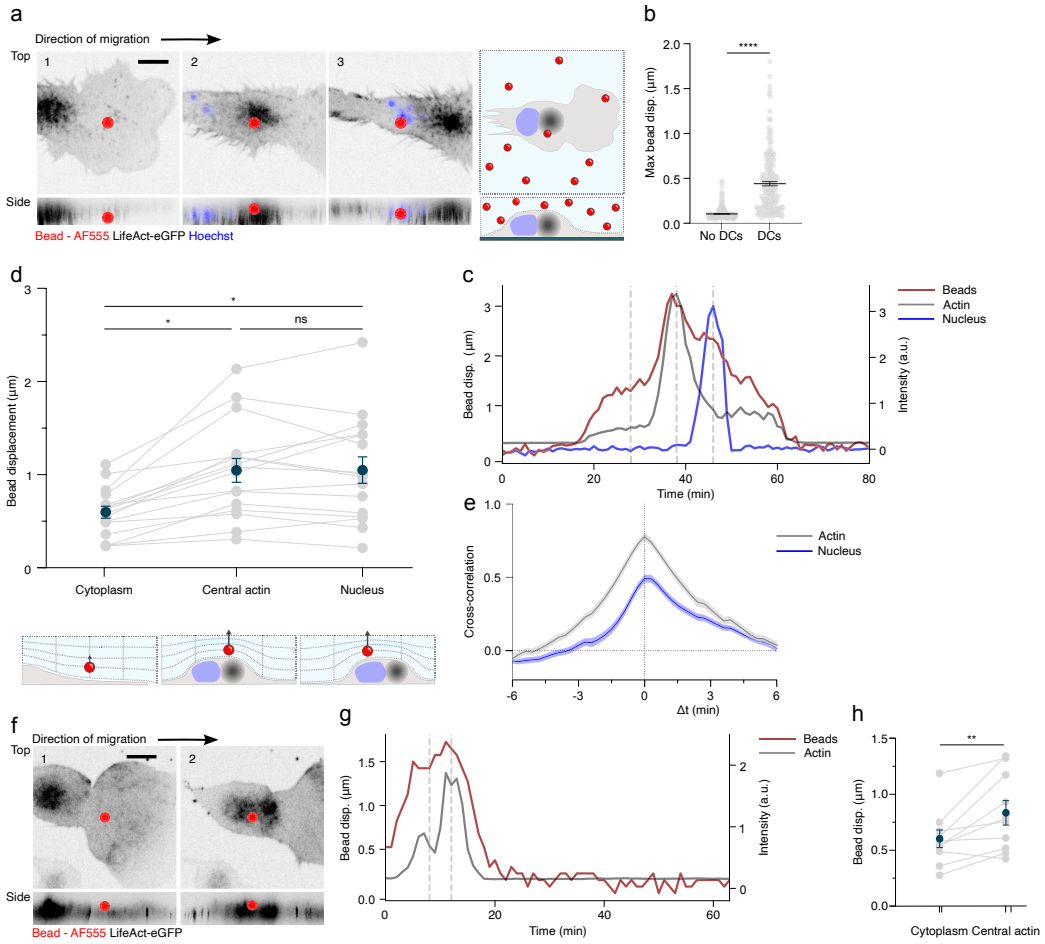
a
Direction of migration
Top
Side
1
2
3
Bead - AF555 LifeAct-eGFP Hoechst
b
Max bead disp. (µm)
****
No DCs
DCs
d
Bead displacement (µm)
*
*
ns
Cytoplasm
Central actin
Nucleus
c
Bead disp. (µm)
Intensity (a.u.)
Time (min)
Beads
Actin
Nucleus
e
Cross-correlation
Δt (min)
Actin
Nucleus
f
Direction of migration
Top
Side
Bead - AF555 LifeAct-eGFP
g
Bead disp. (µm)
Intensity (a.u.)
Time (min)
Beads
Actin
h
Bead disp. (µm)
**
Cytoplasm Central actin

Figure 3

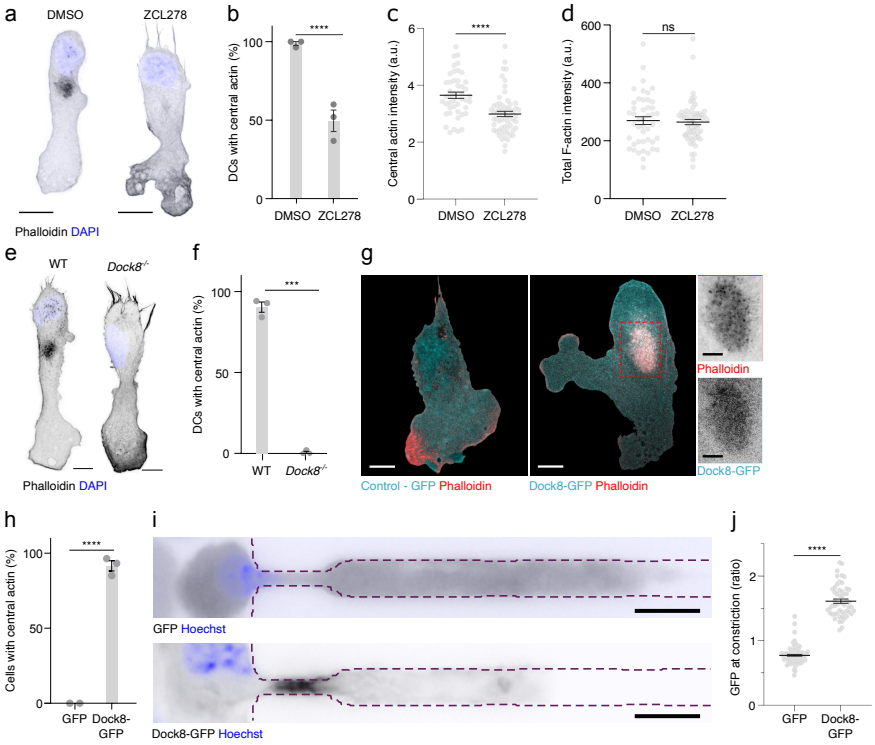
a
DMSO
ZCL278
Phalloidin DAPI
b
DCs with central actin (%)
****
DMSO ZCL278
c
Central actin intensity (a.u.)
****
DMSO ZCL278
d
Total F-actin intensity (a.u.)
ns
DMSO ZCL278
e
WT
Dock8-/-
Phalloidin DAPI
f
DCs with central actin (%)
***
WT Dock8-/-
g
Phalloidin
Dock8-GFP
Control - GFP Phalloidin
Dock8-GFP Phalloidin
h
Cells with central actin (%)
****
GFP Dock8-GFP
i
GFP Hoechst
Dock8-GFP Hoechst
j
GFP at constriction (ratio)
****
GFP Dock8-GFP

Figure 4

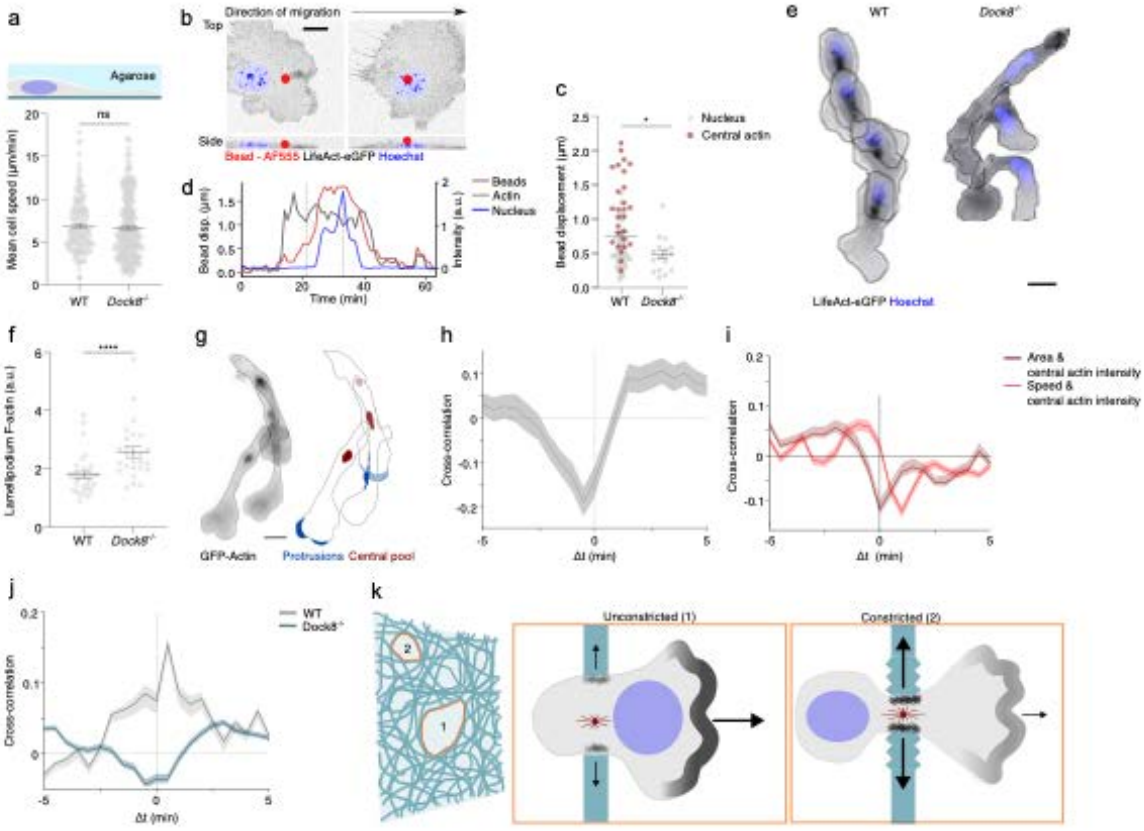
a
Agarose
ns
Mean cell speed (μm/min)
WT
Dock8-/-
b
Direction of migration
Top
Side
Bead - AF555 LifeAct-eGFP Hoechst
c
Nucleus
Central actin
Bead displacement (μm)
WT
Dock8-/-
d
Beads
Actin
Nucleus
Bead disp. (μm)
Intensity (a.u.)
Time (min)
e
WT
Dock8-/-
LifeAct-eGFP Hoechst
f
****
Lamellipodium F-actin (a.u.)
WT
Dock8-/-
g
GFP-Actin
Protrusions Central pool
h
Cross-correlation
Δt (min)
i
Area & central actin intensity
Speed & central actin intensity
Cross-correlation
Δt (min)
j
WT
Dock8-/-
Cross-correlation
Δt (min)
k
Unconstricted (1)
Constricted (2)
2
1

Figure 5

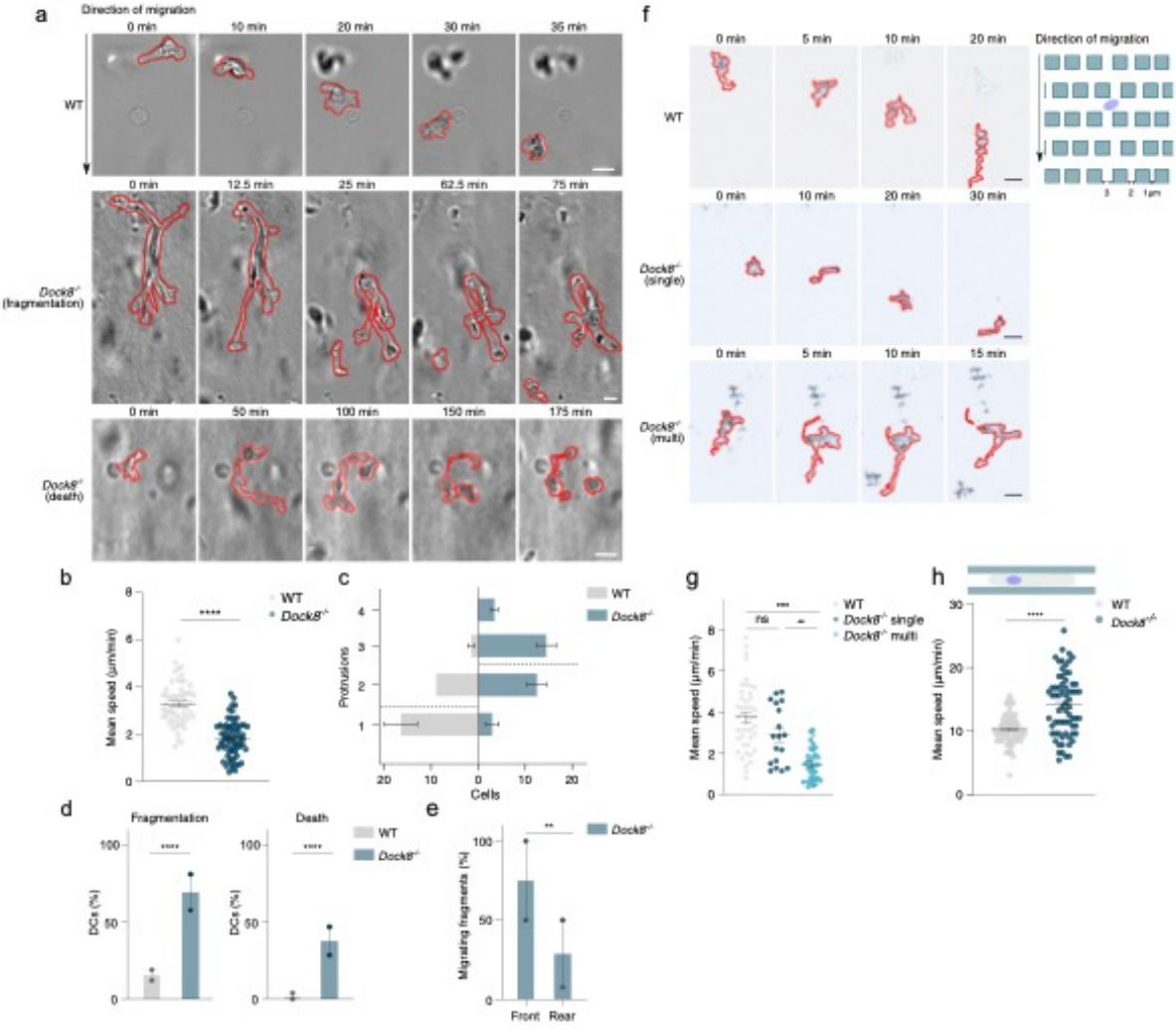
a
Direction of migration
0 min
10 min
20 min
30 min
35 min
WT
0 min
12.5 min
25 min
62.5 min
75 min
Dock8-/- (fragmentation)
0 min
50 min
100 min
150 min
175 min
Dock8-/- (death)
f
0 min
5 min
10 min
20 min
Direction of migration
WT
0 min
10 min
20 min
30 min
Dock8-/- (single)
0 min
5 min
10 min
15 min
Dock8-/- (multi)
b
Mean speed (μm/min)
****
WT
Dock8-/-
c
Protrusions
Cells
WT
Dock8-/-
d
Fragmentation
Death
DCs (%)
****
WT
Dock8-/-
e
Migrating fragments (%)
**
Dock8-/-
Front
Rear
g
Mean speed (μm/min)
***
ns
WT
Dock8-/- single
Dock8-/- multi
h
Mean speed (μm/min)
****
WT
Dock8-/-

Extended Data Figure 1 - Related to Figure 1

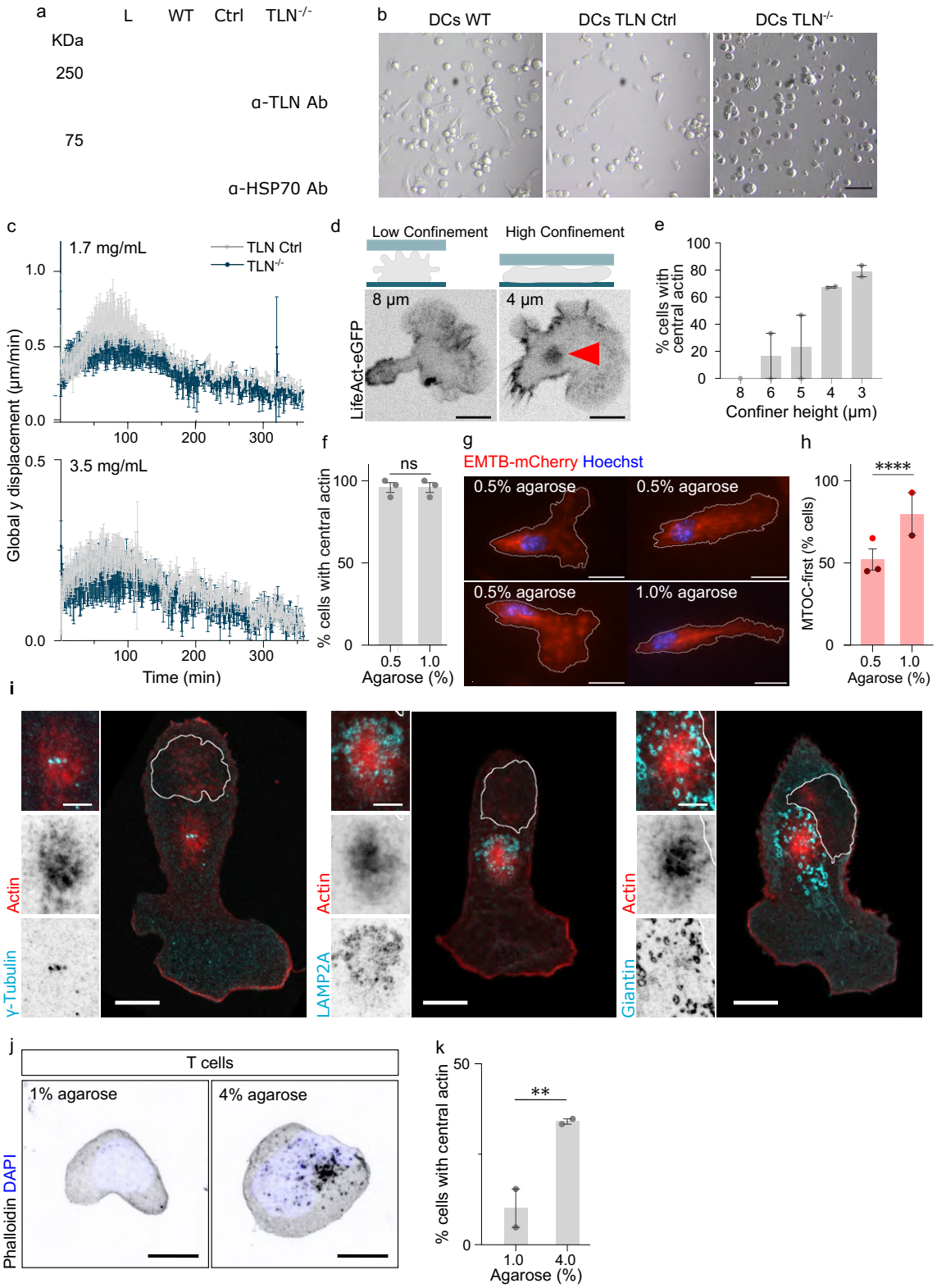

Extended Data Figure 2 - Related to Figure 2

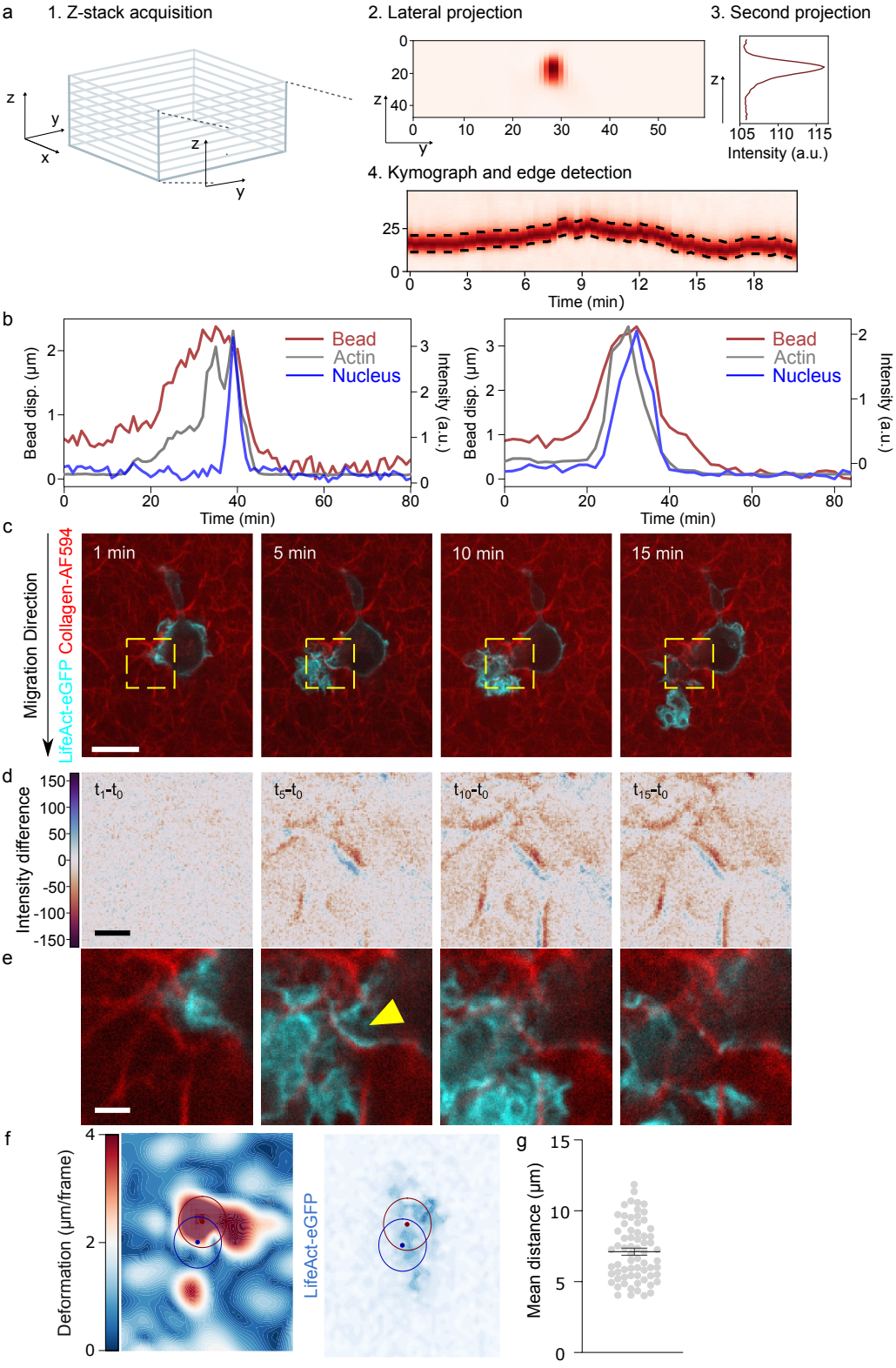

Extended Data Figure 3 - related to Figure 3

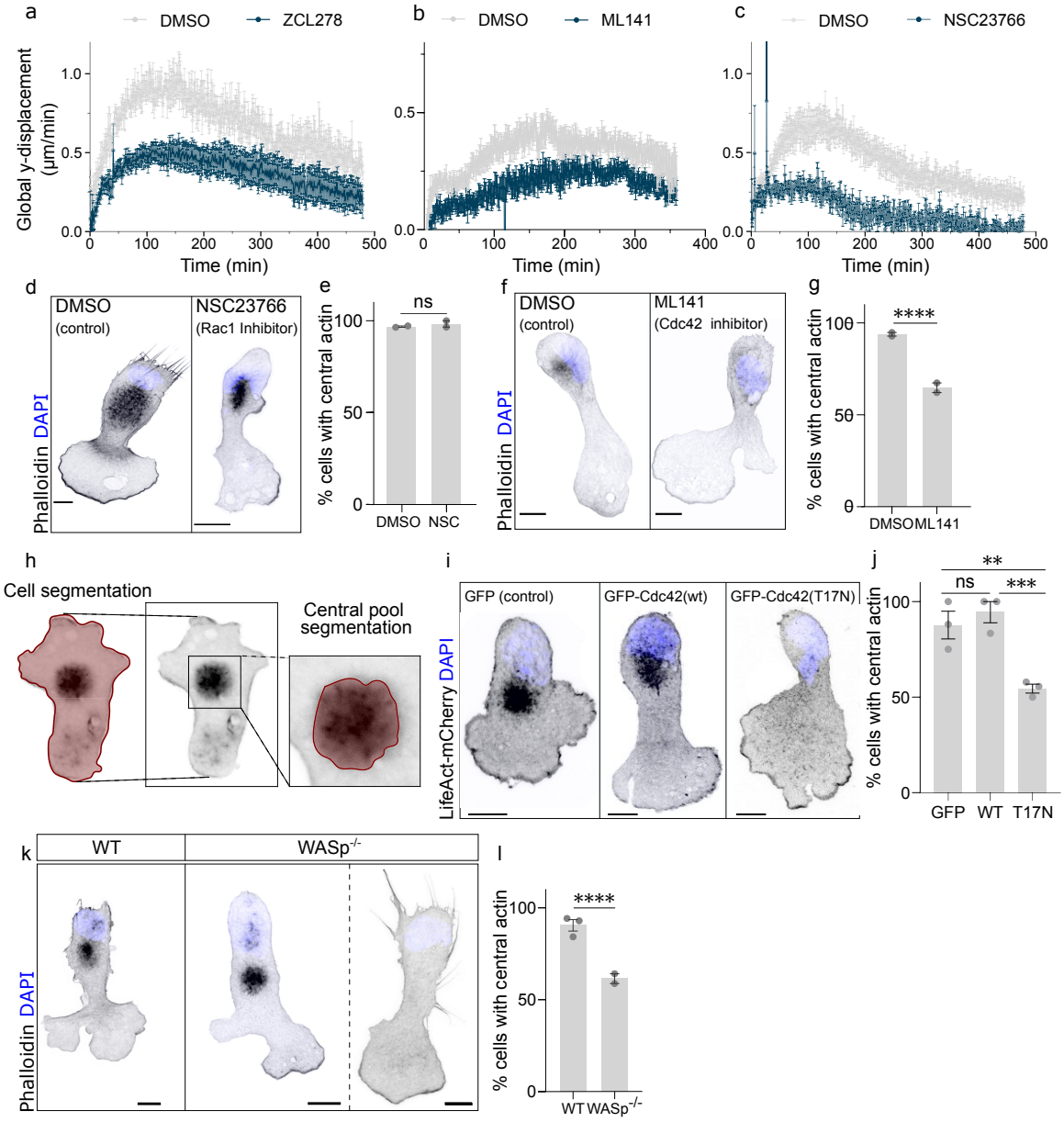

Extended Data Figure 4 - related to Figure 4

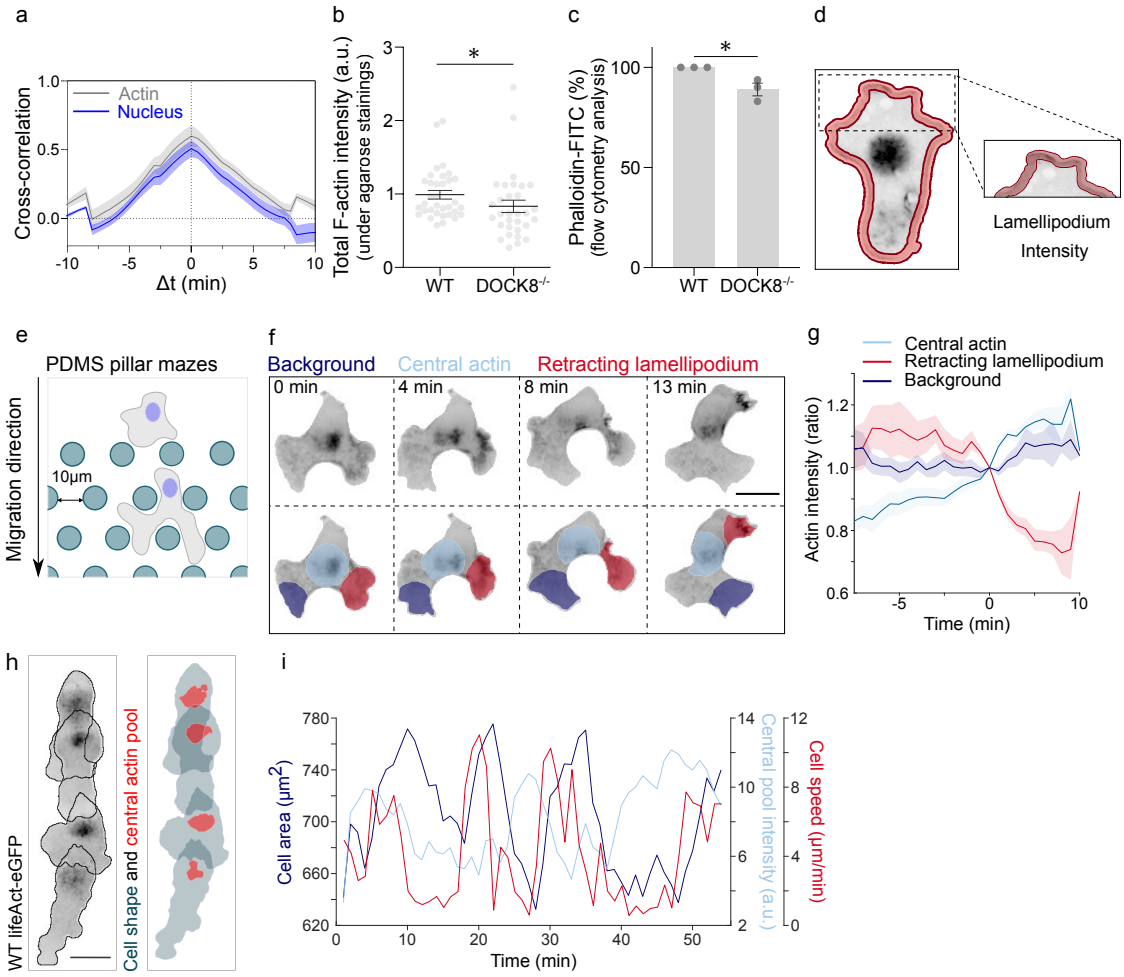

Extended Data Figure 1 - related to Figure 1 a. Talin 1 and HSP70 detection by Western Blot in wild-type, *Tln 1*$^{+/+}$ and *Tln1*$^{-/-}$ DCs. **b.** Wild-type, *Tln 1*$^{+/+}$ and *Tln1*$^{-/-}$ DCs in culture dishes 45 min after treatment with lypopolysaccharide (LPS). **c.** Dots show mean global y-displacement *Tln 1*$^{+/+}$ (grey) and *Tln1*$^{-/-}$ (blue) DCs migrating in 1.7 mg/mL (top) and 3.5 mg/mL (bottom) collagen gels, in three independent experiments. **d.** LifeAct-eGFP^{+} (actin, black) DCs migrating in 8 μm (left) and 4 μm (right) vertical PDMS confiners. Actin accumulation in higher confinement is shown by the red arrow. **e.** Dots show percentage of LifeAct-eGFP^{+} DCs showing the central actin pool in vertical confiners with heights from 8 μm to 3 μm. 8 μm, n=10; 6 μm, n=63; 5 μm, n=17; 4 μm, n=67; 3 μm, n=14. **f.** Dots show percentage of Wild-type DCs showing a central actin pool during migration under 0.5% or 1.0% in three independent experiments. 0.5% agarose, n=145; 1.0% agarose, n=88. P =0.4306. **g.** EMTB-mCherry+ (MTOC, red) DCs labeled with Hoechst (nucleus, blue) migrating under 0.5% and 1% agarose. **h.** Dots show percentage of EMTB-mCherry^{+} (dark red) or eGFP-Centrin^{+} (red) DCs showing MTOC-first orientation when migrating under 0.5% or 1% agarose in at least two independent experiments. 0.5% agarose, n=200; 1% agarose, n=74. **** P<0.0001. **h.** Wild-type DCs migrating under 1.0% agarose and stained with Phalloidin (F-actin, red) and antibodies specific for γ-Tubulin (MTOC - cyan, left), LAMP2 (Lysosomes – cyan, middle) or Giantin (Golgi complex - cyan, right). Nucleus position is shown by the white overlay. **i.** Primary T cells migrating under 1.0% and 4.0% agarose fixed and stained with phalloidin (F-actin, black) and DAPI (nucleus, blue). **j.** Dots show percentage of primary T cells with a central pool of actin under 1.0% and 4.0% agarose in two independent experiments. 1.0% agarose, n= 34; 4.0% agarose, n=69. ** P=0.0044. Histogram bars (**e, f, h, k**) are mean +/- s.e.m. Error bars in **(c)** are s.e.m. Two-sided Fisher's exact test is used in (**f, h, k**). Scale bars in **(d, h, i)** are 10 μm, 3 μm in the inset in **(h)**, and 20 μm in **(g)**. n indicates number of cells.

Extended Data Figure 2 - related to Figure 2 a. Workflow implemented for the quantification of bead displacement. (1) Z-stacks acquisition of fluorescent beads embedded in agarose; (2) lateral projection of the resultant Z-stack; (3) intensity projection of the generated lateral projection; and (4) kymograph and bead edge detection. **b.** Change in bead displacement in Z (red) or LifeAct-eGFP (actin, grey) and Hoechst (nucleus, blue) intensities over time for two different cells. **c.** One Z-plane of a LifeAct-eGFP^{+} (actin, cyan) DCs migrating in 3.5 mg/mL collagen matrices labelled with AlexaFlour594 (red). Yellow dashed box shows the area for the insets in

(c) and **(d)**. **d.** Image subtraction of different time-points of the collagen fibers in the area highlighted by the yellow box in **(b)** shows fiber displacement over time. Red: fiber position in the initial time point; blue: same fiber in the final time point; white: no changes in fiber position. **e.** Collagen fibers and actin in the area highlighted by the yellow box in **(b)** as in **(b)**. Yellow arrow shows actin accumulation at the place of collagen fiber deformation. **f.** Example of the workflow used for the quantification of the distance between collagen fiber displacement and actin accumulation. Left: Collagen fiber deformation measured by Particle Image Velocimetry (PIV). Dark red shows high deformation while dark blue no deformation areas. Right: LifeAct-eGFP intensity. Dark red dot shows the maximum deformation observed in collagen fibers and dark blue dot the maximum LifeaAct-eGFP intensity. **g.** Dots show mean distances between maximum collagen fiber deformation and maximum actin spots as in **(e)** in three independent experiments. n= 10 cells. Error bars show s.e.m. Scale bars in **(d, e)** are 2 μm and 10 μm in **(c)**

Extended Data Figure 3 - related to Figure 3 a. Dots show mean global y-displacement (speed) of wild-type DCs treated with DMSO (gray) or ZCL278 (blue) migrating in 1.7 mg/mL collagen gels in three independent experiments. n=6. **b.** Dots show mean global y-displacement (speed) of wild-type DCs treated with DMSO (gray) or ML141 (blue) as in **(a)**. n=6. **c.** Dots show mean global y-displacement (speed) of wild-type DCs treated with DMSO (gray) or NSC23766 (blue) as in **(a)**. n=6. **d.** Wild-type DCs migrating treated with DMSO (left) or NSC23766 (right) migrating under a patch of 1.0% agarose fixed and stained with phalloidin (F-actin, black) and DAPI (nucleus, blue). **e.** Dots show percentages of DMSO or NSC23766 treated DCs showing a central actin pool, in two independent experiments. DMSO, n=90; NSC, n= 68. ns P>0.9999. **f.** Wild-type DCs treated with DMSO (left) or ML141 (right) as in **(d)**. **g.** Dots show percentages of DMSO or ML141 treated DCs as in **(e)** in two independent experiments. DMSO, n=66; ML141, n= 78. **** P>0.0001. **h.** Central actin pool was segmented based on its phalloidin intensity (left). Mean values obtained in the central actin pool region were normalized to overall F-actin intensity in the cell (right). **i.** Wild-type DCs expressing GFP, $Cdc42^{WT}$-GFP or $Cdc42^{T17N}$-GFP as in **(d)**. **j.** Dots show percentage of GFP^{+}, $Cdc42^{WT}$-GFP^{+} or $Cdc42^{T17N}$-GFP^{+} DCs as in **(e)** in three independent experiments. GFP, n= 32; WT, n=27; T17N, n=52. ns P=0.6780, ** P= 0.0018, *** P= 0.0004. **k.** Wild-type and *Wasp*$^{-/-}$ DCs as in **(d)**. **l.** Dots show percentage of wild-type and *Wasp*$^{-/-}$ DCs as in **(e)** in two independent experiments. WT, n=240; *Wasp*$^{-/-}$, n=149. ****

P<0.0001. Histogram bars (**e, g, j, l**) are mean +/- s.e.m. and **e**rror bars in **(a, b, c)** show the s.e.m. Two-sided Fisher's exact test is used in (**e, g, j, l**). Scale bars in (**d, f, i, k**) are 10 μm. n indicates number of movies in **(a, b, c)** and number of cells in **(e, g, j, l)**.

Supplementary Figure 4 - related to Figure 4 a. Temporal cross-correlation between bead displacement and nucleus (blue) or actin intensity (grey) in *Dock8*$^{-/-}$ DCs migrating under agarose mixed with fluorescent beads. n=17 **b.** Dots show mean total F-actin intensity (phalloidin) of wild-type and *Dock8*$^{-/-}$ fixed DCs migrating under 1.0% agarose in three independent experiments. WT, n=34; *Dock8*$^{-/-}$, n=26. * P<0.05 Two-tailed paired t-test. **c.** Dots show normalized total F-actin (phalloidin-FITC) intensity accessed by flow cytometry of wild-type and *Dock8*$^{-/-}$ DCs in three independent experiments. * P=0.03808. Two-sided Fisher's exact test **d.** Scheme showing cell segmentation for quantification of lamellipodial actin. **e.** Scheme showing DCs migrating in a PDMS pillar maze. Cells were confined between 6 μm apart surfaces intersected by 10 μm distanced pillars. **f.** Top: Time-lapse images of a LifeAct-eGFP^{+} (actin, black) DC migrating in a pillar maze as shown in **(e)**. Bottom: Regions used for quantification of the retracting lamellipodium (red), central actin pool (light blue), and an area where no significant changes in actin intensity was observed - background (dark blue). **g.** Normalized mean actin intensity (LifeAct-eGFP) in the central pool (light blue), the retracting lamellipodium (red), and background (dark blue) through time. n=24. **h.** Left: Time-lapse projection of a migrating LifeAct-eGFP^{+} (actin, black) DC. Black line shows cell contour. Right: DC shape (blue) and central actin pool (red) segmentation results. **i.** Cell area (dark blue), central actin pool intensity (light blue) and cell speed (red) changes of a single DC migrating under 1.0% agarose over time. Histogram bars (**c**) are mean +/- s.e.m., error bars in **(b)** show the s.e.m and s.d. in **(g)**. Scale bars in (**f, h**) are 15 μm. n indicates number of cells.

Supplementary Videos Legends

Supplementary Video 1: *Tln1*$^{+/+}$ and *Tln1*$^{-/-}$ *DCs***s show no migration impairment in collagen matrices**. Bright field movies of *Tln1*$^{+/+}$ 1 (left) and *Tln1*$^{-/-}$ (right) migrating in 1.7 mg/mL (top) and 3.5 mg/mL (bottom) collagen matrices.

Supplementary Video 2: Confinement induces organelle re-orientation and polymerization of a central actin pool in migrating DCs. *First part:* Epifluorescence movies of EB3-mCherry^{+} (red, MTOC) and LifeAct-eGFP^{+} (black, actin) DCs, labeled with Hoechst (blue, nucleus) migrating in PDMS channels with a narrow constriction (1.7 µm) at the entrance. *Second part:* LifeAct-eGFP^{+} (black, actin) DCs migrating in confiners of different heights: 8 µm (top) and 4 µm (bottom).

Supplementary Video 3: Adhesions are not required for the formation of the central actin pool in DCs. *First part:* TIRF imaging of Vasp-GFP^{+} (cyan, VASP) and LifeAct-mCherry^{+} (red, actin) DCs migrating under agarose. Left panel, merged; middle panel, LifeAct-mCherry channel only; right panel: Vasp-GFP channel only. The red arrow highlights the central actin pool, while the cyan arrow points to the presence of VASP-GFP at the lamellipodium. *Second part:* TIRF imaging of two different LifeAct-eGFP^{+} DCs (black, actin) migrating under agarose on a coverslip coated with PEG. Note that, even though cells are slipping on the coverslip (proving the inability to adhere to the substrate) there is a distinct formation of a central actin pool as indicated by the red arrows. *Third part:* TIRF imaging of *Tln1*$^{-/-}$ LifeAct-eGFP^{+} DCs (black, actin) migrating under agarose on an uncoated coverslip.

Supplementary Video 4: Migration under soft substrates also induces organelle re-orientation and central actin pool polymerization. *First part:* EMTB-mCherry^{+} (red, MTOC) DCs migrating under soft (0.5%) or stiff (1%) agarose. Scale bar, 20 µm. *Second part:* LifeAct-eGFP^{+} DCs (black, actin) migrating under soft (0.5%) or stiff (1%) agarose.

Supplementary Video 5: Primary T cells also show a central actin pool. LifeAct-eGFP^{+} (black, actin) T cells labeled with Hoechst (blue) migrating under 1% (left) and 4% (right) agarose.

Supplementary Video 6: The central actin pool induces substrate deformations. *First part:* LifeAct-eGFP^{+} (black, actin) DCs labeled with Hoechst (blue, nucleus) migrating under agarose with beads labelled with AF-555 (red). *Second part:* Lateral projection of the cell shown before. Scale bar, 2 μm. *Third part:* LifeAct-eGFP^{+} (black, actin) enucleated DCs labeled with Hoechst (blue, nucleus) migrating under agarose with beads labelled with AF-555 (red). *Fourth part:* Lateral projection of the cell shown before. Scale bar, 2 μm.

Supplementary Video 7: Local collagen fiber displacement is associated with actin bursts. *First part:* LifeAct-eGFP^{+} (cyan, actin) DCs migrating in a collagen matrix labeled with AF-594 (red). White square shows the inset used for the close-up in the second part. *Second part:* close-up of the collagen fiber deformation (left) and the actin localization (right).

Supplementary Video 8: Low concentrations of Cdc42 and Rac1 inhibitors induce a slight decrease of cell speed in collagen matrices. Bright field movies of wild-type DCs treated with DMSO (top left), ZCL278 (top right), ML141 (bottom left) or NSC23766 (bottom right) moving in 1.7 mg/mL collagen.

Supplementary Video 9: WASp localization at the central actin pool is lost in *Dock8*$^{-/-}$ DCs. *First part:* TIRF imaging of a WASp-GFP^{+} DC migrating under agarose. The cyan arrow shows the presence of WASp at the periphery, while the red arrow highlights WASp localization in the central actin pool region. *Second part:* TIRF imaging of a *Dock8*$^{-/-}$ WASp-GFP^{+} DC migrating under agarose. The cyan arrow shows the presence of WASp signal at the periphery of the cell.

Supplementary Video 10: DOCK8-GFP accumulates at the constricted site of PDMS constricted channels. Top: *Dock8*$^{-/-}$DCs transfected with a GFP construct (control). While GFP labeling is shown in black, nuclear labeling with Hoechst is presented in blue. Bottom: *Dock8*$^{-/-}$ DCs rescued with DOCK8-GFP (black, actin) and labeled with Hoechst (blue, nucleus). In both cases we observe cells migrating in PDMS channels with a 1.7 μm wide constriction.

Supplementary Video 11: *Dock8*$^{-/-}$ DCs cannot deform the surrounding environment to the same extend as WT *First part: Dock8*$^{-/-}$ LifeAct-eGFP^{+} (black, actin) DC labeled with Hoechst

(blue, nucleus) migrating under agarose with beads labelled with AF-555 (red). *Second part:* Lateral projection of the cell shown before. Scale bar, 2 μm.

Supplementary Video 12: Central actin pool communicates with leading edge actin. *First part:* LifeAct-eGFP^{+} DC migrating in a PDMS pillar maze. Left: time-lapse of a migrating cell; right: retracting lamellipodium (red), central actin pool (light blue) and background (dark blue) regions used for the quantification shown in **Extended Data Fig.4 f.** *Second part:* wild-type (top) and *Dock8*$^{-/-}$ (bottom) LifeAct-eGFP^{+} DCs labeled with Hoechst (blue, nucleus) migrating under stiff agarose. *Third part:* actin-eGFP^{+} DC (top) and resulting segmentation of the actin in protrusion areas (blue), and the central actin pool (red, bottom). *Fourth part:* LifeAct-eGFP^{+} DC (top) and resulting segmentation of the cell body depicted in black, from which we extracted the cell area, and the central actin pool shown in red (bottom).

Supplementary Video 13: DOCK8 differentially affects DC locomotion depending on environmental factors. *First part:* Low magnification (10x) bright field movies of wild-type (left) and *Dock8*$^{-/-}$ (right) migrating in 1.7 mg/mL collagen. *Second part:* High magnification (40x) bright field movies of wild-type (left) and *Dock8*$^{-/-}$ (middle and right) migrating in 1.7 mg/mL collagen. Middle: example of a fragmenting DC. Right: example of a dying DC. *Third part*: wild-type (left) and *Dock8*$^{-/-}$ (middle and right)LifeAct-eGFP^{+} (black, actin) DCs labelled with Hoechst (blue, nucleus) migrating in PDMS pillar mazes. Middle: example of a *Dock8*$^{-/-}$ DC with a single lamellipodium; right: example of a *Dock8*$^{-/-}$ DC forming multiple simultaneous lamellipodia. *Fourth part*: Bright field images of wild-type and *Dock8*$^{-/-}$ DCs labeled with Hoechst (blue, nucleus) migrating in straight PDMS channels.

5 Discussion

5.1 Nucleus-MTOC positioning during migration

In order to fulfill their role in the immune system, dendritic cells (DCs) need to efficiently migrate through a variety of complex 3D environments. To do so, these amoeboid migrating cells rely on their nucleus to probe the surrounding space and find the path of least resistance[102]. Here, we show that, when confronted with more geometrically complex environments, DCs adopt a new locomotory mode and position the MTOC in front of the nucleus, an organelle organization often observed in mesenchymal migrating cells. Despite this organelle re-orientation, no other characteristics typical of mesenchymal migrating cells, like degradation of the surrounding ECM or strong interactions with the substrate, were observed[113].

Indeed, transitions between different migration modes have been reported in the literature. The best studied cases describe transient changes from mesenchymal to amoeboid migration in cancer cells to enhance tissue invasion[105]. Interestingly, this switch is often associated with changes in the environment that surrounds cells. In environments where cells experience physical confinement and reduced adhesion, mesenchymal cells can switch to amoeboid migration, which allows for faster movement without the need for proteolytic degradation of the matrix[114]. This plasticity indicates that rather than using a predefined mode or migration, cells switch modes to adapt to the geometry and characteristics of their surrounding environment. Although molecular mechanisms behind this switch remain unclear, myosin II has been proposed as a key candidate. Complete loss or inhibition of myosin II activity results in impaired nuclear repositioning, suggesting that high myosin contractility supports the nucleus-MTOC switch[115].

5.2 Outward pushing at the cell body and at the periphery

Outward-pushing forces orthogonal to the direction of migration occur at two distinct cellular locations - the cell body, where they are generated by the central actin pool, and the periphery, where they arise from actin foci – both of which influence cell migration.

The formation of the central actin pool is triggered by mechanical confinement of DCs and regulated by the guanine exchange factor (GEF) DOCK8; however, the upstream signal that activates DOCK8 remains unidentified. An interesting candidate is the Hippo kinase MST1, which has been shown to activate DOCK8[116]. In the canonical Hippo pathway, MST1 kinase controls the activity of Yes-associated protein (YAP) and transcriptional co-activator with PDZ-binding motif (TAZ), formally known as YAP/TAZ. MST1 phosphorylation of YAP/TAZ triggers inactivation and cytoplasmic sequestering of this complex, effectively suppressing the expression of genes involved in cell proliferation and survival, thereby regulating organ architecture[117] and preventing uncontrolled cell growth and tumorigenesis[118]. Contrary to what has been established in multicellular organisms, depletion of the YAP/TAZ ortholog in the unicellular organism *Capsaspora owczarzaki* does affect cell proliferation, but instead impacts actin polymerization and cell morphology. This suggests that, from an evolutionary perspective, before multicellularity, the Hippo pathway may have originally regulated cytoskeleton dynamics prior to the emergence of multicellularity[119,120]. It is thus plausible that in single cells, MST1 might have a role in regulating individual cell shape in response to

mechanical confinement. Indeed, depletion of MST1 in T lymphocytes results in their entanglement in collagen gels, as previously observed for DOCK8-deficient DCs[121], raising the possibility that activation of DOCK8 might be one of the non-canonical roles of MST1 activity. Since DOCK8 has been described as a specific regulator of Cdc42 activity[122], its downstream pathway signaling is better understood. Among other effectors, Cdc42 activates WASp, which triggers branched actin polymerization via the Arp2/3 complex[123]. Given that WASp and DOCK8 form a complex via the scaffold protein WIP in T lymphocytes[124], it is plausible that, downstream of DOCK8, WASp may mediate the outward-directed forces exerted by the central actin pool. Indeed, we have observed the presence of WASp at the central actin pool; however, WASp depletion only resulted in a partial loss of the central actin pool, suggesting that Cdc42 activation by DOCK8 in this region might not only trigger WASp but also other nucleation-promoting factors, such as formins.

At the periphery of the cell, outward-pushing forces are initiated by bar-domain proteins. Bar domain-containing proteins are characterized by a crescent-shaped Bar domain that senses and induces membrane curvature[125]. These proteins can be categorized into two subtypes: F-bar domain proteins, which associate with positive curvature (as observed during endocytosis or phagocytosis); and I-Bar domain proteins, which recognize negative membrane curvature (as in, for example, filopodia formation)[126]. Several of these proteins have been shown to either directly recruit Rho GTPases to specific curvature membrane places, or to interact with GEFs which activate these GTPases[127]. Indeed, we observed that CIP4, an F-Bar domain protein that acts as a scaffold for Cdc42 and N-WASp[128], localizes in places of positive membrane curvature, correlating with the presence of WASp and protrusive actin foci that remodel the ECM. These data suggest that topological changes in the environment can lead to the recruitment of Bar-domain proteins that trigger actin polymerization pathways, making these proteins interesting candidates to further understand Rho GTPase activation during migration in complex 3D environments. Although further investigation is needed to understand how cells adapt to their surroundings, they likely rely on a combination of mechanical cues and membrane curvature sensing to activate signaling pathways that drive actin polymerization at the cell body and the periphery.

Our work indicates that protrusive forces at the cell body and the periphery are regulated by Cdc42 activity. However, as it was previously discussed, the molecular mechanisms governing actin polymerization at these two sites appear to differ, with Cdc42 and WASp being the only shared components. The specific localization of DOCK8 within the cell may help explain these differences. Several GEFs have been described to localize to specific regions of migrating cells, where they can locally activate their effectors. For example, β-Pix (ARHGEF7), an activator of Rac1 and Cdc42, localizes at focal adhesions[129–131] and Tiam 1, a Rac1 GEF, localizes at cell-cell junctions[132] and focal adhesions[131,133]. The DOCK homology region 1 (DHR-1) domain of DOCK8 specifically binds to phosphatidylinositol 4,5-bisphosphate (PIP2)[134]. This phosphoinositide is enriched in the inner leaflet of the plasma membrane, but can also be found in several intracellular compartments like the Golgi apparatus, endosomes, and lysosomes[135]. In fact, DOCK8 has been shown to accumulate at the surface of lysosomes, where it regulates actin polymerization[136], suggesting that DOCK8 biased localization to organelle endomembranes, possibly mediated by PIP2, can trigger Cdc42 activation and actin polymerization upon confinement. Why is the localization of DOCK8 specific to organelle endomembranes when PIP2 is fairly abundant throughout the whole plasma membrane, or why is it only activated through confinement, is not well understood. One possibility is that DOCK8 requires other scaffold proteins or interacting partners to facilitate its functions.

Similarly to what has been described in yeast, where binding of the scaffold protein Bem1 to Cdc24 enhances its GEF activity[137], or in mammalian cells, where formation of a complex between p21-activated kinases (PAKs) and the GEF β-Pix enhances localized Rac1 activation, DOCK8 might require an interacting partner that directs its localization and activity.
Although DOCK8 specifically locates at the cell center, WASp, which closely associates with the actin cortex[138], is present at both the center and the periphery of the cell. The central actin pool at the cell body and the WASp-mediated actin foci at the periphery are structurally distinct. While the central pool consists of a dense accumulation of highly dynamic actin filaments, the peripheral foci appear as small, discrete patches. Raising the hypothesis that, at the lamellipodium, where the cell is particularly thin, Arp2/3 mediated actin polymerization driven by Cdc42-WASp activation is sufficient to generate outward pushing forces. In contrast, at the cell body, where the cell is bulkier, WASp-mediated actin polymerization near the plasma membrane likely requires additional support. This support could be provided by organelles, such as lysosomes, where the presence of DOCK8 triggers Cdc42 activation and promotes actin polymerization.

5.3 Why to push outwards?

Formation of a central actin pool might be particularly important for DCs. Since these cells neither tightly adhere and pull, nor degrade their surroundings[93,139], they rely on both the actin foci at the lamellipodium and the central actin pool at the center of the cell to generate space and allow passage of the cell body. However, being able to push outwards can have other advantages besides facilitating migration by rearrangement of the ECM.
Confinement of immature DCs and T lymphocytes induces Arp2/3 dependent actin polymerization around the nucleus[121,140,141]. Additionally, in T lymphocytes, the absence of this pool of actin leads to increased nuclear damage[121], raising the possibility that actin polymerization can be a mechanism for nuclear protection. In contrast to the perinuclear localization observed in immature DCs and T lymphocytes, the central actin pool in mature DCs localizes with other organelles, like the lysosomes or the Golgi apparatus. Actin accumulation around intracellular vesicles has a key role in their intracellular traffic and morphology maintenance[142,143] and, in DCs, it protects lysosomes, preventing leakage of accumulated ingested self-dsDNA, avoiding triggering auto-immune responses[144]. These data suggest that, besides protecting the nucleus, actin polymerization could also preserve the integrity of other organelles.
In addition, we identified the central actin pool as an actin-capacitor in migrating DCs. We observed that changes in actin amounts at the central pool are negatively correlated with changes in the cell periphery, suggesting a tight regulation between different pools of F-actin. How different actin pools communicate is better understood in yeast, where F-actin comes either in the form of patches or cables. In yeast, reduction of one structure is balanced by an increase of the other, conserving the overall levels of F-actin[145]. A similar process has been proposed in animal cells. Here, manipulation of Arp2/3 complex-dependent and -independent actin assembly pathways also resulted in the maintenance of the total level of F-actin[146]. While these observations suggest that F-actin structures may influence and regulate one another, an alternative explanation is that they are indirectly balanced by competition for a shared pool of free G-actin[147]. However, the molecular mechanisms or the upstream signals that rule and coordinate this balance remain unclear.

References

1. Buchmann, K. Evolution of Innate Immunity: Clues from Invertebrates via Fish to Mammals. *Front. Immunol.* **5**, 459 (2014).
2. Riera Romo, M., Pérez-Martínez, D. & Castillo Ferrer, C. Innate immunity in vertebrates: an overview. *Immunology* **148**, 125–139 (2016).
3. Jr, C. A. J. *et al. Immunobiology*. (Garland Science, 2001).
4. Takeuchi, O. & Akira, S. Pattern recognition receptors and inflammation. *Cell* **140**, 805–820 (2010).
5. Lam, N., Lee, Y. & Farber, D. L. A guide to adaptive immune memory. *Nat. Rev. Immunol.* **24**, 810–829 (2024).
6. Sichien, D., Lambrecht, B. N., Guilliams, M. & Scott, C. L. Development of conventional dendritic cells: from common bone marrow progenitors to multiple subsets in peripheral tissues. *Mucosal Immunol.* **10**, 831–844 (2017).
7. Savina, A. & Amigorena, S. Phagocytosis and antigen presentation in dendritic cells. *Immunol. Rev.* **219**, 143–156 (2007).
8. Liu, Z. & Roche, P. A. Macropinocytosis in phagocytes: regulation of MHC class-II-restricted antigen presentation in dendritic cells. *Front. Physiol.* **6**, (2015).
9. Liu, J., Zhang, X., Cheng, Y. & Cao, X. Dendritic cell migration in inflammation and immunity. *Cell. Mol. Immunol.* **18**, 2461–2471 (2021).
10. Chudnovskiy, A., Pasqual, G. & Victora, G. D. Studying interactions between Dendritic Cells and T cells in vivo. *Curr. Opin. Immunol.* **58**, 24–30 (2019).
11. Tai, Y., Wang, Q., Korner, H., Zhang, L. & Wei, W. Molecular Mechanisms of T Cells Activation by Dendritic Cells in Autoimmune Diseases. *Front. Pharmacol.* **9**, 642 (2018).
12. Kjøller, L. & Hall, A. Signaling to Rho GTPases. *Exp. Cell Res.* **253**, 166–179 (1999).
13. Sah, V. P., Seasholtz, T. M., Sagi, S. A. & Brown, J. H. The role of Rho in G protein-coupled receptor signal transduction. *Annu. Rev. Pharmacol. Toxicol.* **40**, 459–489 (2000).
14. Erlandson, S. C., McMahon, C. & Kruse, A. C. Structural Basis for G Protein-Coupled Receptor Signaling. *Annu. Rev. Biophys.* **47**, 1–18 (2018).
15. Kankanamge, D., Tennakoon, M., Karunarathne, A. & Gautam, N. G protein gamma subunit, a hidden master regulator of GPCR signaling. *J. Biol. Chem.* **298**, 102618 (2022).
16. Brock, C. *et al.* Roles of G beta gamma in membrane recruitment and activation of p110 gamma/p101 phosphoinositide 3-kinase gamma. *J. Cell Biol.* **160**, 89–99 (2003).
17. Chen, C.-L. *et al.* Molecular basis for Gβγ-mediated activation of phosphoinositide 3-kinase γ. *Nat. Struct. Mol. Biol.* **31**, 1198–1207 (2024).
18. Lämmermann, T. & Kastenmüller, W. Concepts of GPCR-controlled navigation in the immune system. *Immunol. Rev.* **289**, 205–231 (2019).
19. Mosaddeghzadeh, N. & Ahmadian, M. R. The RHO Family GTPases: Mechanisms of Regulation and Signaling. *Cells* **10**, 1831 (2021).
20. Schmidt, A. & Hall, A. Guanine nucleotide exchange factors for Rho GTPases: turning on the switch. *Genes Dev.* **16**, 1587–1609 (2002).
21. Vetter, I. R. & Wittinghofer, A. The Guanine Nucleotide-Binding Switch in Three Dimensions. *Science* **294**, 1299–1304 (2001).
22. Rossman, K. L., Der, C. J. & Sondek, J. GEF means go: turning on RHO GTPases with guanine nucleotide-exchange factors. *Nat. Rev. Mol. Cell Biol.* **6**, 167–180 (2005).
23. Bernards, A. GAPs galore! A survey of putative Ras superfamily GTPase activating proteins in man and Drosophila. *Biochim. Biophys. Acta* **1603**, 47–82 (2003).

24. Iden, S. & Collard, J. G. Crosstalk between small GTPases and polarity proteins in cell polarization. *Nat. Rev. Mol. Cell Biol.* **9**, 846–859 (2008).
25. Lawson, C. D. & Ridley, A. J. Rho GTPase signaling complexes in cell migration and invasion. *J. Cell Biol.* **217**, 447–457 (2018).
26. Baumeister, M. A., Rossman, K. L., Sondek, J. & Lemmon, M. A. The Dbs PH domain contributes independently to membrane targeting and regulation of guanine nucleotide-exchange activity. *Biochem. J.* **400**, 563–572 (2006).
27. Laurin, M. & Côté, J.-F. Insights into the biological functions of Dock family guanine nucleotide exchange factors. *Genes Dev.* **28**, 533–547 (2014).
28. Côté, J.-F. & Vuori, K. Identification of an evolutionarily conserved superfamily of DOCK180-related proteins with guanine nucleotide exchange activity. *J. Cell Sci.* **115**, 4901–4913 (2002).
29. Côté, J.-F. & Vuori, K. In vitro guanine nucleotide exchange activity of DHR-2/DOCKER/CZH2 domains. *Methods Enzymol.* **406**, 41–57 (2006).
30. Eberth, A. *et al.* Monitoring the real-time kinetics of the hydrolysis reaction of guanine nucleotide-binding proteins. *Biol. Chem.* **386**, 1105–1114 (2005).
31. Nancy J. Fidyk & Richard A. Cerione. Understanding the Catalytic Mechanism of GTPase-Activating Proteins: Demonstration of the Importance of Switch Domain Stabilization in the Stimulation of GTP Hydrolysis | Biochemistry. https://pubs.acs.org/doi/10.1021/bi026413p.
32. Li, R., Zhang, B. & Zheng, Y. Structural determinants required for the interaction between Rho GTPase and the GTPase-activating domain of p190. *J. Biol. Chem.* **272**, 32830–32835 (1997).
33. Sermon, B. A., Lowe, P. N., Strom, M. & Eccleston, J. F. The importance of two conserved arginine residues for catalysis by the ras GTPase-activating protein, neurofibromin. *J. Biol. Chem.* **273**, 9480–9485 (1998).
34. Müller, R. T., Honnert, U., Reinhard, J. & Bähler, M. The rat myosin myr 5 is a GTPase-activating protein for Rho in vivo: essential role of arginine 1695. *Mol. Biol. Cell* **8**, 2039–2053 (1997).
35. Cherfils, J. & Zeghouf, M. Regulation of Small GTPases by GEFs, GAPs, and GDIs. *Physiol. Rev.* **93**, 269–309 (2013).
36. Forget, M.-A., Desrosiers, R. R., Gingras, D. & Béliveau, R. Phosphorylation states of Cdc42 and RhoA regulate their interactions with Rho GDP dissociation inhibitor and their extraction from biological membranes. *Biochem. J.* **361**, 243–254 (2002).
37. Hancock, J. F. & Hall, A. A novel role for RhoGDI as an inhibitor of GAP proteins. *EMBO J.* **12**, 1915–1921 (1993).
38. Jaiswal, M., Dvorsky, R. & Ahmadian, M. R. Deciphering the molecular and functional basis of Dbl family proteins: a novel systematic approach toward classification of selective activation of the Rho family proteins. *J. Biol. Chem.* **288**, 4486–4500 (2013).
39. Iden, S. & Collard, J. G. Crosstalk between small GTPases and polarity proteins in cell polarization. *Nat. Rev. Mol. Cell Biol.* **9**, 846–859 (2008).
40. Riento, K. & Ridley, A. J. ROCKs: multifunctional kinases in cell behaviour. *Nat. Rev. Mol. Cell Biol.* **4**, 446–456 (2003).
41. Ohashi, K. *et al.* Rho-associated kinase ROCK activates LIM-kinase 1 by phosphorylation at threonine 508 within the activation loop. *J. Biol. Chem.* **275**, 3577–3582 (2000).

42. Amano, M. *et al.* Phosphorylation and activation of myosin by Rho-associated kinase (Rho-kinase). *J. Biol. Chem.* **271**, 20246–20249 (1996).
43. Uehata, M. *et al.* Calcium sensitization of smooth muscle mediated by a Rho-associated protein kinase in hypertension. *Nature* **389**, 990–994 (1997).
44. Kimura, K. *et al.* Regulation of myosin phosphatase by Rho and Rho-associated kinase (Rho-kinase). *Science* **273**, 245–248 (1996).
45. Narumiya, S., Tanji, M. & Ishizaki, T. Rho signaling, ROCK and mDia1, in transformation, metastasis and invasion. *Cancer Metastasis Rev.* **28**, 65–76 (2009).
46. Wettschureck, N. & Offermanns, S. Mammalian G proteins and their cell type specific functions. *Physiol. Rev.* **85**, 1159–1204 (2005).
47. O'Connor, K. L. & Mercurio, A. M. Protein kinase A regulates Rac and is required for the growth factor-stimulated migration of carcinoma cells. *J. Biol. Chem.* **276**, 47895–47900 (2001).
48. Feoktistov, I., Goldstein, A. E. & Biaggioni, I. Cyclic AMP and protein kinase A stimulate Cdc42: role of A(2) adenosine receptors in human mast cells. *Mol. Pharmacol.* **58**, 903–910 (2000).
49. Howe, A. K. Regulation of actin-based cell migration by cAMP/PKA. *Biochim. Biophys. Acta* **1692**, 159–174 (2004).
50. Ridley, A. J. Rho GTPases and cell migration. *J. Cell Sci.* **114**, 2713–2722 (2001).
51. Etienne-Manneville, S. & Hall, A. Rho GTPases in cell biology. *Nature* **420**, 629–635 (2002).
52. Rameh, L. E. *et al.* A Comparative Analysis of the Phosphoinositide Binding Specificity of Pleckstrin Homology Domains*. *J. Biol. Chem.* **272**, 22059–22066 (1997).
53. Han, J. *et al.* Role of substrates and products of PI 3-kinase in regulating activation of Rac-related guanosine triphosphatases by Vav. *Science* **279**, 558–560 (1998).
54. Welch, H. C. E. *et al.* P-Rex1, a PtdIns(3,4,5)P3- and Gbetagamma-regulated guanine-nucleotide exchange factor for Rac. *Cell* **108**, 809–821 (2002).
55. Xu, J. *et al.* Divergent signals and cytoskeletal assemblies regulate self-organizing polarity in neutrophils. *Cell* **114**, 201–214 (2003).
56. Spiering, D. & Hodgson, L. Dynamics of the Rho-family small GTPases in actin regulation and motility. *Cell Adhes. Migr.* **5**, 170–180 (2011).
57. El-Sibai, M. *et al.* RhoA/ROCK-mediated switching between Cdc42- and Rac1-dependent protrusion in MTLn3 carcinoma cells. *Exp. Cell Res.* **314**, 1540–1552 (2008).
58. Machacek, M. *et al.* Coordination of Rho GTPase activities during cell protrusion. *Nature* **461**, 99–103 (2009).
59. Welch, M. D. & Mullins, R. D. Cellular Control of Actin Nucleation. *Annu. Rev. Cell Dev. Biol.* **18**, 247–288 (2002).
60. Rosenbloom, A. D., Kovar, E. W., Kovar, D. R., Loew, L. M. & Pollard, T. D. Mechanism of actin filament nucleation. *Biophys. J.* **120**, 4399–4417 (2021).
61. Fujiwara, I., Vavylonis, D. & Pollard, T. D. Polymerization kinetics of ADP- and ADP-Pi-actin determined by fluorescence microscopy. *Proc. Natl. Acad. Sci.* **104**, 8827–8832 (2007).
62. Zebda, N. *et al.* Phosphorylation of ADF/cofilin abolishes EGF-induced actin nucleation at the leading edge and subsequent lamellipod extension. *J. Cell Biol.* **151**, 1119–1128 (2000).
63. Pollard, T. D. & Borisy, G. G. Cellular motility driven by assembly and disassembly of actin filaments. *Cell* **112**, 453–465 (2003).
64. Isenberg, G., Aebi, U. & Pollard, T. D. An actin-binding protein from Acanthamoeba regulates actin filament polymerization and interactions. *Nature* **288**, 455–459 (1980).

65. Cooper, J. A. Actin dynamics: tropomyosin provides stability. *Curr. Biol. CB* **12**, R523-525 (2002).
66. Peskin, C. S., Odell, G. M. & Oster, G. F. Cellular motions and thermal fluctuations: the Brownian ratchet. *Biophys. J.* **65**, 316–324 (1993).
67. Mogilner, A. & Oster, G. Cell motility driven by actin polymerization. *Biophys. J.* **71**, 3030–3045 (1996).
68. Svitkina, T. M., Verkhovsky, A. B., McQuade, K. M. & Borisy, G. G. Analysis of the Actin–Myosin II System in Fish Epidermal Keratocytes: Mechanism of Cell Body Translocation. *J. Cell Biol.* **139**, 397–415 (1997).
69. Svitkina, T. M. & Borisy, G. G. Arp2/3 complex and actin depolymerizing factor/cofilin in dendritic organization and treadmilling of actin filament array in lamellipodia. *J. Cell Biol.* **145**, 1009–1026 (1999).
70. Glacy, S. D. Subcellular distribution of rhodamine-actin microinjected into living fibroblastic cells. *J. Cell Biol.* **97**, 1207–1213 (1983).
71. Snapper, S. B. *et al.* N-WASP deficiency reveals distinct pathways for cell surface projections and microbial actin-based motility. *Nat. Cell Biol.* **3**, 897–904 (2001).
72. Goode, B. L. & Eck, M. J. Mechanism and function of formins in the control of actin assembly. *Annu. Rev. Biochem.* **76**, 593–627 (2007).
73. Bear, J. E. *et al.* Antagonism between Ena/VASP proteins and actin filament capping regulates fibroblast motility. *Cell* **109**, 509–521 (2002).
74. Mattila, P. K. & Lappalainen, P. Filopodia: molecular architecture and cellular functions. *Nat. Rev. Mol. Cell Biol.* **9**, 446–454 (2008).
75. Charras, G. & Paluch, E. Blebs lead the way: how to migrate without lamellipodia. *Nat. Rev. Mol. Cell Biol.* **9**, 730–736 (2008).
76. Paluch, E. K. & Raz, E. The role and regulation of blebs in cell migration. *Curr. Opin. Cell Biol.* **25**, 582–590 (2013).
77. Abercrombie, M., Heaysman, J. E. & Pegrum, S. M. The locomotion of fibroblasts in culture. 3. Movements of particles on the dorsal surface of the leading lamella. *Exp. Cell Res.* **62**, 389–398 (1970).
78. Lauffenburger, D. A. & Horwitz, A. F. Cell Migration: A Physically Integrated Molecular Process. *Cell* **84**, 359–369 (1996).
79. Hsu, J. C. *et al.* Region-specific Epithelial Cell Dynamics During Branching Morphogenesis. *Dev. Dyn. Off. Publ. Am. Assoc. Anat.* **242**, 1066–1077 (2013).
80. Auffray, C. *et al.* Monitoring of blood vessels and tissues by a population of monocytes with patrolling behavior. *Science* **317**, 666–670 (2007).
81. Fisher, G. & Rittié, L. Restoration of the basement membrane after wounding: a hallmark of young human skin altered with aging. *J. Cell Commun. Signal.* **12**, 401–411 (2018).
82. Varki, A. *et al.* Proteoglycans and Glycosaminoglycans. *Essentials of Glycobiology* (Cold Spring Harbor Laboratory Press, 1999).
83. Sutherland, T. E., Dyer, D. P. & Allen, J. E. The extracellular matrix and the immune system: A mutually dependent relationship. *Science* **379**, eabp8964 (2023).
84. Wolf, K. & Friedl, P. Extracellular matrix determinants of proteolytic and non-proteolytic cell migration. *Trends Cell Biol.* **21**, 736–744 (2011).
85. Ballestrem, C., Hinz, B., Imhof, B. A. & Wehrle-Haller, B. Marching at the front and dragging behind. *J. Cell Biol.* **155**, 1319–1332 (2001).
86. Huttenlocher, A. & Horwitz, A. R. Integrins in Cell Migration. *Cold Spring Harb. Perspect. Biol.* **3**, a005074 (2011).

87. Tamariz, E. & Grinnell, F. Modulation of fibroblast morphology and adhesion during collagen matrix remodeling. *Mol. Biol. Cell* **13**, 3915–3929 (2002).
88. Wyckoff, J. B., Pinner, S. E., Gschmeissner, S., Condeelis, J. S. & Sahai, E. ROCK- and myosin-dependent matrix deformation enables protease-independent tumor-cell invasion in vivo. *Curr. Biol. CB* **16**, 1515–1523 (2006).
89. Doyle, A. D., Sykora, D. J., Pacheco, G. G., Kutys, M. L. & Yamada, K. M. 3D mesenchymal cell migration is driven by anterior cellular contraction that generates an extracellular matrix prestrain. *Dev. Cell* **56**, 826-841.e4 (2021).
90. Wang, W. Y., Davidson, C. D., Lin, D. & Baker, B. M. Actomyosin contractility-dependent matrix stretch and recoil induces rapid cell migration. *Nat. Commun.* **10**, 1186 (2019).
91. Wolf, K. *et al.* Compensation mechanism in tumor cell migration. *J. Cell Biol.* **160**, 267–277 (2003).
92. Wolf, K. *et al.* Multi-step pericellular proteolysis controls the transition from individual to collective cancer cell invasion. *Nat. Cell Biol.* **9**, 893–904 (2007).
93. Wolf, K. & Friedl, P. Extracellular matrix determinants of proteolytic and non-proteolytic cell migration. *Trends Cell Biol.* **21**, 736–744 (2011).
94. Infante, E. *et al.* LINC complex-Lis1 interplay controls MT1-MMP matrix digest-on-demand response for confined tumor cell migration. *Nat. Commun.* **9**, 2443 (2018).
95. Yamada, K. M. & Sixt, M. Mechanisms of 3D cell migration. *Nat. Rev. Mol. Cell Biol.* **20**, 738–752 (2019).
96. Friedl, P., Borgmann, S. & Bröcker, E. B. Amoeboid leukocyte crawling through extracellular matrix: lessons from the Dictyostelium paradigm of cell movement. *J. Leukoc. Biol.* **70**, 491–509 (2001).
97. Francis, K., Palsson, B., Donahue, J., Fong, S. & Carrier, E. Murine Sca-1(+)/Lin(-) cells and human KG1a cells exhibit multiple pseudopod morphologies during migration. *Exp. Hematol.* **30**, 460–463 (2002).
98. Wang, W. *et al.* Single cell behavior in metastatic primary mammary tumors correlated with gene expression patterns revealed by molecular profiling. *Cancer Res.* **62**, 6278–6288 (2002).
99. Lämmermann, T. & Sixt, M. Mechanical modes of 'amoeboid' cell migration. *Curr. Opin. Cell Biol.* **21**, 636–644 (2009).
100. Hons, M. *et al.* Chemokines and integrins independently tune actin flow and substrate friction during intranodal migration of T cells. *Nat. Immunol.* **19**, 606–616 (2018).
101. Reversat, A. *et al.* Cellular locomotion using environmental topography. *Nature* **582**, 582–585 (2020).
102. Renkawitz, J. *et al.* Nuclear positioning facilitates amoeboid migration along the path of least resistance. *Nature* **568**, 546–550 (2019).
103. Petrie, R. J., Koo, H. & Yamada, K. M. Generation of compartmentalized pressure by a nuclear piston governs cell motility in a 3D matrix. *Science* **345**, 1062–1065 (2014).
104. Petrie, R. J. & Yamada, K. M. At the leading edge of three-dimensional cell migration. *J. Cell Sci.* **125**, 5917–5926 (2012).
105. Panková, K., Rösel, D., Novotný, M. & Brábek, J. The molecular mechanisms of transition between mesenchymal and amoeboid invasiveness in tumor cells. *Cell. Mol. Life Sci. CMLS* **67**, 63–71 (2010).
106. Alexandrova, A. Y., Chikina, A. S. & Svitkina, T. M. Actin cytoskeleton in mesenchymal-to-amoeboid transition of cancer cells. *Int. Rev. Cell Mol. Biol.* **356**, 197–256 (2020).

107. Rösel, D. *et al.* Up-regulation of Rho/ROCK signaling in sarcoma cells drives invasion and increased generation of protrusive forces. *Mol. Cancer Res. MCR* **6**, 1410–1420 (2008).
108. Kurz, A. R. M. *et al.* MST1-dependent vesicle trafficking regulates neutrophil transmigration through the vascular basement membrane. https://www.jci.org/articles/view/87043/pdf (2016) doi:10.1172/JCI87043.
109. Parri, M., Taddei, M. L., Bianchini, F., Calorini, L. & Chiarugi, P. EphA2 reexpression prompts invasion of melanoma cells shifting from mesenchymal to amoeboid-like motility style. *Cancer Res.* **69**, 2072–2081 (2009).
110. Bergert, M., Chandradoss, S. D., Desai, R. A. & Paluch, E. Cell mechanics control rapid transitions between blebs and lamellipodia during migration. *Proc. Natl. Acad. Sci. U. S. A.* **109**, 14434–14439 (2012).
111. Petrie, R. J. & Yamada, K. M. Fibroblasts Lead the Way: A Unified View of 3D Cell Motility. *Trends Cell Biol.* **25**, 666–674 (2015).
112. Yamada, K. M. *et al.* Extracellular matrix dynamics in cell migration, invasion and tissue morphogenesis. *Int. J. Exp. Pathol.* **100**, 144–152 (2019).
113. Canigova, N. Adaptive strategies of dendritic cell migration in response to environmental cues. (2025).
114. Liu, Y.-J. *et al.* Confinement and Low Adhesion Induce Fast Amoeboid Migration of Slow Mesenchymal Cells. *Cell* **160**, 659–672 (2015).
115. Kroll, J., Hauschild, R. & Kuznetcov, A. Adaptive pathfinding by nucleokinesis during amoeboid migration. doi:10.15252/embj.2023114557.
116. Mou, F. *et al.* The Mst1 and Mst2 kinases control activation of rho family GTPases and thymic egress of mature thymocytes. *J. Exp. Med.* **209**, 741–759 (2012).
117. Zhou, D. *et al.* Mst1 and Mst2 maintain hepatocyte quiescence and suppress hepatocellular carcinoma development through inactivation of the Yap1 oncogene. *Cancer Cell* **16**, 425–438 (2009).
118. The Hippo signalling pathway and its implications in human health and diseases | Signal Transduction and Targeted Therapy. https://www.nature.com/articles/s41392-022-01191-9.
119. Phillips, J. E., Santos, M., Konchwala, M., Xing, C. & Pan, D. Genome editing in the unicellular holozoan Capsaspora owczarzaki suggests a premetazoan role for the Hippo pathway in multicellular morphogenesis. *eLife* **11**, e77598 (2022).
120. Phillips, J. E., Zheng, Y. & Pan, D. Assembling a Hippo: the evolutionary emergence of an animal developmental signaling pathway. *Trends Biochem. Sci.* **49**, 681–692 (2024).
121. Shen, C. *et al.* DOCK8 regulates a mechanosensitive actin redistribution that maintains immune cell cohesion and protects the nucleus during migration. 2024.07.26.605273 Preprint at https://doi.org/10.1101/2024.07.26.605273 (2024).
122. Harada, Y. *et al.* DOCK8 is a Cdc42 activator critical for interstitial dendritic cell migration during immune responses. *Blood* **119**, 4451–4461 (2012).
123. Rotty, J. D., Wu, C. & Bear, J. E. New insights into the regulation and cellular functions of the ARP2/3 complex. *Nat. Rev. Mol. Cell Biol.* **14**, 7–12 (2013).
124. Janssen, E. *et al.* A DOCK8-WIP-WASp complex links T cell receptors to the actin cytoskeleton. https://www.jci.org/articles/view/85774/pdf (2016) doi:10.1172/JCI85774.
125. Peter, B. J. *et al.* BAR domains as sensors of membrane curvature: the amphiphysin BAR structure. *Science* **303**, 495–499 (2004).

126. Simunovic, M., Evergren, E., Callan-Jones, A. & Bassereau, P. Curving Cells Inside and Out: Roles of BAR Domain Proteins in Membrane Shaping and Its Cellular Implications. *Annu. Rev. Cell Dev. Biol.* **35**, 111–129 (2019).
127. de Kreuk, B.-J. & Hordijk, P. L. Control of Rho GTPase function by BAR-domains. *Small GTPases* **3**, 45–52 (2012).
128. Pichot, C. S. *et al.* Cdc42-interacting protein 4 promotes breast cancer cell invasion and formation of invadopodia through activation of N-WASp. *Cancer Res.* **70**, 8347–8356 (2010).
129. Hoefen, R. J. & Berk, B. C. The multifunctional GIT family of proteins. *J. Cell Sci.* **119**, 1469–1475 (2006).
130. Turner, C. E. *et al.* Paxillin LD4 motif binds PAK and PIX through a novel 95-kD ankyrin repeat, ARF-GAP protein: A role in cytoskeletal remodeling. *J. Cell Biol.* **145**, 851–863 (1999).
131. Goicoechea, S. M., Awadia, S. & Garcia-Mata, R. I'm coming to GEF you: Regulation of RhoGEFs during cell migration. *Cell Adhes. Migr.* **8**, 535–549 (2014).
132. Mertens, A. E. E., Pegtel, D. M. & Collard, J. G. Tiam1 takes PARt in cell polarity. *Trends Cell Biol.* **16**, 308–316 (2006).
133. Wang, S. *et al.* Tiam1 interaction with the PAR complex promotes talin-mediated Rac1 activation during polarized cell migration. *J. Cell Biol.* **199**, 331–345 (2012).
134. Sakurai, T. *et al.* A conserved PI(4,5)P2–binding domain is critical for immune regulatory function of DOCK8. *Life Sci. Alliance* **4**, e202000873 (2021).
135. Ravi, A., Palamiuc, L. & Emerling, B. M. Crucial Players for Inter-Organelle Communication: PI5P4Ks and Their Lipid Product PI-4,5-P2 Come to the Surface. *Front. Cell Dev. Biol.* **9**, 791758 (2021).
136. Gutierrez-Ruiz, O. L. *et al.* Ectopic expression of DOCK8 regulates lysosome-mediated pancreatic tumor cell invasion. *Cell Rep.* **42**, 113042 (2023).
137. Rapali, P. *et al.* Scaffold-mediated gating of Cdc42 signalling flux. *eLife* **6**, e25257 (2017).
138. Takenawa, T. & Miki, H. WASP and WAVE family proteins: key molecules for rapid rearrangement of cortical actin filaments and cell movement. *J. Cell Sci.* **114**, 1801–1809 (2001).
139. Wolf, K. *et al.* Multi-step pericellular proteolysis controls the transition from individual to collective cancer cell invasion. *Nat. Cell Biol.* **9**, 893–904 (2007).
140. Alraies, Z. *et al.* Cell shape sensing licenses dendritic cells for homeostatic migration to lymph nodes. *Nat. Immunol.* **25**, 1193–1206 (2024).
141. Thiam, H.-R. *et al.* Perinuclear Arp2/3-driven actin polymerization enables nuclear deformation to facilitate cell migration through complex environments. *Nat. Commun.* **7**, (2016).
142. Taunton, J. *et al.* Actin-Dependent Propulsion of Endosomes and Lysosomes by Recruitment of N-Wasp✪. *J. Cell Biol.* **148**, 519–530 (2000).
143. Duleh, S. N. & Welch, M. D. WASH and the Arp2/3 complex regulate endosome shape and trafficking. *Cytoskelet. Hoboken NJ* **67**, 193–206 (2010).
144. Piperno, G. M. *et al.* Wiskott-Aldrich syndrome protein restricts cGAS/STING activation by dsDNA immune complexes. *JCI Insight* **5**, e132857, 132857 (2020).
145. Suarez, C. *et al.* Profilin Regulates F-Actin Network Homeostasis by Favoring Formin over Arp2/3 Complex. *Dev. Cell* **32**, 43–53 (2015).
146. Rotty, J. D. *et al.* Profilin-1 Serves as a Gatekeeper for Actin Assembly by Arp2/3-Dependent and -Independent Pathways. *Dev. Cell* **32**, 54–67 (2015).

147. Kiuchi, T., Nagai, T., Ohashi, K. & Mizuno, K. Measurements of spatiotemporal changes in G-actin concentration reveal its effect on stimulus-induced actin assembly and lamellipodium extension. *J. Cell Biol.* **193**, 365–380 (2011).